学 位 論 文

X-ray Study of Rapid Variability in TeV Blazars and the Implications on Particle Acceleration in Jets

[X線を用いたTeVガンマ線放射ブレーザーの速い時間変動の研究およびジェット内部での粒子加速への示唆]

平成11年12月博士（理学）申請

東京大学大学院理学系研究科
物理学専攻

片 岡 淳

X-ray Study of Rapid Variability in TeV Blazars and the Implications on Particle Acceleration in Jets

Jun KATAOKA

Doctoral Thesis

Department of Physics
Faculty of Science
University of Tokyo

December 1999

Abstract

Four TeV blazars, Mrk 421, Mrk 501, PKS 2155−304, and 1ES 2344+514, have been studied with the X–ray satellites *ASCA* and *RXTE*. Because spectral energy distributions of TeV blazars cover all observable bands, and their fluxes vary rapidly, we conducted a number of multi-frequency campaigns. In particular, our observations of Mrk 421 and Mrk 501 in both X-ray and TeV γ-ray bands provide the first truly simultaneous data sets in various phases of source activity. The overall νL_ν spectra of TeV blazars show two broad pronounced peaks in the spectral energy distribution: one is located between the radio and X-ray bands, and another in the γ-ray regime. We found that variability in the X-ray and TeV bands is well correlated on time scale of a day to years. The amplitude of flux variation was comparable in both energy bands for Mrk 421 ([X-ray flux] $\propto$ [TeV flux]), while quadratic for Mrk 501 ([X-ray flux]^2 $\propto$ [TeV flux]). The data considered here support the currently popular models where the low energy peak is produced via the synchrotron process, and the high energy peak is produced by Comptonization of the synchrotron photons by the *same* electrons that produced the synchrotron photons (the SSC model). The physical parameters relevant for the emission were successfully constrained from the observational properties of each TeV blazar.

Analysis of the X-ray data indicated five principal results. First, we detected the peak of the synchrotron component for all TeV blazars. We found that the position of the synchrotron peak shifted from lower to higher energy when the source became brighter. This correlation is best studied for Mrk 421 and Mrk 501. The relationship between the peak energy and luminosity showed quite different behavior in the two sources. Data for Mrk 421 indicated very little change in the peak position (0.5−2 keV), while Mrk 501 revealed the lagest shift ever observed in blazars (1−100 keV). Second, seven day uninterrupted observation of Mrk 421 revealed day-by-day flares, which were strongly correlated from the UV to the hard X-ray bands. We found that the characteristic time scales of individual flare events are similar for all TeV blazars ($\sim$ 1 day), but are slightly different in each object. Below this time scale, rapid variability appears strongly suppressed, indicating 'strong red-noise' type behavior ($\propto f^{-2} \sim f^{-3}$ in the Power Spectrum Density). Third, from the analysis of light curves of the blazar Mrk 421, we found the presence of 'hard-lag' flares, where soft X-ray variations *precede* those in the hard X-rays. More remarkably, time-lags in various X-ray energy bands changed flare by flare, and hence the *paradigm* of 'soft-lag' does not always apply. Fourth, we detected the general trend that the amplitude of variation becomes larger at increasing photon energy. A few exceptions were found in which variation in the lower energy X-ray band is larger or comparable to that in the higher energy band. Fifth, time profiles of each flare event were almost *symmetric*,

meaning that they are characterized by nearly equal rise-time and decay-time. From the detailed temporal analysis, we discovered that the symmetry of the time profiles tends to break down at lower energies.

Clear correlations of synchrotron peak energy with peak luminosity, found in Mrk 421 and Mrk 501, suggest that flaring behavior is repeatable and reproduced in these objects. However, very different spectral evolution of Mrk 421 and Mrk 501 probably indicates some differences in the electron acceleration mechanism at work during the flares. Our result strongly supports the idea that the variability of TeV blazars is most probably due to the changes in the injected electron number and/or maximum Lorentz factor ($\gamma_{\rm max}$). Data for Mrk 421 indicate that the flux variability is associated with an increase in the number of electrons, while only small changes are implied for $\gamma_{\rm max}$. On the other hand, the flare of Mrk 501 is mostly due to the large changes in $\gamma_{\rm max}$ while keeping the electron number almost conservative. Interestingly, our X-ray data and interpretation suggest that the origin of the flares may be associated with what is expected from the VLBI observations of superluminal motion.

From the X-ray study of TeV blazars, we suggest that at least four dynamical time scales must be taken into account to understand the observed time variabilities. These are (1) electron accerelation time, $t_{\rm acc}$, (2) electron cooling time, $t_{\rm cool}$, (3) source light travel time, $t_{\rm crs}$ and (4) electron injection time, $t_{\rm inj}$. We show that all the variability patterns in blazars are well understood by the balance of those time scales. To confirm our knowledge of spectral evolution and rapid variability in blazars more *quantitatively*, we have developed a new time-dependent SSC code, incorporating the radiative cooling and acceleration process, as well as light travel time effects properly. That is because we deemed the popular SSC model based on *steady state* emission as inadequate for our case, given the detection of the *rapid flux and spectral time variability* in blazars. By using the code developed by us, we simulated various types of flares for TeV blazars. We confirmed that 'soft-lag' will be expected when the acceleration time of electrons is much shorter than cooling time, while 'hard-lag' can be observed when the acceleration time is nearly equal to the cooling time, which is only expected around $\gamma_{\rm max}$.

Contents

1 Introduction **1**

2 Observational Properties of Blazars **5**

2.1 Unifying Active Galactic Nuclei (AGN) 5

2.1.1 Classification of AGN 5

2.1.2 Unified Picture of AGN 6

2.1.3 Blazars – Roles in All AGN Classes 7

2.2 Observations of Blazars 8

2.2.1 Spectral Energy Distribution 8

2.2.2 Time Variability 10

2.2.3 X-ray Spectral Evolution 11

2.2.4 Implications on the Relativistic Beaming 12

2.3 Jet Models for Blazar Emission 13

2.3.1 Leptonic Jet Models 13

2.3.2 Time Dependent SSC Model 15

2.3.3 Comment on the Hadronic Jet Model 17

2.4 TeV Blazars – Clue to the Jet Physics 17

2.4.1 Unifying Blazar Classes 17

2.4.2 Extreme Particle Accelerators – TeV Blazars 19

2.4.3 Individual Target 21

2.5 Effects by the DIRB 25

3 Emission Mechanism of Blazars **27**

3.1 Energy Gain Processes 27

3.1.1 2nd order Fermi Acceleration 27

3.1.2 1st order Fermi Acceleration 28

3.1.3 Acceleration Rate 29

3.1.4 Diffusion Coefficient 30

3.1.5 Energy Spectrum . . . 31
3.2 Energy Loss Processes . . . 32
3.3 Synchrotron Radiation . . . 33
3.3.1 Emission from a Single Electron . . . 33
3.3.2 Emission Coefficient : j_ν . . . 35
3.3.3 Absorption Coefficient : α_ν . . . 36
3.4 Inverse Compton Radiation . . . 36
3.4.1 Scattering From a Single Electron . . . 37
3.4.2 Inverse Compton Spectrum . . . 38
3.5 Particle Escape and Adiabatic Expansion . . . 39
3.6 Electron Kinetic Equation . . . 40
3.7 Relativistic Beaming in Blazar Jets . . . 42
3.7.1 Aberration of Light . . . 42
3.7.2 Time Dilation . . . 42
3.7.3 Blue Shift of Frequencies and the Luminosity Enhancement . . . 43

4 Instruments on-board *ASCA* 45
4.1 *ASCA* Satellite . . . 45
4.2 XRT . . . 46
4.3 SIS . . . 47
4.3.1 System Description . . . 47
4.3.2 On-Board Data Processing . . . 49
4.3.3 Reduction of the SIS data . . . 51
4.4 GIS . . . 52
4.4.1 System Description . . . 52
4.4.2 On-Board Data Processing . . . 54
4.4.3 Reduction of the GIS data . . . 54
4.5 Alignment of the Detectors . . . 55

5 Instruments on-board *RXTE* 57
5.1 *RXTE* Satellite . . . 57
5.2 PCA . . . 58
5.2.1 System Description . . . 58
5.2.2 On-Board Data Processing . . . 60
5.2.3 Reduction of PCA data . . . 60
5.3 HEXTE . . . 62
5.4 ASM . . . 63

5.4.1 System Description . . . 63
5.4.2 Reduction of ASM data . . . 65

6 Observation 67
6.1 X-ray Observations with *ASCA* . . . 67
6.2 X-ray Observations with *RXTE* . . . 69
6.3 Individual Targets . . . 71
6.4 Simultaneous Observations . . . 72
6.4.1 X-ray and GeV γ-ray (EGRET) observations . . . 72
6.4.2 X-ray and TeV γ-ray (*Whipple*) observations . . . 73

7 Analysis and Results of *ASCA* Observations 75
7.1 Analysis . . . 75
7.1.1 Data Reduction . . . 75
7.1.2 Background Subtraction . . . 76
7.1.3 Treatment of the Telemetry Saturation . . . 78
7.2 Results from Temporal Studies . . . 78
7.2.1 Time Variability . . . 78
7.2.2 Energy Dependence of Variability . . . 82
7.2.3 Structure Function . . . 87
7.2.4 Spectral Evolutions . . . 95
7.2.5 Search for Time Lags and Time Leads . . . 96
7.3 Results from Spectral Studies . . . 104
7.3.1 Fit with a Power Law Function plus Absorption . . . 104
7.3.2 Fit with a Cutoff Power Law Function . . . 109
7.3.3 Shift of the Synchrotron Peak . . . 111

8 Analysis and Results of *RXTE* Observations 115
8.1 Analysis . . . 115
8.1.1 Data Reduction . . . 115
8.1.2 Background Subtraction . . . 116
8.2 Results from Temporal Studies . . . 117
8.2.1 Time Variability . . . 117
8.2.2 Energy Dependence of Variability . . . 122
8.2.3 Structure Function . . . 126
8.2.4 Spectral Evolutions . . . 131
8.3 Results from Spectral Studies . . . 133

8.3.1 Fit with a Power Law Function . . . 133
8.3.2 Comparison between *ASCA* and *RXTE* . . . 134
8.3.3 Shift of the Synchrotron Peak . . . 138

9 Multi-wavelength Properties of TeV Blazars **143**
9.1 Mrk 421 . . . 144
9.2 Mrk 501 . . . 148
9.3 PKS 2155−304 . . . 153
9.4 1ES 2344+514 . . . 155

10 Discussion **157**
10.1 Summary of Results . . . 157
10.2 Dynamics of Rapid Variability . . . 160
10.2.1 Synchrotron Cooling . . . 160
10.2.2 Smoothing by Light Travel Time . . . 163
10.2.3 Acceleration of Electrons . . . 165
10.2.4 Application of Acceleration/Cooling Model to Data . . . 167
10.2.5 Comment on Multiple Emission Models . . . 169
10.2.6 Cooling Time vs Escape Time . . . 170
10.3 Properties of Short-Time Variability in Blazars . . . 172
10.4 X-ray Flares and Implications on the Jet Structure . . . 175
10.5 Implications from Inter-band Correlation . . . 179
10.6 Constraints on the Physical Parameters . . . 182
10.6.1 Allowed Parameter Region . . . 182
10.6.2 Individual Target . . . 185
10.7 Motivation to develop a 'NEW' theoretical model . . . 192

11 Time-Dependent SSC Model **195**
11.1 One-zone Homogeneous SSC Model . . . 195
11.2 Application to the Time-Dependent Model . . . 196
11.2.1 Assumptions . . . 196
11.2.2 Connection between Acceleration Region and Emission Region . . . 197
11.2.3 Numerical Approach . . . 198
11.2.4 Light Travel Time Effects . . . 199
11.3 Acceleration of Electrons . . . 200
11.3.1 Electron Injection at γ_0 . . . 200
11.3.2 Evolution of Electron Distribution after Stopping the Injection . . . 201

11.4 Examples [I] – Steady State Emission . . . 202
11.4.1 SSC Spectrum and Higher Order Comptonization . . . 203
11.4.2 Effects of the Changes in Parameters . . . 204
11.5 Examples [II] – Time Evolution . . . 207
11.5.1 Synchrotron Cooling Model . . . 207
11.5.2 Time Evolution of the SSC Spectrum and Light Curves . . . 208
11.6 Comments on the Time-Dependent Model . . . 211
11.6.1 Emission from the Acceleration Region . . . 211
11.6.2 Scope for Improvement . . . 212
11.7 Application to the Observational Data . . . 213
11.7.1 Steady State Emission . . . 213
11.7.2 Modeling PKS 2155−304 Flare in 1994 . . . 216
11.7.3 Modeling Mrk 421 Flare . . . 221
11.7.4 Spectral Evolutions . . . 226
11.7.5 Modeling Mrk 501 Flare . . . 229
11.7.6 Unified Picture of Rapid Variability in TeV Blazars . . . 230

12 Conclusion **235**

A *RXTE* Observation Log of TeV Blazars **239**

B DCF Distributions of Mrk 421 during 1998 Campaign **249**

C Estimation of Errors in the Temporal Analysis **259**
C.1 Errors on Lags Estimated from the Monte Calro Simulations . . . 259
C.2 Analysis of De-Trended Light Curves . . . 260

D *ASCA* Spectra of TeV blazars **263**

E Synchrotron Peak Shifts of TeV blazars **273**

F HEXTE spectra of Mrk 501 in 1998 **277**

G Spectral Fit Results of *RXTE* Observations **279**

H *RXTE* Spectra of TeV Blazars **291**

I Homogeneous SSC model **297**
I.1 Solution for a Spherical Geometry . . . 297
I.2 Correction Factor: $C_{\rm corr}$ . . . 299

J Numerical Approach to the Kinetic Equation 301

Acknowledgment 313

List of Figures

1.1 Multi-frequency spectra of Mrk 421 and PKS 0528+134 2

2.1 A categorization of AGNs 6
2.2 Unified scheme of all types of AGNs 7
2.3 Spectral energy distribution of the TeV blazar Mrk 421 9
2.4 Variation of TeV γ-ray rates of Mrk 501 10
2.5 Light curves obtained from Nov 1997 observation of PKS2155−304 with *BeppoSax* 11
2.6 Hysteresis in the variation of the TeV blazar Mrk 421 12
2.7 Schematic view of leptonic jet models 14
2.8 Time-dependent model for multi-wavelength spectrum and light curves of Mrk 421 16
2.9 Unified picture of SED for all types of blazars 18
2.10 Correlation between $\gamma_{\rm peak}$ and the total energy density 19
2.11 Unified scheme of all types of blazars 20
2.12 Energy density of the DIRB: observation and theoretical prediction 26
2.13 Optical depth for DIRB absorption 26

3.1 Schematic view of 2nd order Fermi Acceleration 28
3.2 Schematic view of 1st order Fermi Acceleration 29
3.3 Energy loss rate $b(\gamma)$ from a single electron 33
3.4 Synchrotron spectrum from a single electron 34
3.5 Synchrotron emission coefficient j_ν 35
3.6 Synchrotron absorption coefficient α_ν 36
3.7 Geometries for inverse Compton scattering 37
3.8 Ratio of synchrotron and inverse Compton cooling 40
3.9 Beaming factor as a function of viewing angle 43

4.1 Schematic drawing of the *ASCA* satellite 45
4.2 Arrangement of instruments on the *ASCA* satellite 46

4.3 Alignment of four CCD chips in SIS . . . 48
4.4 Definitions of grades of events . . . 50
4.5 Structure of GIS . . . 53
4.6 Alignment of the detectors . . . 56

5.1 Schematic drawing of the *RXTE* satellite . . . 58
5.2 Schematic view of PCA counters . . . 59
5.3 The PCA background in Orbit . . . 61
5.4 All-Sky Monitor shadow camera . . . 64

6.1 Observations of four TeV blazars with *ASCA* & *RXTE* . . . 68

7.1 Effects of telemetry saturation for Mrk 421 data . . . 79
7.2 Mrk 421 light curve in 1993–1998 . . . 80
7.3 Mrk 501 light curve in 1996–1998 . . . 81
7.4 PKS 2155–304 light curve in 1993–1996 . . . 82
7.5 1ES 2344+514 light curve in 1997 . . . 83
7.6 Variability amplitude of four TeV blazars (*ASCA*) . . . 84
7.7 Variability amplitude of Mrk 421 in 1998 . . . 85
7.8 Light curves of Mrk 421 in 1998 divided into 10 segments . . . 85
7.9 Variability amplitudes of individual flares of Mrk 421 . . . 86
7.10 Schematic drawing of the Structure Function . . . 88
7.11 Simulated structure function for $P(f) \propto f^{-2.2}$ . . . 89
7.12 Structure functions of TeV blazars (*ASCA*) . . . 92
7.13 Symmetry of the Mrk 421 light curves in various energy bands . . . 93
7.14 Time asymmetry of Mrk 421 light curves during the 1998 campaign . . . 94
7.15 Spectral evolutions of Mrk 421 observed with *ASCA* (1993/1994) . . . 96
7.16 Spectral evolution 421 observed with *ASCA* (1998) . . . 97
7.17 Spectral evolutions of PKS 2155–304 observed with *ASCA* (1993/1994) . . 98
7.18 Spectral evolutions of 1ES 2344–514 observed with *ASCA* . . . 98
7.19 Discrete correlation function and time lag of Mrk 421 in 1993 . . . 100
7.20 Discrete correlation function and time lag of Mrk 421 in 1994 . . . 100
7.21 Discrete correlation function and time lag of PKS 2155–304 in 1993 . . . 101
7.22 Discrete correlation function and time lag of PKS 2155–304 in 1994 . . . 101
7.23 Time lag of Mrk 421 in 1998 . . . 102
7.24 Variability ratio and time lag for Mrk 421 (1998) . . . 103
7.25 *ASCA* SIS0 spectrum fitted to a power law function . . . 106

7.26 Confidence contour of spectral fitting for Mrk 421 (1998) . . . 107
7.27 Distribution of luminosities and photon indices for all observations with *ASCA* . . . 108
7.28 *ASCA* SIS0 spectrum fitted to a cutoff power law function . . . 111
7.29 Distribution of peak luminosity vs peak energy . . . 112
7.30 Synchrotron peak shifts of four TeV blazars . . . 114

8.1 Mrk 421 light curve in 1996–1997 (*RXTE*) . . . 118
8.2 Mrk 501 light curve in 1996–1998 (*RXTE*) . . . 119
8.3 PKS2155-304 light curve in 1996–1998 (*RXTE*) . . . 120
8.4 *RXTE* ASM light curves for four TeV blazars . . . 121
8.5 Variability amplitude of three TeV blazars (*RXTE*) . . . 122
8.6 Variability amplitude of PKS 2155–304 in 1996 May . . . 123
8.7 Light curves of PKS 2155–304 in 1996 May divided into 9 segments . . . 124
8.8 Variability amplitude of individual flares for PKS 2155–304 . . . 125
8.9 Structure functions of TeV blazars (*RXTE*) . . . 128
8.10 Symmetry of the PKS 2155–304 light curves in various energy bands . . . 129
8.11 Structure functions of TeV blazars (*ASCA* + *RXTE*) . . . 130
8.12 Spectral evolutions of PKS 2155–304 observed with *RXTE* . . . 132
8.13 *RXTE* PCA spectra fitted to a power law function . . . 134
8.14 Distribution of luminosities and photon indices for all observations with *RXTE* . . . 135
8.15 Comparison between *ASCA* and *RXTE* . . . 137
8.16 Synchrotron peak shifts of Mrk 421 . . . 138
8.17 Synchrotron peak shifts of Mrk 501 . . . 139
8.18 Synchrotron peak shifts of PKS 2155–304 . . . 140
8.19 Distribution of peak luminosity vs peak energy (*ASCA* + *RXTE*) . . . 141

9.1 X-ray and TeV γ-ray flux variation of Mrk 421 from 1995 to 1998 . . . 144
9.2 Multi-frequency variation of Mrk 421 during 1998 campaign . . . 145
9.3 X-ray and TeV γ-ray flux correlation of Mrk 421 . . . 146
9.4 UV and TeV γ-ray flux correlation of Mrk 421 . . . 146
9.5 Multi-frequency spectra of Mrk 421 . . . 147
9.6 X-ray and TeV γ-ray flux variation of Mrk 501 from 1995 to 1998 . . . 148
9.7 Time history of Mrk 501 during the March 1996 campaign . . . 149
9.8 X-ray and TeV γ-ray flux correlation of Mrk 501 in Apr/May 1997 . . . 150
9.9 X-ray and TeV γ-ray flux correlation of Mrk 501 . . . 151

9.10 Multi-frequency spectra of Mrk 501 152
9.11 X-ray and TeV γ-ray flux variation of PKS 2155−304 from 1995 to 1998 . 153
9.12 Multi-frequency spectra of PKS 2155−304 154
9.13 X-ray and TeV γ-ray flux variation of 1ES 2344+514 from 1995 to 1998 . . 155
9.14 Multi-frequency spectra of 1ES 2344+514 156

10.1 Comparison of PSD slopes for various black hole systems 158
10.2 A Gaussian fit to the time profile of PKS 2155−304 161
10.3 Measurement of the parameters describing the 1994 May flare of PKS 2155−304 162
10.4 Time profiles of a flare in various energy bands (Mrk 421 in 1998 #2) . . . 164
10.5 Time profiles of two different flares of Mrk 421 in 1998 165
10.6 Time profiles of a flare in various energy bands (Mrk 421 in 1998 #8) . . . 166
10.7 Fit with acceleration and cooling model 171
10.8 Self-similarity of rapid variabilities in Cyg X-1 and Mrk 421 173
10.9 Space VLBI map of Mrk 421 and Mrk 501 177
10.10Schematic view of spectral evolution of Mrk 501 181
10.11Definition of parameters from polynomial (cubic) fit 183
10.12Polynomial fit and allowed region for Mrk 421 188
10.13Polynomial fit and allowed region for Mrk 501 189
10.14Polynomial fit and allowed region for PKS 2155−304 190
10.15Polynomial fit and allowed region for 1ES 2344+514 191

11.1 Schematic view of the model adopted in this thesis 197
11.2 Schematic view of the division of the emission blob into 'slices' 199
11.3 Geometrical weight function of 'slices' 200
11.4 Evolution of the electron distribution injected at γ_0 201
11.5 Evolution of the electron distribution after the injection stop 202
11.6 SSC spectrum using the same parameters in Band & Grindlay (1985) . . . 203
11.7 Synchortron self-Compton spectra for various physical quantities 206
11.8 Analytical/numerical solution for time evolution of electron distribution . . 207
11.9 Spectral evolution of electrons for mono-energetic input 208
11.10Light curves of the flux for mono-energetic input 209
11.11Spectral evolution of photons for mono-energetic input 210
11.12SSC model fit and cooling rate of Mrk 421 215
11.13SSC model fit and cooling rate of Mrk 501 215
11.14SSC model fit and cooling rate of PKS 2155−304 216

11.15SSC model fit and cooling rate of 1ES 2344+514 216
11.16Simulated light curves of PKS 2155−304 218
11.17Detailed time history of PKS 2155−304 219
11.18Evolution of the X-ray spectrum of PKS 2155−304 220
11.19Measurement of the parameters describing PKS 2155−304 flare 221
11.20Multi-band spectrum of PKS 2155−304 222
11.21Modeling Mrk 421 flare due to the changes in δ 223
11.22Modeling Mrk 421 flare due to the changes in B 224
11.23Modeling Mrk 421 flare due to the changes in $\gamma_{\rm max}$ 225
11.24Modeling Mrk 421 flare due to the changes in q_e 226
11.25Simulation of a flare due to rapid electron acceleration 227
11.26Simulation of a flare due to gradual electron acceleration 228
11.27Simulation of a flare with long duration 229
11.28Modeling the spectral evolution of Mrk 501 in flare states 230
11.29Unified picture of rapid variability in TeV blazars (1) 232
11.30Unified picture of rapid variability in TeV blazars (2) 233

B.1 DCF of time-segment 2 for Mrk 421 in 1998 250
B.2 DCF of time-segment 3 for Mrk 421 in 1998 251
B.3 DCF of time-segment 4 for Mrk 421 in 1998 252
B.4 DCF of time-segment 5 for Mrk 421 in 1998 253
B.5 DCF of time-segment 6 for Mrk 421 in 1998 254
B.6 DCF of time-segment 7 for Mrk 421 in 1998 255
B.7 DCF of time-segment 8 for Mrk 421 in 1998 256
B.8 DCF of time-segment 9 for Mrk 421 in 1998 257

C.1 Errors on lags estimated from the Monte Calro simulations 260
C.2 Time lags of Mrk 421 in 1998 (de-trended) 261
C.3 Structure function of Mrk 421 during 1998 campaign (de-trended) 262

D.1 *ASCA* energy spectra of Mrk 421 (1) 264
D.2 *ASCA* energy spectra of Mrk 421 (2) 265
D.3 *ASCA* energy spectra of Mrk 421 (3) 266
D.4 *ASCA* energy spectra of Mrk 421 (4) 267
D.5 *ASCA* energy spectra of Mrk 501 (1) 267
D.6 *ASCA* energy spectra of Mrk 501 (2) 268
D.7 *ASCA* energy spectra of PKS 2155−304 (1) 269

D.8 *ASCA* energy spectra of PKS 2155−304 (2) 270
D.9 *ASCA* energy spectra of 1ES 2344+514 (1) 271

E.1 Synchrotron peak shifts of TeV blazars (1) 274
E.2 Synchrotron peak shifts of TeV blazars (2) 275

F.1 HEXTE spectra of Mrk 501 in 1998 May observation 277

H.1 *RXTE* spectra of Mrk 421 (1996−1997) 292
H.2 *RXTE* spectra of Mrk 501 (1996−1998) 293
H.3 *RXTE* spectra of PKS 2155−304 (1996−1997) 294
H.4 *RXTE* spectra of PKS 2155−304 (1998) 295

I.1 Schematic view of the cross section of a homogeneous sphere 298
I.2 Density of synchrotron photon distribution in a homogeneous source 300

List of Tables

4.1 Design parameters and performance of *ASCA* XRT 47
4.2 Design parameters and performance of *ASCA* SIS 48
4.3 Summary of observation modes in SIS 49
4.4 Design parameters and performance of GIS 53
4.5 Clock speed relating to time assignment of GISs 54

5.1 Design parameters and performance of *RXTE* PCA 59
5.2 Design parameters and performance of *RXTE* HEXTE 63
5.3 Design parameters and performance of *RXTE* ASM 65

6.1 TeV blazars observed with *ASCA* & *RXTE* 68
6.2 *ASCA* observation log of Mrk 421 69
6.3 *ASCA* observation log of Mrk 501 69
6.4 *ASCA* observation log of PKS 2155−304 70
6.5 *ASCA* observation log of 1ES 2344+514 70
6.6 List of simultaneous X-ray/GeV (EGRET) observations 73
6.7 List of simultaneous X-ray/TeV (*Whipple*) observations 74

7.1 Screening criteria for *ASCA* analysis 76
7.2 Image region for source and background spectrum 77
7.3 Fit results of *ASCA* spectra with a power law function plus absorption . . 105
7.4 Results of spectral fitting of Mrk 421 with a power law function plus absorption. 107
7.5 Fit result of *ASCA* spectra with a cutoff power law function 110
7.6 Results of spectral fitting of Mrk 421 with a cutoff power law function. . . 111

8.1 Screening criteria for *RXTE* analysis 116
8.2 An example of spectral fitting of Mrk 501 133
8.3 List of simultaneous X-ray observations by *ASCA* and *RXTE* 136

9.1 EGRET results for Mrk 501 150

10.1 Results of polynominal (cubic) fit 186
10.2 Input observables for individual TeV blazars 187
10.3 Output physical quantities for individual TeV blazars 192

11.1 Input model parameters for TeV blazars 213
11.2 Energy density of photons, magnetic field and electrons 217

A.1 *RXTE* observation log of Mrk 421 (1) 240
A.2 *RXTE* observation log of Mrk 421 (2) *continued* 241
A.3 *RXTE* observation log of Mrk 421 (3) *continued* 242
A.4 *RXTE* observation log of Mrk 501 (1) 243
A.5 *RXTE* observation log of Mrk 501 (2) *continued* 244
A.6 *RXTE* observation log of PKS 2155−304 (1) 245
A.7 *RXTE* observation log of PKS 2155−304 (2) *continued* 246
A.8 *RXTE* observation log of PKS 2155−304 (3) *continued* 247

F.1 Results of spectral fitting of HEXTE data 277

G.1 Fit results of *RXTE* spectra of Mrk 421 (1) 280
G.2 Fit results of Mrk 421 (2) *continued* 281
G.3 Fit results of Mrk 421 (3) *continued* 282
G.4 Fit results of *RXTE* spectra of Mrk 501 (1) 283
G.5 Fit results of Mrk 501 (2) *continued* 284
G.6 Fit results of Mrk 501 (3) *continued* 285
G.7 Fit results of *RXTE* spectra of PKS 2155−304 (1) 286
G.8 Fit results of PKS 2155−304 (2) *continued* 287
G.9 Fit results of PKS 2155−304 (3) *continued* 288
G.10 Fit results of PKS 2155−304 (4) *continued* 289
G.11 Fit results of TeV blazars with a cutoff power law function 289

Chapter 1

Introduction

Active Galactic Nuclei (AGN) produce enormous power (10^{40}∼10^{46} erg/s) from extremely compact volumes. They are commonly variable, and large luminosity variations on time scales of hours to years have been observed. From the combination of high luminosities and rapid time variability, it is generally believed that the ultimate source of power in AGN is accretion onto massive black holes (10^{7}∼$10^{10} M_{\odot}$) which exist at the centers of these powerhouses. The recent discovery of the clear, broad, skewed fluorescent iron line in the spectrum of MCG 6-30-15 with *ASCA* (Tanaka et al. 1995), as well as the high rotation velocities in a sub-parsec region of NGC 4258 (Miyoshi et al. 1995) from water-maser observation confirmed the existence of those massive black holes in AGN, and in some cases, allowed us to estimate their masses.

Blazars, a subclass of AGNs, have outstanding properties in several aspects. They exhibit the most rapid and the largest amplitude variations of all AGNs (Stein et al. 1976). Recent observations with the EGRET instrument (30 MeV−30 GeV; Thompson et al. 1993) on-board the *Compton Gamma-Ray Observatory* (*CGRO*) reveal that more than 60 AGNs are bright γ ray emitters (e.g., Mukherjee et al. 1997). Remarkably, all AGNs detected by EGRET were classified as blazars. Observations with ground-based Cherenkov telescopes further confirmed γ-ray emission extending up to TeV energies for four nearby blazars: Mrk 421 ($z = 0.031$; Punch et al. 1992), Mrk 501 ($z = 0.034$; Quinn et al. 1996), 1ES 2344+514 ($z = 0.044$; Catanese et al. 1998) and PKS 2155−304 ($z = 0.117$; Chadwick et al. 1999).

It has been reported that the overall spectra of blazars (plotted as νF_{ν}) have at least two pronounced continuum components: one peaking between IR and X rays, and another in the γ ray regime (e.g., von Montigny et al. 1995). The strong polarization observed in the radio and optical bands (Angel & Stockman 1980) implies that the lower energy component is most likely produced by synchrotron radiation of relativistic electrons in

magnetic fields, while inverse-Compton scattering by the same electrons is believed to be the dominant process responsible for the high energy γ ray emission (Ulrich, Maraschi, & Urry 1997; Ghisellini et al. 1998; see also § 2). This non-thermal radiation is thought to be emitted in a relativistic jet pointing close to our line of sight (e.g., Urry & Padovani 1995).

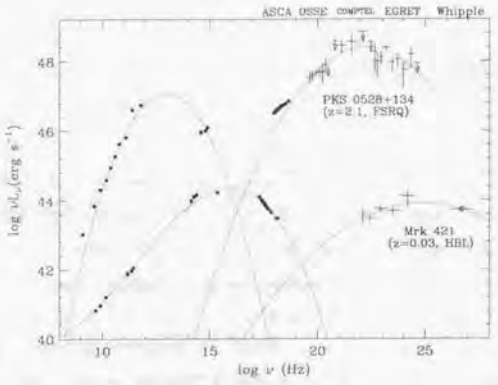

Figure 1.1: The multi-frequency spectra obtained from the contemporaneous observations of Mrk 421 and PKS 0528+134 (Kubo et al. 1998). The dotted line (intended as a guide to the eyes) shows the fit to a third-order polynomial function.

Multi-frequency spectra of blazars indicate their variety. Figure 1.1 shows the spectral energy distributions of Mrk 421 and PKS 0528+134, respectively. Mrk 421 is the prototype of TeV γ-ray emitting blazars, while PKS 0528+134 is the one of the brightest GeV emitting blazars that was observed by EGRET but has not been detected at TeV energies. One can find significant differences in their luminosities and peak positions of low-energy (LE) and high-energy (HE) components. Also note that the LE luminosity is larger than that of HE for Mrk 421, while the reverse applies for PKS 0528+134. Several authors have interpreted the difference as due to the different 'seed' photons for inverse-Compton scattering. Kubo et al (1998) suggested that the multi-frequency spectrum of Mrk 421 is well explained by the synchrotron-Self-Compton (SSC) scenario, in which the source of the 'seed' photons for the Compton process is pure synchrotron radiation internal to the jet (Jones et al. 1974; Marscher 1980; Königl 1981; Marscher & Gear 1985; Ghisellini & Maraschi 1989; Maraschi et al. 1992; Marscher & Travis 1996), while seed photons external to the jet play an important role for the case of PKS 0528+134 and other objects

showing strong broad emission lines (External Radiation Compton (ERC) model; Dermer & Schlickeiser 1993; Sikora, Begelman, & Rees 1994).

There are indications that particles are accelerated more efficiently in blazars having lower luminosities (e.g., Ghisellini et al. 1998; Kubo et al. 1998). In fact, the luminosity of Mrk 421 is significantly lower than that of PKS 0528+134, while the peaks of LE/HE components are located at much higher frequencies (Figure 1.1). In low luminosity objects, energy loss by radiative cooling would not be effective because there are less ambient photons to be Compton scattered to higher energies. Thus the TeV blazars gives an important opportunity to study the particle acceleration in blazar jets.

The first multi-frequency campaign of Mrk 421 including TeV energies was conducted in 1994 (Macomb et al. 1995; Takahashi et al. 1996). The contemporaneous observations implied correlated variability between the keV X-ray and TeV γ-ray emission, while the GeV flux and the radio to UV fluxes showed less variability. The results from this campaign are important because it suggested the possibility that a single electron population is responsible for both the X-rays and TeV γ-rays, qualitatively agreeing with the SSC scenario. However, the fact that the X-ray and TeV observations were separated by one day, could introduce uncertainties to draw concrete pictures. In fact, we now know that both X-ray and TeV γ-ray fluxes of Mrk 421 can vary significantly within a day. Simultaneous, uninterrupted observations are crucial to understand the blazar phenomenon.

In this thesis we intensively study the four TeV blazars, with an emphasis on the observations with the X-ray satellites *ASCA* and *RXTE*. Our main goal is to understand *both* the rapid time variability and spectral evolution of TeV blazars based on the high quality X-ray data. We analyze all the *ASCA* data obtained in 1993−1998, which covers the energy range 0.5−10 keV. To increase data samples in different states of source activity, we have also analyzed all the archival data of *RXTE* obtained in 1996−1998, where the energy range covered by the Proportional Counter Array (PCA) on-board *RXTE* is 2.5 keV to ∼20 keV.

Importantly, 30 observations presented in this thesis were conducted truly simultaneously with the *Whipple* Cherenkov telescope (TeV γ-ray) and 7 observations were simultaneous with EGRET (GeV γ-ray). In particular, an unprecedented campaign of Mrk 421 (7 days) is extremely valuable since this provides for the first time an uninterrupted and simultaneous data set including *EUVE*, X-ray (*ASCA* and *RXTE*) and TeV γ-ray energy bands. We also report another big campaign for PKS 2155−304 for 12 days by *RXTE*.

Unlike most of the previous work which focused on the photon spectral properties and/or classification of blazars, we also study the rapid time variability in blazars. Photon

spectra are important since they provide information on the distribution of relativistic electrons and the physical environment around the jet. On the other hand, the time variability gives us different constraints on the dynamics operating in blazar jets, such as the acceleration, radiative cooling and particle escape. It also gives us an information on the size of the emission region. To understand the observational data deeply, we develop a time-dependent numerical code that follows the time evolution of radiation from particles based on the one-zone homogeneous SSC model. Using the code, we compare the observational data directly to the prediction of the time-dependent model. Such a comparison is an important ingredient in the study of blazar activity.

In this thesis, we present the review of the past study on the AGNs and blazars in § 2. We give a brief description for theoretical frameworks which can be a guide to understand the radiation mechanism in blazars in § 3. We describe the instruments on-board *ASCA* satellite in § 4 and *RXTE* satellite in § 5. The log of *ASCA* and *RXTE* observations of four TeV blazars are described in § 6. We report the analysis and results of *ASCA* observations in § 7 and *RXTE* observations in § 8. The multiband properties of TeV blazars are described in § 9. We discuss our observational results and their implications in § 10. We develop a 'new' time-dependent SSC model in § 11 and compare it to the observational data. Finally, the conclusions are presented in § 12. Details are described in appendixes.

Chapter 2

Observational Properties of Blazars

2.1 Unifying Active Galactic Nuclei (AGN)

2.1.1 Classification of AGN

The Universe is made up of galaxies, many containing more than a hundred thousand million stars. 1−10 % of galaxies are called 'active' galaxies and possess an amazing source of energy at its nucleus (e.g., Ormes et al. 1996; Figure 2.1), generating the power comparable to that emitted by a thousand of galaxies. They are called an active galactic nuclei (AGNs).

AGNs produce enormous luminosities in extremely compact volumes. The combination of high luminosities (10^{40}∼10^{46} erg/s) and short variability time scales ($\leq$ 1 day) implies that the power of AGN is produced in more efficient way than ordinary stellar processes (e.g., nuclear fusion). This leads us to the hypothesis — which is widely believed — that the massive black holes are present in the central powerhouses, and that the accretion of matter onto such black holes is the origin of their high radiation power.

In general, an AGN emits not only visible light, but their emission spans a wide spectral range from radio to γ-rays. Furthermore, the most rapid time variability in AGN is observed in the X-ray and γ-ray energy bands. Since the integrated stellar light from a galaxy is emitted mainly in the IR/optical bands and relatively little of it is in the X-ray band, X-ray observations are an extremely important tool to 'look' inside the active galaxies.

In the broadest sense, galaxies in general are classified into two types, ellipticals or spirals. Independently, on the spectral grounds AGNs are classified into 'radio loud' and 'radio quiet' objects by their activity and/or luminosity in the radio band (Figure 2.1). About 10 % of AGNs are radio loud, and a 'jet' structure most frequently appears in the

radio VLBI image. Jets usually extend in opposite directions from the central core of the galaxy (see, Figure 2.2). BL Lac objects, the subject of this thesis, have strong radio emission, but also generally 'inhabit' elliptical galaxies. About 1000 blazars are known so far (see, also Veron-Cetty & Veron 1993).

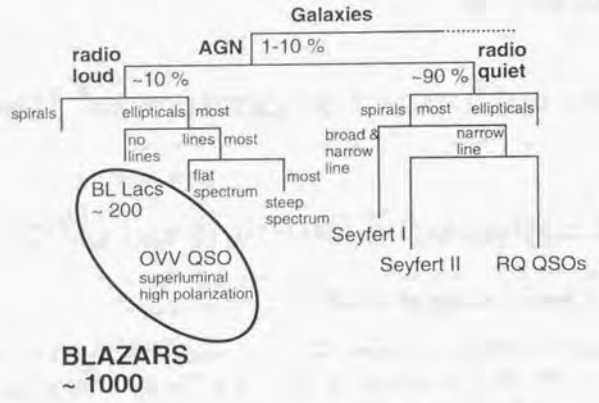

Figure 2.1: A categorization of active galactic nuclei (AGN). About 1–10 % of galaxies have active nucleus in their center. AGNs are furter classified into radio loud/quiet objects. Figure adopted from Ormes et al (1996).

2.1.2 Unified Picture of AGN

The radio quiet AGNs which are *not* associated with jet structure include Seyfert galaxies and radio quiet quasars as shown in Figure 2.1. The precise classification of Seyfert I, Seyfert II and the intermediate categories are discussed by Osterbrock (1981).

Recent intensive studies to unify AGNs can successfully impose some order on many types of AGN classes (e.g., Antonucci & Miller 1985; Antonucci 1993). Figure 2.2 shows a schematic picture of the unifying scheme of AGNs. The left panel summarizes the radio loud objects with jets, while the right is for the case of radio quiet objects without jets. The black hole, the accretion disk and the broad line region are surrounded by a molecular torus. Narrow line region (NLR) is thought to be the place that emits optical lines with narrow width. Broad line region (BLR) is believed to be inner part of the NLR. Due to the high velocity of clouds, optical lines emitted from this region form broad line structure. When the line of sight is between the jet axis and the torus plane, both the broad line

region and the narrow line region are visible; for galaxies with radio emission, these would be classified as broad line radio galaxies. When the broad line region is obscured by the torus, an object is observed as a narrow line galaxy. In this context, the observational differences between Seyfert I and II galaxies (and this holds independently of their radio loudness) are interpreted by the difference of line of sight between the jet axis and torus plane (e.g., Antonucci 1993).

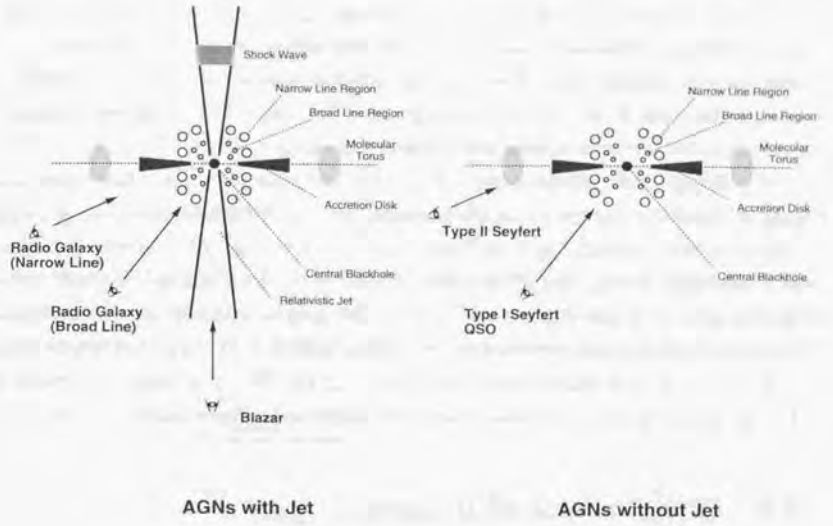

Figure 2.2: Unified scheme of all types of AGNs. *left panel*: AGNs having the jet, *right panel*: AGNs in absence of the jet.

2.1.3 Blazars – Roles in All AGN Classes

As it was mentioned above, some galaxies show strong radio emission, and those are called radio galaxies. We believe that most if not all radio galaxies have relativistic jets. However, the emission from the relativistic jet, due to the effects of relativistic light aberation (see, e.g., Rybicki and Lightman 1979), is only visible (and strongly amplified) if it is pointing close to our line of sight, and could be invisible if viewed close to the line of sight perpendicular to the direction of the jet. Blazars are the AGNs in which the line of sight lies close to the jet axis (Figure 2.2). VLBI observations reveal that many blazars

show superluminal motion of their jets: the apparent velocity of the blob sometimes well exceeds the light velocity ($v/c = 5 \sim 10$; Vermeulen & Cohen 1994). The superluminal motion can be explained by motion with speed close to c of the blobs at a small angle towards the observer (e.g., Blanford & Königl 1979).

Blazars are thus very different from other types of AGNs in a sense that the emission from the very inner part of the system (e.g., accretion disk, line emission region) is mostly overwhelmed by the strong jet emission. In fact, thermal X-ray emission from the accretion disk often observed in Seyfert galaxies and Galactic black holes (e.g., Dotani et al. 1997) is *not* observed in blazars, suggesting that the non-thermal jet emission is dominant for these sources. Polarization observed in the radio and optical band (Angel & Stockman 1980) further implies that most of the radiation in the radio - to UV band is non-thermal synchrotron radiation of relativistic electrons in the magnetic field.

The synchrotron radiation from radio to UV and sometimes X-ray bands indicates that the distribution of the relativistic electrons exists in the blazars' jets; these electrons cannot be mono-energetic. In some objects, an existence of extremely relativistic electrons with Lorentz factor $\gamma_{max} \sim 10^6$ (see below) is implied. Such high-energy electrons should rapidly cool via synchrotron radiation, hence continuous acceleration must occur. These acceleration/deceleration processes are very likely related to the large amplitude, rapid time variability often observed in blazars (see, § 2.2.2). Therefore, blazars are the only class of AGNs which provide information of dynamics operating in relativistic jets.

2.2 Observations of Blazars

2.2.1 Spectral Energy Distribution

Figure 2.3 shows the multi-frequency spectra of the well-studied TeV blazar Mrk 421 (Macomb et al. 1995; § 2.4.3). Open circles are data compiled from the archive, while filled diamonds are the data from the multi-wavelengh campaign in 1994 May (Macomb et al. 1995; see also below). Conveniently, the data points are plotted as Log(ν) versus Log(νL_ν), often used for multi-wavelength astronomy. This gives the source power per logarithmic frequency interval and thereby directly shows the relative energy output in each frequency band (Gehrels 1997). In this figure, the data taken within a week are plotted as 'simultaneous'.

One can find two important features from this figure. First, the multiband spectra of blazars, when plotted as νL_ν, show two pronounced continuum components. This is a common feature of all blazars detected with EGRET (von Montigny et al. 1995; Mukherjee et al. 1997). The low energy component (hereafter LE component) extends from the radio to UV, and sometimes extends to the X-ray bands. It is generally belived that the LE component is due to the synchrotron emission of relativistic electrons in magnetic field. The higher component (hereafter HE component) covers from the hard X-ray to TeV γ-ray energy bands, but its origin is less well understood. One promising explanation is inverse-Compton scattering of ambient photons, either internal or external to the jet. We will discuss various emission models which explain the HE component in § 2.3.

Blazars vary in all observable bands with large amplitude, and important clues to their structure and radiative properties lie in the correlations of flux variability in various spectral bands. For example, in the blazar Mrk 421, the keV X-ray and TeV γ-ray emission varied by an order of magnitude from their base values, while GeV γ-ray flux observed by EGRET, as well as the radio and UV fluxes, showed less variability than the keV or TeV bands. However, clear conclusions from the inter-band correlation could not be drawn because the X-ray observation by *ASCA* in this campaign was conducted one day after the TeV observation, and thus was not exactly simultaneous (Takahashi et al. 1996; 1999). In spite of the non-simultaneity of the observations, this campaign played an important role to give a strong motivation for subsequent multi-frequency campaigns of blazars.

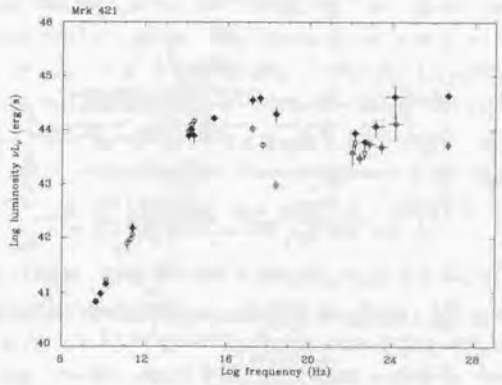

Figure 2.3: Spectral Energy Distribution of the TeV blazar Mrk 421 at multiple epochs including faint to flare states. Open circles are data taken before 1994 May in the quiescent state, while filled diamonds are data obtained in 1994 campaign (May 10−17) and plotted as 'simultaneous'. Figure from Macomb et al (1995).

2.2.2 Time Variability

One of the main characteristics of blazars is their rapid time variability with large amplitude. Flares have been observed in most wavelengths. Figure 2.4 shows time variation of TeV γ-rays of Mrk 501 from Quinn et al (1999). One can see that the large flux variations on time-scales from days to years. In particular, this source was in the historical high state during 1997 observations (see § 2.4.3). The maximum flux reached to ~ 4 Crab, which is about a factor 40 increase from the average flux of 1995 (Quinn et al. 1996). Most rapid time variability were found for this source whose doubling time of a few hours in 1997 data (Quinn et al. 1999).

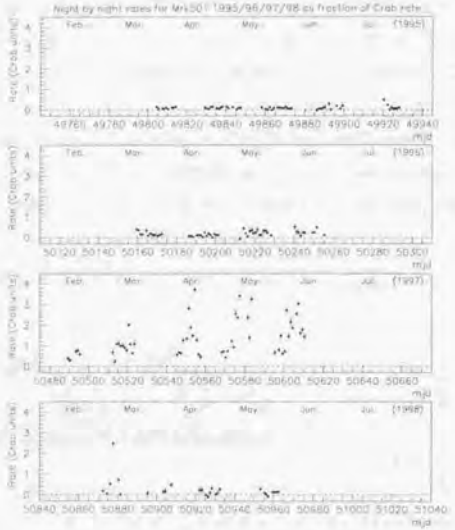

Figure 2.4: Average TeV γ-ray rates on daily time-scales for Mrk 501 between 1995 and 1998. Figure adapted from Quinn et al (1999).

Figure 2.5 show the X-ray light curves of PKS 2155−304 obtained with *BeppoSAX* in 1997 (Maraschi et al. 1999a; Zhang et al. 1999). Well-defined flare is clearly seen in the center, whose doubling time is about 3×10^4 sec (0.3 day). One can see the factor two variation in the lower energy X-rays (0.1−1.5 keV), and a factor three variation for higher energy X-rays (3.5−10 keV). The origin of the flare is completely unknown.

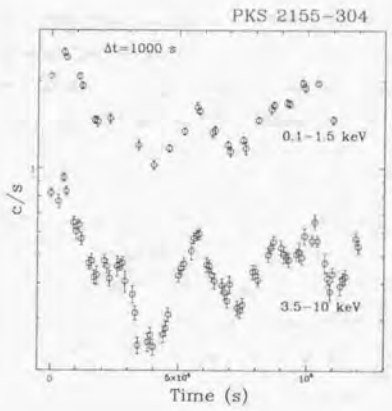

Figure 2.5: Light curves obtained from Nov 1997 observation of PKS2155-304 with *BeppoSax*. Quasi-symmetric flares are seen. Figure from Maraschi et al (1999).

2.2.3 X-ray Spectral Evolution

Another important discovery is the detection of the time lag between the soft X-ray and the hard X-ray band variations. This behaviour was first pointed out by Tashiro (1992) using the light curves from *GINGA* observations. He found that most of the X-ray variations exihibit canonical 'clockwise' hysteresis when plotted in flux versus photon index plane, which can be interpreted that the soft X-ray variation lags behind the hard X-ray variations both in an increasing and decreasing phases of intensity. This behaviour is expected for objects in which the X-ray emission is dominated by the synchrotron radiation.

This idea was verified during the *ASCA* observation of Mrk 421 in 1994, which was conducted as a part of the multi-frequency observations (Figure 2.3). The result indicated that the soft X-ray (≤ 1 keV) flux variation lagged behind that in the hard X-ray band (~ 2 keV) by 4 ksec. X-ray spectral evolution tracked a clearest 'clockwise' loop ever observed in the X-ray energy bands (Figure 2.6). Takahashi et al. (1996) associated the soft lag with the energy dependence of the synchrotron cooling time, deriving a magnetic field strength $B \sim 0.2$ G for $\delta = 5$. Importantly, this was the first case where the magnetic field was calculated only from the observed X-ray spectral variability.

The similar behavior was also detcted in other blazars (Kohmura et al. 1994; Tashiro

et al. 1995), leading to the *paradigm* that soft X-rays always lag behind the hard X-ray variations. However, the other types of the variations, e.g., *anti*-clockwise motion (e.g., PKS 2155−304: Sembay et al. 1993) or very small time-lag (e.g., PKS 2155−304: Edelson et al. 1995) have also been detected. Such an event was completely forgotten in the theoretical field until very recently (Kirk, Rieger & Mastichiadis 1998; see also § 2.3).

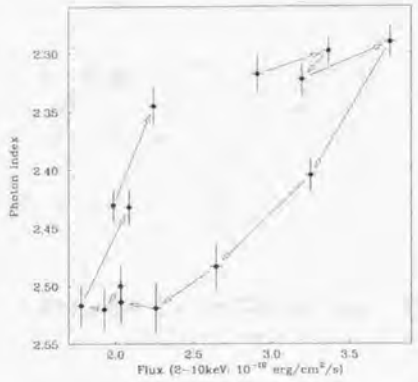

Figure 2.6: Hysteresis in a correlation between the flux and the photon index. A 'clockwise loop' is clearly seen. Figure from Takahashi et al (1996).

2.2.4 Implications on the Relativistic Beaming

Relativistic beaming is also suggested to avoid the so called "$\tau_{\gamma-\gamma}$" problem, related to the excessive optical depth (τ) to pair production for X-ray and γ-ray photons if one uses the variability time scale observed in blazars as the indicator of their size. In particular, several blazars detected by EGRET were extremely bright, whose isotropic luminosity would amount to $\sim 10^{49}$ (erg/s) (e.g., Figure 1.1). For these γ-ray bright blazars, if we assume that the radiation is isotropic and all photons are created in the same region of the size implied by the variability time scale, the value of τ well exceeds unity, hence γ-ray would *not* be observed. In order for GeV γ-rays to escape, emission region should be transparent to the γ-rays. This can be satisfied when the radiation is anisotropic, i.e., strongly beamed in a certain direction. For example, Mattox et al (1993) derived the lower limit of Doppler beaming factor as $\delta > 7.6$ for OVV quasar 1633+382.

Assume that there is an emission blob which radiates isotropically in the rest frame. In the observer's frame, the blob is moving with relativistic speed $\beta = v/c$ ($\sim$1), and the radiation is strongly anisotropic (e.g., Rybicki & Lightman 1979). Three important effects are expected (for more detail, see § 3.7). First, in the observer's frame, photons emitted from the moving source are concentrated in a narrow cone of half angle $\theta \sim 1/\Gamma$, where Γ is the Lorentz factor of emission blob in the observer's frame. Second, because of the difference in emission and arrival time intervals, the observed time scale is shortened by factor $\sim 1/\Gamma$. Third, since frequencies are the inverse of times, observed photon frequencies is blue-shifted by Γ.

Beaming factor δ is related with Γ as $\delta = [\Gamma(1-\beta\cos\theta)]^{-1}$ (see, § 3.7). If the observer lies close to the angles $\theta \sim 1/\Gamma$ from the jet axis, we have the relation of $\delta \simeq \Gamma$. Combining these relations, the total observed luminosity is enhanced by δ^4. The origin of this enhancement factor is easily understood as follows: factor δ^2 comes from the light aberration in solid angle, factor δ due to the blue shift of the frequency, and factor δ from the time dilation.

2.3 Jet Models for Blazar Emission

In this section, we summarize the emission models of blazars based on *leptonic* jet scenario. In the leptonic jet scenario, the electrons and positrons (hereafter, the term "electrons" refers to both electrons and positrons) are accelerated in the relativistic jets and produce both low-energy (LE) and high-energy (HE) components. Most of the current models agree in that the LE component is due to the synchrotron radiation of those high-energy electrons, while the source of the 'seed' photons for the Compton process producing HE component is a matter of debate. Various authors have considered various origin of the seed photons. These models are briefly summarized in the following and Figure 2.7.

There are completely different scenario in which *protons* are the primarily accelerated particles in the jet. This framework is called *hadronic* jet scenario. Even in the hadronic jet scenario, LE component is thought to be the synchrotron radiation from the electrons produced of hadronic cascade. Although the hadronic jet model is not considered in this thesis, we will briefly describe this model in § 2.3.3.

2.3.1 Leptonic Jet Models

SSC (Synchrotron-Self-Compton) Model

The first candidate for the 'seed' photons is the synchrotron radiation (i.e., LE component) produced in the jet (Jones et al. 1974; Marscher 1980; Königl 1981; Ghisellini & Maraschi 1989; Marscher & Travis 1996). In a most simple scenario, a single homogeneous

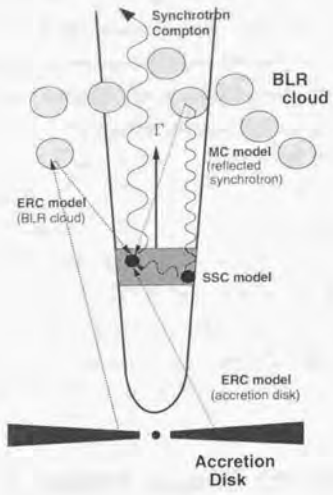

Figure 2.7: Illustration of the model geometry and the relevant γ-ray radiation mechanisms for leptonic jet models

region (spherical or slab geometry) emits both the synchrotron and inverse-Compton radiation (one-zone homogeneous model), as suggested by Gould (1979), Band & Grindlay (1985), and Inoue & Takahara (1996). More sophisticated model takes into account the inhomogeneity of the source, e.g., radial profile of the magnetic field and/or the propagating disturbance in the plasma jet flow (Marscher 1980; Marscher & Travis 1996; Georganopoulos & Marscher 1999).

Various authors have successfully interpreted the multi-frequency spectra of TeV emitting blazars by a simple one-zone homogeneous SSC model (e.g., Mastichiadis & Kirk 1997; Pian et al. 1998; Kataoka et al. 1999a). However, for the γ-ray bright OVV quasars, the γ-ray flux severely dominates the radiative output (e.g., PKS 0528+134; Figure 1.1), and an extremely strong beaming ($\delta \geq 100$) is necessary to account for the multiband spectra. Considering the *reasonable* beaming factor suggested by the VLBI observations ($5 < \delta < 30$), SSC scenario is thus highly unlikely for these bright OVV quasars (Kubo et al. 1998).

In OVV quasars, both X-ray and the γ-ray spectra are considered to be the Compton radiation from relativistic electrons. However, their multi-frequency spectra often show that the X-ray and the γ-ray spectra are not connected smoothly (e.g.,Figure 1.1; see

also Madejski et al. 1999 and Tanihata et al. 2000). This implies that both emissions are produced by the Compton process, but their seed photons are different. One of the candidates of the seed photons is the photons external to the jet, as discussed below.

ERC (External-Radiation-Compton) Model

The energy density of radiation produced externally to the emission blob may also be important for Compton scattering, since it is enhanced by relativistic beaming effect in the blob frame. In fact, the beaming pattern produced by radiation emitted isotropically in the blob frame (e.g., SSC process) is $\propto \delta^4$, while in the scattering of an external isotropic radiation field goes as $\propto \delta^6$ (Dermer 1995).

Various contributions for the *external* seed photons has been proposed; the radiation produced by an accretion disk (Dermer & Schlickeiser 1993), or reprocessed by the Broad Line Region (BLR) and/or scattered by material surrounding the jet (Sikora, Begelman, & Rees 1994; Blanford & Levinson 1995). Multi-frequency spectra of OVV quasars are well explained as the combination of SSC process and ERC process, with a reasonable beaming factor of $\delta \sim 10$ (Inoue & Takahara, 1996; Kubo et al. 1998; Takahashi et al. 1999).

MC (Mirror-Compton) Model

A portion of the broad line region (BLR; see § 2.7) could be illuminated by the beamed jet radiation, provided that some broad line clouds (or scattering material) exist in the vicinity of the jet (Ghisellini & Madau 1996). In different with other Compton scattering scenarios, this model predicts the flare in the γ-ray band (i.e., HE component) to lag the synchrotron outburst by $\sim L/c$, where L is the distance from the blob to the BLR region. It also predicts almost simultaneous variability at all γ-ray energies.

2.3.2 Time Dependent SSC Model

Theoretical models in previous sections have brought much success to understand the multi-frequency spectra of blazars from radio to γ-ray bands. However, we must note that these models are basically constructed on the *steady* state assumption, while blazars are highly variable in various energy bands (§ 2.2.2). Next step for the theoretical works is to understand the rapid time variability of blazars. It is only recently that several authors start to consider unified picture of blazars, taking both temporal and spectral evolutions into account. Successful results have been obtained for the simplest one-zone SSC model, but an application to the ERC and/or the MC models remains a future work.

Mastichiadis & Kirk (1997) and Dermer (1998) considered time-dependent SSC models where the variability is on time scales longer than R/c, R being the size of the emission region. One example of such calculations is illustrated in Figure 2.8 (Mastichiadis & Kirk 1997). Observational data come from Macomb et al. (1995; Figure 2.3). Assuming that electron injection spectrum is suddenly changed and then left constant, they calculated the time evolution of the electron and photon spectra for an arbitrary time. Left panel shows the time evolution of multi-frequency spectra, while right panel shows the changes in flux in various energy bands. In this particular case, they assumed that maximum Lorentz factor ($\gamma_{\rm max}$) of the electron population changed by factor of 5 in the 'new' equilibrium state.

Kirk, Rieger & Mastichiadis (1998) considered more sophisticated scenario where a thin shock front propagates through the emission region with a finite velocity v_s, supplying freshly accelerated electrons only in the front's vicinity. Most important discovery of their model is that the balance of acceleration and cooling processes plays an important role to determine blazar's variability, in particular at $\gamma \sim \gamma_{\rm max}$. They found that not only the usual clockwise hysteresis (Figure 2.6), but also the *anti*-clockwise hysteresis could be observed if the acceleration time is comparable with the cooling time scale.

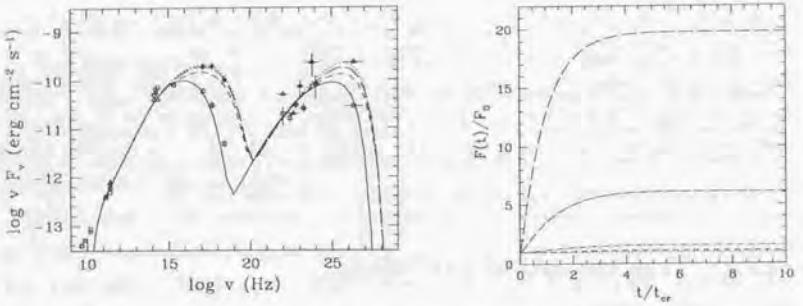

Figure 2.8: Time-dependent model for multi-wavelength spectrum and light curves of Mrk 421. Electron injection spectrum is assumed to be suddenly changed and then left constant. In this figure, maximum Lorentz factor of injected electron population are changed by factor of 5. *left*: Evolutions of multi-wavelength spectrum. Solid line is an initial state, while dotted line is the 'new' equilibrium state. *right*: Plot of the flux at various frequencies. The large dash line is 2–10 keV X-rays, while large dot-dash line is $>$ 500 GeV γ-rays. Figure from Mastichiadis & Kirk (1997).

2.3.3 Comment on the Hadronic Jet Model

Finally, we must note that there exists an alternative (or additional) scenario that AGN jets consists of normal hadronic matter ("proton jet" model; Mannheim & Biermann 1992; Mannheim 1993; Dar & Laor 1997). In this scenario, relativistic electrons can be injected by relativistic protons following nuclear interactions and/or photo-meson production process. Since the column densities in the jet plasma are too low to provide target for nuclear interactions, an external target has been proposed (Bednarek 1993). Such a model, however, may include several shortcomings as discussed in Sikora (1994) and Sikora et al. (1997).

First, the extremely low magnetic field in the target are required to avoid isotropization of accelerated protons before nuclear interactions. Second, in this scenario, it is only the third generation of particles which produces synchrotron radiation in the observable energy range. In this case, very fine tuning must be at work in order to obtain a third generation radiation component in the radio to X-ray bands. Third, such a compact region is expected to be opaque for GeV photons. Only for protons with energies above $\sim 10^9$ GeV, the radiation fields become opaque for photo-meson production process (Mannheim 1993). Following photo-meson production triggered by such protons, the synchrotron pair cascade develops. In this model, the break between X-rays and γ-rays is postulated to correspond with the break in the pair injection function. This model predicts the γ-ray energy index to be $\alpha_\gamma \geq 1$, which cannot explain steep γ-ray spectra observed with EGRET.

Finally, we should note that the prediction from the leptonic scenario is quite consistent with the observational data from radio to TeV γ-ray bands. Additional contribution from the accelerated protons, even if it exists, seems not very important. For these reasons, we do not consider the hadronic jet model in this thesis. Following discussion assumes the jet includes only leptons (i.e., electrons and positrons), or at least, radiation originated in hadronic interactions is assumed to be negligibly small.

2.4 TeV Blazars – Clue to the Jet Physics

2.4.1 Unifying Blazar Classes

As we see briefly in the previous section, blazars are classified into BL lac objects and OVV quasars. BL lac objects that have low-energy peaks in the IR/optical bands are called LBLs (low-energy peaked BL lacs), while BL lacs that have the peaks in the UV/X-ray band are called HBLs (high-energy peaked BL lacs) (e.g., Padovani & Giommi, 1995).

The first attempt to find regularities in the spectral energy distribution (SED) of blazars including γ-ray data, are performed by Kubo et al (1997; 1998) and Fossati et al (1998).

Kubo et al. (1997; 1998) fit the multi-frequency spectra of 18 blazars observed with *ASCA* by a cubic, leading to a conclusion that the difference of three types of blazars (HBLs, LBLs and OVV quasars) are primarily due to the different maximum Lorentz factors ($\gamma_{\rm max}$) of electrons. $\gamma_{\rm max}$ of OVV quasars were derived to be 10^3–10^4, while they were 10^5–10^6 for HBLs. They also found that the multiband spectra of HBLs are well explained by a simple SSC process, while the ERC process must be dominant for OVV quasars. Since BL lac objects is characterized with the lack of any emission lines in the optical band (Figure 2.1), contribution from the external radiation field should be much less than that in the OVV quasars. In such situation, they found that pure Synchrotron-Self-Compton (SSC) process is expected to be dominant.

Fossati et al (1998) collect data from literature for more than 50 sources and construct the SED of all these blazars. They divided the all sources in radio luminosity bins, averaging the data of the sources belonging to the same luminosity bin. The result is shown in Figure 2.9. Importantly, there seems a clear trend that as the total power decreases, both LE and HE components shift to the higher frequencies, and at the same time the γ-ray luminosity decreases its relative importance, reducing the bolometric output.

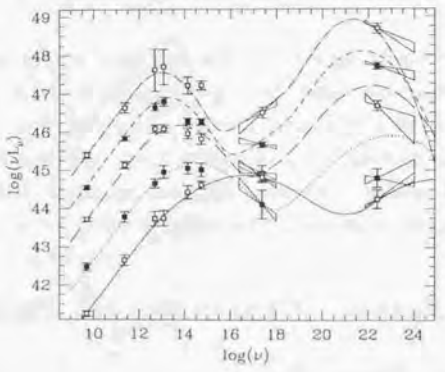

Figure 2.9: Unified picture of spectral energy distribution for all types of blazars. Figure from Fossati et al (1998).

Ghisellini et al. (1998) have collected a larger samples of 51 blazars and applied more

stringent theoretical models for blazars. They also associated the difference of three blazar classes with the difference in electron Lorentz factors. They found a tight correlation between the $\gamma_{\rm peak}$ ($\sim \gamma_{\rm max}$) and the amount of energy density U (both magnetic and radiative); $\gamma_{\rm peak} \propto U^{-0.6}$ (Figure 2.10). Importantly, this means that the energy loss rate of electrons ($\propto \gamma^2 U$; see § 3) is, at $\gamma_{\rm peak}$, nearly the same for all types of blazars. Since the acceleration and cooling is expected to be balanced at $\gamma_{\rm peak}$, this suggests the presence of some *universal* acceleration mechanism in blazar jets.

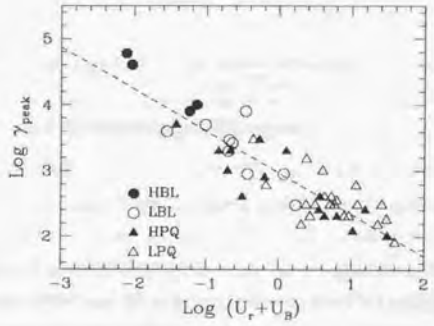

Figure 2.10: Correlation between $\gamma_{\rm peak}$ and the total (magnetic plus radiative) energy density. A tight correlation, $\gamma_{\rm peak} \propto U^{-0.6}$ was found. In this figure, QSO hosted blazars (QHBs) are defined as LPQ plus HPQ. Figure from Ghisellini et al (1998).

2.4.2 Extreme Particle Accelerators – TeV Blazars

As was suggested by Kubo et al. (1998) and Ghisellini et al. (1998), the typical values of $\gamma_{\rm max}$ are $\sim 10^3$ for OVV quasars, $\sim 10^4$ for LBLs and $\sim 10^5$ for HBLs, respectively. The unified picture of these blazar classes is illustrated in Figure 2.11. This figure represents the relation between luminosity (in the source frame) versus maximum Lorentz factor of electrons (Ghisellini et al. 1998). One can see that the HBLs are less luminous but have large $\gamma_{\rm max}$, which indicates that particle acceleration process is working most efficiently in HBLs.

Four TeV blazars are classified into HBLs, because their LE component reaches to the X-ray energy band. Detection of TeV γ-rays suggests a presence of electrons accelerated to extremely high energies, up to $\gamma_{\rm max} \geq 10^6$. This can be easily understood as follows.

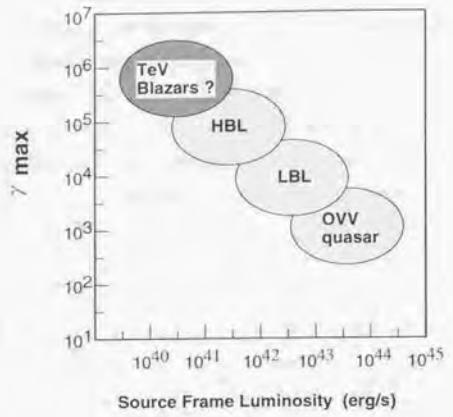

Figure 2.11: Unified scheme of all types of blazars. Figure adapted from Ghisellini et al (1998).

The maximum energy of high energy electrons is given as $\gamma_{max}\, m_e c^2$. From the argument of energy conservation between an electron and photon, this must be larger than the observed maximum photon energy measured in the source frame, i.e., $h\nu_{max}/\delta$. Since we have detected TeV γ-rays from these sources, the relation becomes $\gamma_{max}\delta \geq 10^7$. Assuming $\delta \sim 10$ for beaming factor, we expect that electrons are accelerated to more than $\gamma_{max} \sim 10^6$ at least in these TeV sources.

Since the cooling time when an electron loses its half of energy by synchrotron radiation is proportional to γ^{-1} (§ 3.3), most rapid variations can be observed for these TeV blazars. Any changes, such as variations in acceleration rate and/or the magnetic field, will be most sensitively observed at γ_{max}. Importantly, in the photon frequency space, this corresponds to the X-ray band for LE component and TeV band for HE component, both of which are known to show very steep spectra and large amplitude variability (§ 2.2.2). Thus the study of variability patterns and the spectral evolutions in X-ray and TeV bands provides direct information on dynamics operating in the jet (e.g., Kirk, Rieger,& Mastichiadis 1998).

A similar study could be also possible for QHBs and LBLs, but would probably be less conclusive, as these sub-classes of blazars exhibit a greater variety of spectral behavior. In particular, the X-ray and γ-ray bands (GeV regime in this case) corresponds to the lowest and the highest part of HE component, respectively, and thus *they sample different ends of the electron population*, which is in contrast to HBLs. In fact, X-ray variability

of QHBs and LBLs is known to be slower and less variable on short time scales (e.g., Kubo et al. 1998). TeV blazars promise to provide richest – but reasonably well measured – variety of both temporal and spectral evolution which at the same time is reasonably well understood in the context of the relatively simple SSC model, which points to diverse but relatively well-determined physical conditions in the jet rather than including additional effects due to geometry (e.g., beaming and orientation).

2.4.3 Individual Target

Mrk 421

Mrk 421 is very bright and highly variable in the X-ray band. Rapid variability in time scales as short as ≤ 1 day was repeatedly observed (e.g., Makino et al. 1987; George et al. 1988). X-ray spectrum is very steep, such that the photon energy spectrum in the X-ray band is well-described by a power law with the photon index $\sim 2-3$, although the spectral shape changes significantly during individual observations (Giommi et al. 1990; Makino et al. 1992; Comastri et al. 1997). It was also shown that the energy spectrum from radio to X-ray band connects smoothly, suggesting that the same emission mechanism (i.e., synchrotron radiation) is responsible for the radiative output from the entire radio - to X-ray regime (e.g., Urry 1984; Makino et al. 1987).

The advent of EGRET instrument and the observations by *Whipple* Cherenkov telescope brought a dramatical progress in the multifrequency study of this object. The γ-ray emission was first detected in the GeV band in 1991, but was very faint. The GeV flux was comparable to that of EGRET detection limit (Lin et al. 1992). Importantly, the spectral photon index in the GeV band was flat (≤ 2) and *not* connected smoothly to the X-ray spectrum. This was the first case which suggested that the both emissions have different origins, as predicted by the SSC scenario (see § 2.3).

After the EGRET detection, Mrk 421 was detected at TeV energies (Punch et al. 1992) by *Whipple* collaboration, being the *first* extragalactic TeV source detected at that time. The initial detection indicated a 6 σ excess and the flux was approximately 30 % of the flux of the Crab Nebula above 500 GeV (Punch et al. 1992). TeV emission from Mrk 421 has now been confirmed by several other collaborations (e.g., Petry et al. 1996 for the *HEGRA* detection). The TeV spectrum was measured to be very steep, indicating the spectral photon index of ~ 3 (Petry et al. 1996; Aharonian et al. 1999). Many authors associated the peculiarity of Mrk 421 with the distance to the source. In fact, it is the closest BL lac objects whose redshift is 0.031, and thus least affected by DIRB (extragalactic diffuse Infrared background) absorption (see § 2.5).

The first multiwavelength campaign of Mrk 421, including γ-ray detectors, was conducted in 1994 from radio to TeV bands (Macomb et al. 1995; 1996). This campaign provided the best-sampled data ever known for Mrk 421. During this campaign, a TeV flare was detected, but the *ASCA* observation was conducted one day after the TeV flare (Kerrick et al. 1995; Takahashi et al. 1996). The EGRET also observed Mrk 421 for a week, but no significant variation in flux was detected (Figure 2.3). Another Mrk 421 multiwavelength campaign performed in 1995 revealed another coincident keV/TeV flare (Buckley et al. 1996; Takahashi et al. 1996b). Although the relative amplitudes of variability are different, the UV and optical bands also showed correlation during the flares. Unfortunately, the X-ray data were too sparsely sampled to resolve the rapid time variability during the observation (see, e.g., Figure 7.2).

Mrk 501

Mrk 501 was known to be a fainter and less variable BL lac object than Mrk 421 in the X-ray band. Except for an *EXOSAT* observation in 1986 (Giommi et al.1990), the variation time scale was always longer than one day. X-ray spectrum was steep, such that the photon energy spectrum was well-described by a power law with the photon index of ~ 2.6 (Makino et al. 1992; Comastri et al. 1997). The energy spectrum from radio to X-ray bands connected smoothly, again suggesting that same emission mechanism is dominant for the radiation in both energy bands (e.g., Urry 1984).

From 1991 to 1992, EGRET observed Mrk 501 three times, but no significant γ-ray emission was detected ($\leq 2\,\sigma$). Thus only upper limit on flux was available in the 2nd EGRET source catalogue (Fichtel et al. 1994). In parallel with EGRET observations, Mrk 501 was also part of an active program of observing extragalactic sources by the *Whipple* collaboration. Prior to the detection in the GeV band, in 1995, it was detected as the *second* extragalactic source that emits TeV γ-rays (Quinn et al. 1996). The sum of 1995 data indicated the marginal evidence for detection at 9 σ level and the flux was approximately 10 % of the flux of the Crab Nebula above 350 GeV (Quinn et al. 1996). The TeV spectrum was measured to be steep, but flatter than Mrk 421. The spectral photon index was ~ 2.5 (Petry et al. 1997; Samuelson al. 1998). Notably, Mrk 501 is the second closest TeV-emitting BL Lac object ($z = 0.034$).

The first multiwavelength observations of Mrk 501, which included γ-ray detectors, were conducted in 1996 (Kataoka et al. 1999a). The observations were conducted with optical, *ASCA* , EGRET, and *Whipple* telescopes, although the GeV γ-ray was not detected at that time. The observations were well-scheduled and simultaneous from optical to TeV bands. The X-ray flux observed with *ASCA* was five times higher than that obtained

with *GINGA* (Makino et al. 1992) and the photon energy spectrum was harder. More importantly, during this campaign, EGRET detected Mrk 501 with a significance of 3.5 σ above 100 MeV (Kataoka et al. 1999a). Follow up observations established more strongly the detection of Mrk 501 by EGRET, with a marginal significance of 4.0 σ above 100 MeV but a significance of 5.2 σ above 500 MeV, indicating a hard GeV photon spectrum of the photon index of 1.3 ± 0.5.

The multiwavelength observations of Mrk 501 including TeV telescopes repeated after the success in 1996. During 1997 April campaign, a dramatical flare was observed in both X-ray and TeV bands (e.g., Catanese et al. 1997; Pian et al. 1998). Those results implied that the keV and TeV variations are well correlated, and X-ray spectrum becomes hardest among the HBLs (photon index at 2 – 10 keV was ~ 1.7; Pian et al. 1998). Pian et al (1998) pointed out the shift of synchrotron peak (peak of LE component) by a factor of 100, which is the largest shift ever observed in blazars.

PKS 2155−304

PKS 2155−304 is a bright X-ray blazar, showing a rapid variability on time-scale of hours (e.g. Treves et al. 1989; Tagliaferri et al. 1991; Chiapetti et al. 1999; Zhang et al. 1999). It is also one of the brightest extragalactic EUV sources. A large number of intensive multiwavelength campaigns have been conducted, but those observations did not include γ-ray detectors (e.g., Edelson et al. 1995; Urry et al. 1997). The energy spectrum from radio to X-ray band connects very smoothly, suggesting that both emissions are due to the same origin (e.g., Urry 1984; Treves et al. 1989). The photon energy spectrum is well-described by a power law with the photon index $\sim 2 - 3$, but highly variable (e.g., Sembay et al. 1993)

EGRET observed PKS 2155−304 six times from 1991 to 1993, but no significant emission was detected. However, during 1994 observation, it was detected for the first time at 6 σ level (Vestrand, Stacy, & Sreekumar 1995). Furthermore, higher GeV flux was observed during 1997 observation, implying a GeV flux increase by a factor of 3 (Sreekumar & Vestrand, 1997). The spctral photon index in the GeV band was measured to be 1.7 ± 0.2, more flatter than that of the X-ray spectrum (Vestrand, Stacy & Sreekumar, 1995).

The TeV emission from PKS 2155−304 was detected only recently, probably due to its southern location (Chadwick et al. 1999). *Durham Mark 6* Cherenkov telescope repeatedly observed PKS 2155−304 from 1996 to 1997, and obtained an evidence for TeV emission with marginal significance of 6.8 σ. Although other telescopes located in the Southern Hemisphere, e.g., CANGAROO collaboration, have not confirmed the detection, PKS 2155−304 is now believed to be the *fourth* TeV emitting blazar. It should be noted

that PKS 2155−304 is more distant ($z = 0.117$) than Mrk 421 and Mrk 501, and thus the most crucial test on DIRB will be achieved for this source in the future work.

Since both GeV and TeV emission was detected only recently, no multiwavelength campaign including γ-ray detectors was reported. The time variability was greatly different in different epochs. During 1991 campaign, 10 % flux change was observed *coherently* from optical to X-ray bands, with no significant time lags (Edelson et al. 1995). However in 1994 campaign, the amplitude of variation was strongly frequency dependent — flare of a factor 2 in the X-ray band, while smaller amplitude variations in UV bands were observed with significant time lags (Urry et al.1997). Considering the latter campaign has only short coverage between UV and X-ray observations, it seems speculative to put emphasis on the time lag. However, these observations suggest the variety of flares which are probably due to the different physical origin.

1ES 2344−514

1ES 2344+514 is one of the few known BL lac objects. It was first detected in the *Einstein* Slew Survey (Elvis et al. 1992). 1ES 2344+514 was only recently identified as a BL lac object (Perlman et al. 1996), by the lack of optical emission lines whose equivalent width greater than 5Aand its Ca II 'break strength' being smaller than 25 %. The former eliminates the possibility of the source as a quasar, while the latter criteria is indicative of the presence of a power law continuum. Perlman et al. (1996) determined the redshift of this object ($z = 0.044$) based on absorption lines, since it had no evident emission lines.

1ES 2344+514 is identified as the third closest known BL Lac object, after Mrk 421 and Mrk 501. Perlman et al. (1996) derive a 2 keV X-ray flux as roughly 1/3 the flux detected for Mrk 421 and Mrk 501. Measurements taken with the Very Large Array radio interferometer indicate that its radio emission is 'point-like,' with more than 80% of its flux being from an unresolved point source (Patanik et al. 1992; Perlman et al. 1996). The 5 GHz radio flux is about 1/3 and 1/4 of the flux of Mrk 421 and Mrk 501, respectively.

The EGRET observed 1ES 2344+514, but has not detected it. The preliminary upper limit on the GeV flux, derived from the private communication with the EGRET team, is presented in Catanese et al. (1998). 1ES 2344+514 was, however, detected by *Whipple* collaboration as the *third* extragalactic source succeeding to Mrk 501 (Catanese et al. 1998). The evidence for emission from 1ES 2344+514 comes mostly from an apparent flare on 1995, with a significance of 6 σ excess. This corresponds to about the 60 % of the Crab flux. However, follow up observations taken between 1995 and 1996 showed a fainter flux, crresponding to 10 % of the Crab Nebula, and no significant flux was observed between 1996 to 1997, indicating the source is highly variable in the TeV energy band.

Although no simultaneous campaigns have been conducted so far, best quality data in the X-ray band were obtained very recently by *BeppoSAX* observations (Giommi et al. 1999). They detected a flux variation on a time scale as short as ≤ 1 day. The X-ray photon spectrum was well represented by a power law form, with photon index ranged from 1.8 to 2.3.

2.5 Effects by the DIRB

There exist HBLs whose multiband properties are very similar to those of TeV blazars, but which are *not* detected at TeV energies yet. It should be noted that four TeV blazars detected at present are all low-redshift BL Lac objects. In fact, Mrk 421 is the closest BL lac objects ever known. This naturally suggests that the detectability at TeV energy band may be dependent on the distance to the source. Many authors pointed out that TeV γ-rays from the high-redshift sources are probably absorbed by the interaction with extragalactic diffuse infrared background (DIRB; e.g., Stecker et al. 1992). This interpretation is very likely, however, main difficulty is that the flux of the DIRB has not been determined experimentally due to large systematic errors driven by local effects (Figure 2.12). Some authors suggest that the TeV energy spectrum of blazars can be viable to derive the upper limit on DIRB, but this still involves large systematic errors in the estimation (e.g., Funk et al. 1998; Figure 2.12).

Thus the effects of DIRB on the photon spectra of TeV emitting blazars is now still under debate. We show one example presented by Stecker et al. (1998) in Figure 2.13. According to their model, optical depth for TeV−IR absorption is less than unity below 10 TeV for Mrk 421 and Mrk 501, both at redshift of ~ 0.03. This indicates that no significant curvature would be appearent in the TeV γ-ray spectra obtained with ground-based Cherenkov telescopes. However, the intrinsic spectra of these sources should be harder by amounts of ~ 0.25 to 0.45 in the spectral index (in the 1 to 10 TeV range), with an intergalactic absorption cutoff above 20 TeV.

In this thesis, we proceed under the assumption that the effect of absorption by DIRB is negligibly small for all TeV blazars. This approximation is probably valid for *Whipple* observations of Mrk 421 and Mrk 501 ($z \simeq 0.03$), because the energy threshold of the detector is 0.35 TeV and most of the photons are detected below 1 TeV (Figure 2.13). However, for the most distant TeV blazar PKS 2155−304 ($z = 0.117$), optical depth becomes ~ 1 at 1 TeV (Figure 2.13), which may lead to an underestimation of absolute TeV flux by factor $\sim$2, altough this is still consistent within the measurement error (Chadwick

et al. 1999).

We also note that, even if absorption by DIRB is more important than the estimation given by Stecker et al. (1998), *relative* amplitude of variation in the TeV flux is *not* affected unless DIRB itself is variable in time. Thus the study of inter-band correlation between X-ray and TeV γ-rays described in § 9 is not affected by the DIRB absorption.

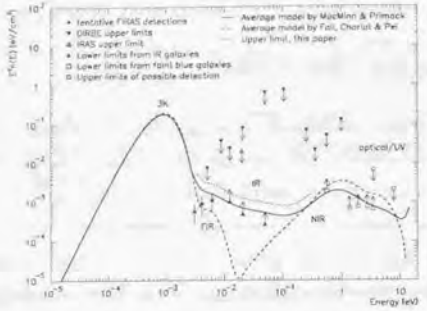

Figure 2.12: Energy density of the DIRB. *Solid line* and *dashed line* : theoretical models for DIRBs. *Dotted line* : upper limit from the TeV energy spectra of Mrk 501. Figure from Funk et al (1998).

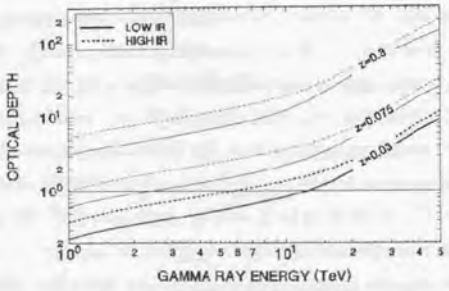

Figure 2.13: Optical depth vs energy for γ-rays originating at various redshifts. Figure from Stecker et al (1998).

Chapter 3

Emission Mechanism of Blazars

3.1 Energy Gain Processes

In this section, a simple theory for particle acceleration at a shock front is introduced as a possible energy gain process of electrons in blazar jets. The following treatment of Fermi acceleration is based on Gaisser (1990) and Protheroe (1996). More detailed and rigorous treatments are given in the literature (e.g., Blanford & Eichler 1987).

3.1.1 2nd order Fermi Acceleration

Assume that there are magnetized clouds moving with speed V (Figure 3.1). A charged particle enters the cloud and scatters off irregularities in the magnetic field which is tied to the cloud. In the frame comoving with cloud, there is no change in energy of the particle because the scattering is collisionless, however, the direction of the particle is randomized by the scattering with clouds in a random direction. We consider a charged particle entering a cloud with energy E_1, momentum p_1, moving in a direction θ_1 related to the cloud's direction. After scattering has occured, it emerges with E_2, momentum p_2, in a direction θ_2 relative to cloud's direction. By applying Lorentz transformations between the observer's frame (unprimed) and the cloud frame (primed), we obtain the fractional energy change in particle energy $(E_2 - E_1)/E_1$,

$$\frac{\Delta E}{E} = \frac{1 - \beta\cos\theta_1 + \beta\cos\theta_2' - \beta^2\cos\theta_1\cos\theta_2'}{1 - \beta^2} - 1, \tag{3.1}$$

where $\beta = V/c$. Since particles and clouds move randomly in direction, average values of $\cos\theta_1$ and $\cos\theta_2'$ are important. Inside the cloud, the direction of the charged particle will be completely randomized by multiple scatterings, such that $<\cos\theta_2'> = 0$. The average value of $\cos\theta_1$ depends on the rate of collision, which is proportional to the relative velocity

between the cloud and particle. Thus probability per unit solid angle of having a collision at angle θ_1 is proportional to $v - V\cos\theta_1$, where v ($\simeq c$) is the velocity of particle. We obtain

$$< \cos\theta_1 >= \int \cos\theta_1 \frac{dP}{d\Omega_1} d\Omega_1 / \int \frac{dP}{d\Omega_1} d\Omega_1 = -\frac{\beta}{3}, \tag{3.2}$$

giving

$$\frac{< \Delta E >}{E} = \frac{1 + \beta^2/3}{1 - \beta^2} - 1 \simeq \frac{4}{3}\beta^2. \tag{3.3}$$

This result shows the particle gains energy from the cloud, but the average gain is small because $\beta \ll 1$ in ordinary cases.

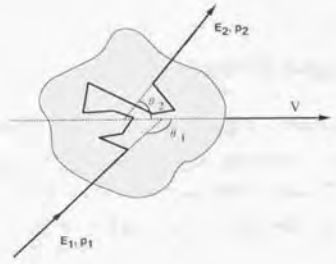

Figure 3.1: Schematic view of 2nd order Fermi Acceleration.

3.1.2 1st order Fermi Acceleration

More efficient acceleration (1st order in β) can take place when a shock propagates through the plasma, and charged particles cross the shock front iteratively from downstream to upstream, and upstream to downstream. This situation is expected in many astrophysical situations, such as supernova explosion in the interstellar medium or relativistic jets associated with extragalactic and/or galactic sources. A schematic view of acceleration at shock front is given in Figure 3.2. In this case, the probability per unit solid angle of having a collision at angle θ_1 is proportional to $\cos\theta_1$, while the probability is proportional to $\cos\theta_2'$ after the scattering. Thus we obtain $<\cos\theta_1> = -2/3$ and $<\cos\theta_2'> = 2/3$. In this case, one finds from equation (3.1)

$$\frac{< \Delta E >}{E} \simeq \frac{4(R-1)}{3R}\frac{V_s}{c} \simeq \frac{4}{3}\beta, \tag{3.4}$$

where V_s is the shock velocity, $R = u_1/u_2$ is the compression ratio, $u_1 = V_s$ and u_2 are the upstream and downstream velocities in the rest frame of the shock. For a strong shock in

a mono-atomic gas (e.g., fully ionized plasma), $R_c = 4$ is expected from Rankine-Hugoniot relation.

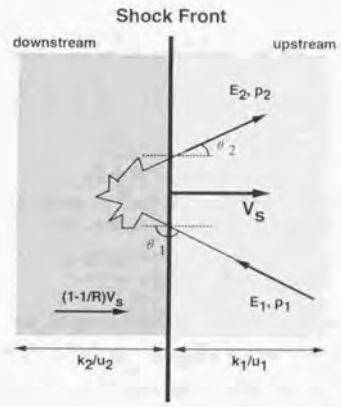

Figure 3.2: Schematic view of 1st order Fermi Accceleration.

3.1.3 Acceleration Rate

A net flow of the energetic particles, which are escaping from the shock front, is calculated as

$$r_{\rm loss} = n_{\rm cp} u_2 = n_{\rm cp} \frac{V_s}{R}, \tag{3.5}$$

where $n_{\rm cp}$ is the number density of particles at the shock. In the upstream of the shock, a charged particle moving at speed v at angle θ to the shock normal (in the observer's frame) approaches the shock with speed $V_s + v\cos\theta$ in the shock frame. To cross the shock, $\cos\theta > -V_s/v$ is required. Thus the rate at which particles cross the shock from upstream to downstream is calculated assuming isotropic distributions of particles

$$r_{\rm cross} = n_{\rm cp}\frac{1}{4\pi}\int_{-V_s/v}^{1}(V_s + v\cos\theta)d(\cos\theta)\int_0^{2\pi} d\phi = n_{\rm cp}\frac{v}{4}. \tag{3.6}$$

We obtain the probability of crossing the shock front once and then escaping from the acceleration process as the ratio of these two rates,

$$\text{Prob(escape)} = \frac{r_{\rm loss}}{r_{\rm cross}} = \frac{4}{R}\frac{V_s}{v}. \tag{3.7}$$

By defining the time $t_{\rm cycle}$ for one complete cycle, i.e., from crossing the shock from upstream to downstream, diffusing back towards the shock and crossing from downstream

to upstream, with enegy gain $<\Delta E>$, we can define the acceleration rate and escape rate per shock crossing as

$$r_{\rm acc} = \frac{1}{E}\frac{dE}{dt} = \frac{<\Delta E>}{E}\frac{1}{t_{\rm cycle}}, \tag{3.8}$$

$$r_{\rm esc} = \frac{\rm Prob(escape)}{t_{\rm cycle}} \simeq \frac{4}{R}\frac{V_s}{c}\frac{1}{t_{\rm cycle}}. \tag{3.9}$$

Combined this with equation (3.4), one obtains the relation

$$\frac{r_{\rm esc}}{r_{\rm acc}} \simeq \frac{3}{R-1}. \tag{3.10}$$

Note that for a strong shock case ($R = 4$), the two rates are equal.

3.1.4 Diffusion Coefficient

The cycle time for the acceleration process depends on particle diffusion, as well as the shock velocity. We first consider the diffusion in the downstream direction. The typical distance of a particle diffusion in time t is given as $\sqrt{k_2 t}$, where k_2 is the diffusion coefficient in the downstream region. The distance advected in this time is simply $u_2 t$. If $\sqrt{k_2 t} \gg u_2 t$, it is very probable that the particle will return to the shock, but if $\sqrt{k_2 t} \ll u_2 t$, the particle will never come back. By setting $\sqrt{k_2 t} = u_2 t$, we obtain the boundary distance $d = k_2/u_2$ from the shock front in the downstream direction, where inside of this, the particle will effectively return to the shock front. There exist $n_{\rm cp} k_2/u_2$ particles per unit area, between the shock front and this boundary. Dividing this by the ratio $r_{\rm cross}$, one finds the average time spent downstream before returning to the shock

$$t_{\rm cycle}^{\rm down} \simeq \frac{4}{c}\frac{k_2}{u_2}. \tag{3.11}$$

Similary, the other half of the cycle after the particle has crossed the shock from downstream to upstream is easily obtained. In this case, one can define a boundary at a distance k_1/u_1 upstream of the shock, leading to

$$t_{\rm cycle}^{\rm up} \simeq \frac{4}{c}\frac{k_1}{u_1}. \tag{3.12}$$

Thus the total cycle time $t_{\rm cycle}$, the acceleration rate $r_{\rm acc}$, and the acceleration time $t_{\rm acc}$ ($\equiv 1/r_{\rm acc}$) are respectively

$$t_{\rm cycle} \simeq \frac{4}{c}(\frac{k_1}{u_1} + \frac{k_2}{u_2}), \tag{3.13}$$

$$r_{\rm acc} \simeq \frac{(R-1)u_1}{3R}(\frac{k_1}{u_1} + \frac{k_2}{u_2})^{-1}, \tag{3.14}$$

$$t_{\rm acc} \simeq \frac{3R}{(R-1)u_1}(\frac{k_1}{u_1} + \frac{k_2}{u_2}). \tag{3.15}$$

3.1.5 Energy Spectrum

Assume that the diffusion coefficients upstream and downstream have the same power law dependence ξ on energy, i.e.,

$$k_1 \propto k_2 \propto E^{\xi}, \tag{3.16}$$

then the acceleration rate $r_{\rm acc}$ and the escape rate $r_{\rm esc}$ also have a power law dependence (see equation (3.10) and (3.14)),

$$r_{\rm acc} \propto r_{\rm esc} \propto E^{-\xi}. \tag{3.17}$$

In the following, we consider the case of ignoring losses due to radiative cooling (e.g., synchrotron cooling) or any other processes. We define the acceleration/escape rate

$$r_{\rm acc} = aE^{-\xi}, \tag{3.18}$$

$$r_{\rm esc} = cE^{-\xi}, \tag{3.19}$$

where a and c are constants. From equation (3.8), the particle energy at time t is determined from a differential equation

$$dE/dt = aE^{1-\xi}, \tag{3.20}$$

giving

$$E(t) = (E_0^{\xi} + \xi a t)^{1/\xi}, \tag{3.21}$$

where E_0 is the particle energy at time t=0. The number of particles remaining inside the shock front at time t after injection is calclulated by solving

$$dN/dt = -N(t) r_{\rm esc} = -N(t) c E(t)^{-\xi}. \tag{3.22}$$

The solution of this equation is

$$N(t) = N_0 [E(t)/E_0]^{-c/a}. \tag{3.23}$$

Since $N_0 - N(t)$ particles have escaped from the shock front before time t, having energies between E_0 and $E(t)$, the differential energy spectrum of particles which have escaped from the shock front is given as

$$dN/dE = N_0 (s-1) E_0^{-1} (E/E_0)^{-s}, \qquad (E_0 < E < E(t)) \tag{3.24}$$

where $s = (1 + c/a)$ is the differential spectral index. It should be noted that for the strong shock case ($r_{\rm esc} = r_{\rm acc}$), one obtains the standard result for shock acceleration, $s = 2$.

3.2 Energy Loss Processes

While the electrons gain energy from the shock, they also suffer from many kind of energy-loss processes. Because of the very wide energy distribution of electrons and the different dependence on energy of each cooling process, it is important to discuss which process cools electrons more effectively. We first consider four cooling processes — (1) synchrotron cooling, (2) inverse Compton scattering, (3) Coulomb losses, and (4) bremsstrahlung. In the following, we evaluate the energy losses $b(\gamma)$, for a single electron.

High-energy electrons in a magnetic field emit synchrotron radiation (e.g., Rybicki & Lightman (1979); see also equation (3.34))

$$b_{\rm sync} = \frac{4\sigma_{\rm T}\gamma^2 U_B}{3m_e c} = 1.29\times10^{-9}B^2\gamma^2 \qquad [{\rm s}^{-1}], \tag{3.25}$$

where $U_{\rm B}$ is the energy density in the magnetic field and $\sigma_{\rm T}$ is the Thomson cross section.

Similarly, the inverse Compton cooling rate $b_{\rm IC}$ is given by (e.g., Rybicki & Lightman 1979; see also equation (3.47))

$$b_{\rm IC} \simeq \frac{4\sigma_{\rm T}\gamma^2 U_{\rm ph}}{3m_e c} \qquad [{\rm s}^{-1}], \tag{3.26}$$

where $U_{\rm ph}$ is the soft photon density to be up-scattered.

The relativistic electrons will also lose their energy by interactions with the thermal plasma. The Coulomb losses due to collisions with charged particles give a loss rate which is approximately (e.g., Rephaeli 1979),

$$b_{\rm Coul} \simeq 1.2\times10^{-12}n_e[1.0+\frac{\ln(\gamma/n_e)}{75}] \qquad [{\rm s}^{-1}], \tag{3.27}$$

where n_e is the thermal electron density in the plasma.

The same collisions between high energy electrons and thermal particles also produce radiation thorough bremsstrahlung. The loss rate due to bremsstrahlung is given approximately (e.g., Blumental & Gould 1970)

$$b_{\rm brems} \simeq 1.5\times10^{-16}n_e\gamma[\ln\gamma+0.36] \qquad [{\rm s}^{-1}]. \tag{3.28}$$

We assume $B\simeq0.1-1.0$ G for a blazar jet. $U_{\rm ph}$ is estimated roughly from the luminosity in the source frame, $L\sim10^{40}-10^{42}$ erg/s (e.g., Kubo et al. 1998). Assuming the source radius $R\sim10^{16}$ cm, we obtain $U_{\rm ph}\sim10^{-4}-10^{-2}$ erg/cm^3. Although the thermal electron density in the blazar jet is completly unknown, we choose $n_e\sim10^{-3}-1$ cm^{-3}, which is appropriate for a typical intracluster medium and/or supernova remnants.

The results are summarized in Figure 3.3. One finds only two cooling processes, synchrotron cooling and inverse Comton scattering, can effectively influence the cooling

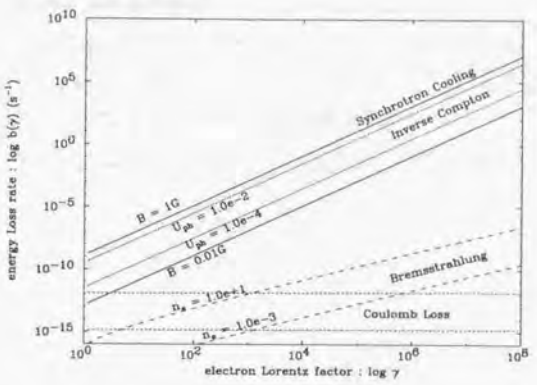

Figure 3.3: Energy loss rate $b(\gamma)$ from a single electron.

of the high-energy electrons. It should be noted that the result is essentially the same for any values of B, n_e and $U_{\rm ph}$ which are appropriate for blazars. Also note that the reduction of cross section in the Klein-Nishina regime would reduce the significance of inverse Compton losses at the high energy end ($\gamma\geq10^5$; see, Figure 3.8), but that it is still more important than Coulomb and bremsstrahlung. Thus we conclude that the synchrotron radiation and the inverse Compton scattering are the dominant energy loss mechanisms to be further investigated.

3.3 Synchrotron Radiation

We first consider synchrotron radiation process. There exist numerous articles and reviews which have treated this process in detail (e.g., Blumenthal & Gould 1970; Rybicki & Lightman 1979). Here we merely collect the formulae which will be used in our calculations. We also describe the details for the synchrotron emission from a homogeneous self-absorbed (i.e., optically thick) source in § 11 and Appendix I.

3.3.1 Emission from a Single Electron

A relativistic electron in a magnetic field B will radiate fairly broad emission with a total emitted power per frequency,

$$P(\omega,\gamma) = \frac{\sqrt{3}e^3 B\sin\alpha}{2\pi m_e c^2}F(\frac{\omega}{\omega_c}). \qquad [{\rm erg\ s^{-1}Hz^{-1}}] \tag{3.29}$$

where e and m_e are the charge and mass of an electron, respectively. γ is the Lorentz factor of the electron, and α is the angle between the magnetic field and the electron velocity. $F(x)$ is defined as

$$F(x) \equiv x \int_x^\infty K_{5/3}(\eta) d\eta, \tag{3.30}$$

where $K_{5/3}(x)$ is the modified Bessel functions of 5/3 order. ω_c is the critical frequency given as

$$\omega_c = \frac{3\gamma^2 eB\sin\alpha}{2m_e c}. \tag{3.31}$$

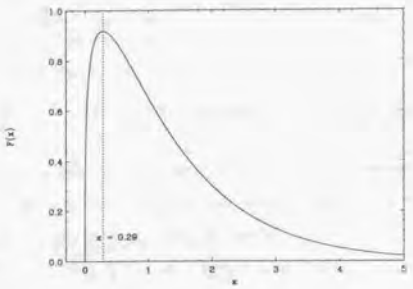

Figure 3.4: Synchrotron spectrum from a single electron as a function of $x \equiv \nu/\nu_c$.

We show the function $F(x)$ in Figure 3.4. Since $F(x)$ peaks at $x \simeq 0.29$, the peak frequency of the synchrotron emission by an electron with Lorentz factor γ is expressed as

$$\nu_p \simeq 1.2 \times 10^6 B\gamma^2 \sin\alpha. \tag{3.32}$$

Similary, the synchrotron frequency *averaged* over the spectral shape for an electron of Lorentz factor γ is

$$\nu_m \simeq 3.7 \times 10^6 B\gamma^2 \sin\alpha. \tag{3.33}$$

An integration of equation (3.29) over the frequencies gives the cooling rate of a single electron by the synchrotron radiation

$$\gamma_{\rm sync} = \frac{4\sigma_T \gamma^2 U_B}{3m_e c}, \tag{3.34}$$

where U_B is the magnetic field energy density and σ_T is the Thomson cross section.

3.3.2 Emission Coefficient : j_ν

Next we consider the synchrotron emission from electrons, whose number density per unit volume per unit energy is characterized by $N_e(\gamma)$. Electrons range from $\gamma_{\rm min}$ to $\gamma_{\rm max}$. The synchrotron emission coefficient $j_\nu(\nu)$ is derived straightforwardly from equation (3.29), noting that $\omega = 2\pi\nu$. We find the total emitted power per unit volume,

$$P_{tot}(\nu) = \int_{\gamma_{\rm min}}^{\gamma_{\rm max}} P(\nu,\gamma) N_e(\gamma) d\gamma. \tag{3.35}$$

For a distribution of randomly oriented emitters, we can write

$$j_\nu(\nu) = \frac{1}{4\pi} P_{tot}(\nu). \tag{3.36}$$

Thus we finally obtain

$$j_\nu(\nu) = c_2 B \int_{\gamma_{\rm min}}^{\gamma_{\rm max}} d\gamma N_e(\gamma) F(\frac{\nu}{c_1 B\gamma^2}), \tag{3.37}$$

where c_1 and c_2 are constants

$$c_1 = \frac{3e}{4\pi m_e c}, \qquad c_2 = \frac{\sqrt{3}e^3}{4\pi m_e c^2}. \tag{3.38}$$

We show examples of j_ν in Figure 3.5, for the magnetic field strength of 0.01 – 1.0 G. We assume a power law form for the electron population, $N(\gamma) = N_0\gamma^{-2}$ ($1<\gamma<10^8$). Note that, at most the frequencies, j_ν is distributed as a power law, $j_\nu \propto \nu^{-p}$, where $p = 0.5$ (e.g., Rybicki & Lightman 1979).

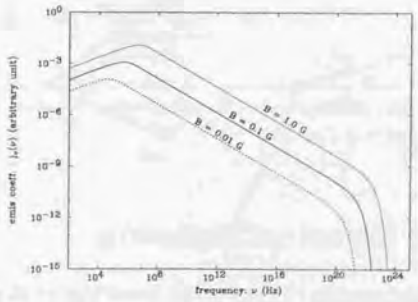

Figure 3.5: Emission coefficient j_ν of the synchrotron radiation for a power law electron population; $N(\gamma) = N_0\gamma^{-2}$ ($1<\gamma<10^8$).

3.3.3 Absorption Coefficient : α_ν

Synchrotron emission is accompanied by absorption, in which a photon interacts with an electron, giving up its energy. In a classical scheme of electrodynamics, where the absorbed photon energy is much smaller than that of the electrons, one finds a simple formula for the self-absoption coefficient. We obtain

$$\alpha_\nu(\nu) = -\frac{1}{8\pi\nu^2 m_e}\int_{\gamma_{\rm min}}^{\gamma_{\rm max}} d\gamma P(\nu,\gamma)\gamma^2\frac{\partial}{\partial\gamma}[\frac{N_e(\gamma)}{\gamma^2}]. \tag{3.39}$$

By replacing $P(\nu,\gamma)$ with equation (3.29), one finds

$$\alpha_\nu(\nu) = -\frac{c_3 B}{\nu^2}\int_{\gamma_{\rm min}}^{\gamma_{\rm max}} d\gamma\gamma^2\frac{\partial}{\partial\gamma}[\frac{N_e(\gamma)}{\gamma^2}]F(\frac{\nu}{c_1 B\gamma^2}), \tag{3.40}$$

where c_3 is a constant

$$c_3 = \frac{\sqrt{3}e^3}{8\pi m_e^2 c^2}. \tag{3.41}$$

Figure 3.6 shows examples of α_ν, for the same population of electrons with Figure 3.5. Note that α_ν is strongly dependent on energy, such that $\alpha_\nu \propto \nu^{-3}$.

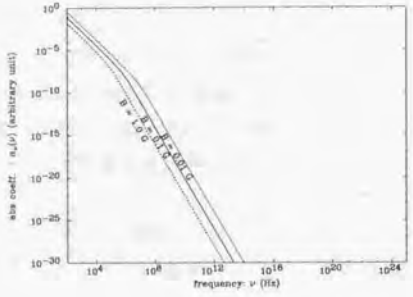

Figure 3.6: Absorption coefficient α_ν of the synchrotron radiation for a power law electron population; $N(\gamma) = N_0\gamma^{-2}$ ($1<\gamma<10^8$).

3.4 Inverse Compton Radiation

In this section, we first consider the very simple case where a soft photon is scattered by a relativistic electron. Next we calculate the inverse Compton spectrum for arbitrary type of electron populations and photon spectra. We employ the formula derived by Jones (1968), which deals with the inverse Compton process more sophisticatedly, including the Klein-Nishina regime.

3.4.1 Scattering From a Single Electron

We start from the scattering event for a single electron and a single photon, which takes place in the Thomson regime. Geometries for inverse Compton scattering is given in Figure 3.7. We denote the electron energy γ, soft photon energy ϵ_0 and scattered photon energy ϵ, and express them in units of $m_e c^2$ (thus they are dimensionless values). We define the parameters with prime in the rest frame of the electron, while the parameters without prime are that in the observer's frame. From the Lorentz transformation and kinematics of Compton scattering, we have

$$\epsilon_0' = \epsilon_0\gamma(1-\beta\cos\theta_0), \tag{3.42}$$

$$\epsilon = \epsilon'\gamma(1+\beta\cos\theta'), \tag{3.43}$$

where θ_0 and θ is the angles between the direction of motions of photons and electrons before/after the scattering, respectively. The scattering is well approximated as being elastic in the rest frame of electrons, such that $\epsilon_0' \simeq \epsilon$. Thus the energies of the photon before scattering, in the rest frame of the electron, and after scattering are in the ratios of

$$\epsilon_0 : \epsilon_0' : \epsilon \simeq 1 : \gamma : \gamma^2, \tag{3.44}$$

which implies a low-energy photon will be scattered up to higher energy by a factor of order γ^2.

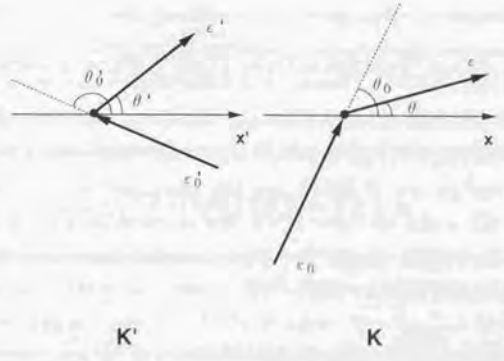

Figure 3.7: Geometries for inverse Compton scattering in the electron rest frame K (left) and the observer's frame K' (right).

Next we derive formulae for the case of an isotropic distributions of photons scattering off an isotropic distributions of electrons. This can be done by averaging equation (3.42) and (3.43) over angles. The total power emitted (scattered) from the electrons is

$$\frac{dE}{dt} = c\sigma_{\rm T}\gamma^2 \int < (1-\beta\cos\theta)^2 > \epsilon_0 n(\epsilon_0) d\epsilon_0 = c\sigma_{\rm T}\gamma^2(1+\frac{1}{3}\beta^2)U_{\rm ph}, \tag{3.45}$$

where $n(\epsilon_0)$ is the number density of photons per energy interval and $U_{\rm ph}$ is the soft photon energy density which is calculated from

$$U_{\rm ph} \equiv m_e c^2 \int \epsilon_0 n(\epsilon_0) d\epsilon_0. \tag{3.46}$$

Thus the net power lost by an electron, subtracting the rate of decrease of the total initial soft photon energy $c\sigma_{\rm T}U_{\rm ph}$, is

$$\dot{\gamma_{\rm IC}} = \frac{4\sigma_{\rm T}\gamma^2 U_{\rm ph}}{3m_e c}. \tag{3.47}$$

By comparing this with equation (3.34), we obtain an well-known relation between the energy loss rate of electrons and energy density of photons/magnetic field as

$$\frac{\dot{\gamma_{\rm sync}}}{\dot{\gamma_{\rm IC}}} = \frac{U_B}{U_{\rm ph}}. \tag{3.48}$$

Note, however, that this relation only holds when the scattering takes place in the Thomson regime, in which $\gamma\epsilon_0 \ll 1$.

3.4.2 Inverse Compton Spectrum

To derive the inverse Compton spectrum for arbitrary distributions of electrons and soft photons, we introduce the formulae derived by Jones (1968). It is accurate in all soft photon energy ranges for both Thomson and Klein-Nishina regimes, as long as the photon and electron distributions are isotropic, and the electrons are ultra-relativistic ($\gamma \gg 1$). The differential photon production rate by inverse Compton scattering $q(\epsilon)$ is

$$q(\epsilon) = \int d\epsilon_0 n(\epsilon_0) \int d\gamma N(\gamma) C(\epsilon, \gamma, \epsilon_0), \tag{3.49}$$

where $n(\epsilon_0)$ is the number density of soft photons per energy interval, and $C(\epsilon, \gamma, \epsilon_0)$ is the Compton kernel of Jones (1968)

$$C(\epsilon, \gamma, \epsilon_0) = \frac{2\pi r_e^2 c}{\gamma^2 \epsilon_0}[2\kappa ln\kappa + (1+2\kappa)(1-\kappa) + \frac{(4\epsilon_0\gamma\kappa)^2}{2(1+4\epsilon_0\gamma\kappa)}(1-\kappa)], \tag{3.50}$$

where

$$\kappa = \frac{\epsilon}{4\epsilon_0\gamma(\gamma-\epsilon)}. \tag{3.51}$$

r_e is the classical electron radius, $r_e \equiv 2.82 \times 10^{-13}$ cm. For a given ϵ_0 and γ, the integration (3.49) can be performed under the range for ϵ

$$\epsilon_0 \le \epsilon \le \gamma\frac{4\epsilon_0\gamma}{1+4\epsilon_0\gamma}, \tag{3.52}$$

from the kinematics of electron-photon scattering.

This production rate $q(\epsilon)$ is converted to emission coefficient $j_\nu^{\rm IC}$ by the relation

$$j_\nu^{\rm IC} = \frac{h\epsilon}{4\pi} q(\epsilon), \tag{3.53}$$

where $h\nu = \epsilon m_e c^2$ and h is the Planck constant.

The energy loss rate per single electron $\dot{\gamma_{\rm IC}}$ in the Klein-Nishina regime is quite uncertain, because electrons do *not* lose their energy continuously, but only by a single encounter with a soft photon. Even in this case, we can estimate the average cooling rate of electrons by considering the energy conservation between electrons and up-scattered photons. From equation (3.49), we find the relation,

$$\dot{\gamma_{\rm IC}} = \int \epsilon d\epsilon \int d\epsilon_0 n(\epsilon_0, t) C(\epsilon, \gamma, \epsilon_0). \tag{3.54}$$

This should coincide with equation (3.47) in the Thomson limit. Figure 3.8 shows the change in the ratio, $\dot{\gamma_{\rm IC}}/\dot{\gamma_{\rm sync}}$, derived from equation (3.34) and (3.54) for various electron Lorentz factors. We assumed the electron population $N(\gamma) \propto \gamma^{-2}$, and changed the $\gamma_{\rm max}$ from 10^4 to 10^6. Note that for $\gamma_{\rm max} \le 10^4$, this ratio is what is expected from the Thomson limit (i.e., equation (3.48)), but $\dot{\gamma_{\rm IC}}$ is strongly suppressed for larger values of $\gamma_{\rm max}$ ($\gamma_{\rm max} \ge 10^5$).

3.5 Particle Escape and Adiabatic Expansion

We assume 'fresh' electrons are injected continuously in the radiating region, while they can escape from this region after the typical time scale $t_{\rm esc}(\gamma)$. After the escape, electrons no longer radiate. Such a situation is also expected if the energy loss by the adiabatic expansion limits the accumulation of relativistic electrons within the photon emitting region. Since the low energy electrons do *not* cool effectively by both synchrotron and inverse Compton losses, the steady state will be achieved by the balance of the escape and the injection rates. For electrons with higher energies ($\gamma \sim \gamma_{\rm max}$), however, the escape is not important because the life time of electrons by radiative cooling may be much shorter than $t_{\rm esc}(\gamma)$. In general, electrons are randomly moving in the emitting region, so that the typical time scale of $t_{\rm esc}$, as well as its energy dependence are completely unknown. Although somewhat arbitrary, there is a good observational reason to believe that escape,

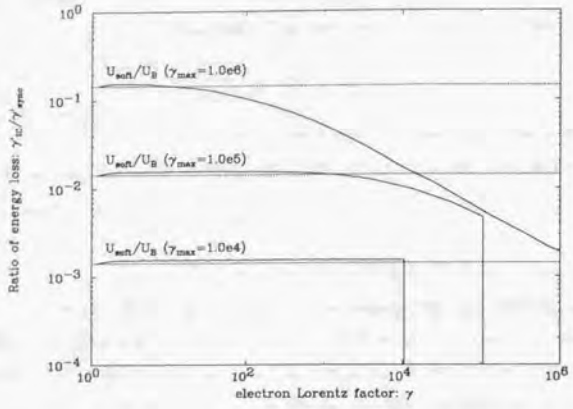

Figure 3.8: Ratio of electron cooling rate by synchrotron/Inverse Compton radiation. We assume $N(\gamma) = N_0\gamma^{-2}$ ($1<\gamma<\gamma_{max}$), where we set the normalization, $N_0 = 10.0$. The source radius is assumed to be $R = 10^{16}$ cm and magnetic field is $B = 0.1$ G, typical values for blazar emission. As γ_{max} increased from 10^4 to 10^6, inverse Compton cooling process becomes inefficient due to the reduction of cross section in the Klein-Nishina regime.

or, equivalently, sudden energy loss by adiabatic expansion, should be important (e.g., § 10.2.6). In this thesis, we will assume the most simple case where t_{esc} has no dependence on energy (a constant value). We see in § 10.6.1 that t_{esc} can be estimated from the turn-over frequency in the multi-wavelength spectra of blazars, where the cooling time and escape time of electrons are expected to be balanced.

3.6 Electron Kinetic Equation

In this section, kinetic equation is introduced to study the characteristic variabilities in the electron/photon spectra of blazars. This approach is well known as a leaky box model of the propagation of high energy cosmic-ray electrons in the inter-stellar medium (e.g., Kardashev 1962).

The time evolution of the high-energy electrons in the magnetic field and the photon field is described by the following kinetic equation:

$$\frac{\partial N_e(\gamma,t)}{\partial t} = \frac{\partial}{\partial\gamma}[g(\gamma,t)N_e(\gamma,t)] + Q(\gamma,t) - \frac{N_e(\gamma,t)}{t_{esc}(\gamma)}, \tag{3.55}$$

where $g(\gamma,t)$ represents the arbitrary types of energy loss and/or gain functions for a single electron. $Q(\gamma,t)$ represents the injection rate of the 'fresh' electrons, and $t_{esc}(\gamma)$ is the escape time of the electrons.

For example, the loss function of synchrotron cooling process is given in equation (3.34),

$$g_{sync}(\gamma) = \gamma_{sync} \propto \gamma^2. \tag{3.56}$$

and the loss function for inverse Compton process is that in equation (3.54)

$$g_{IC}(\gamma,t) = \gamma_{IC}. \tag{3.57}$$

If the scattering takes place in the Thomson regime, the simpler equation (3.47) ($\propto\gamma^2$) would be applied.

The energy gain by the acceleration process is expressed by the acceleration rate $r_{acc}(\gamma)$, which is defined in equation (3.14)

$$g_{acc}(\gamma) = r_{acc}\gamma \propto \gamma^{1-\xi}, \tag{3.58}$$

where ξ is the energy dependence of the diffusion coefficient on energy (see, equation (3.16)).

The general solution of equation (3.55) for arbitrary function $g(\gamma)$ was first given by Makino (1998), yielding

$$N_e = \frac{g(K)}{g(\gamma)}\exp(-\int_0^t \frac{dt'}{t_{esc}(K')})N_{e0}(K) + \int_0^t \frac{g(K')}{g(\gamma)}\exp(-\int_0^{t-t'}\frac{dt''}{t_{esc}(K'')})Q(K',t')dt', \tag{3.59}$$

where

$$y \equiv -\int\frac{d\gamma}{g(\gamma)}, \tag{3.60}$$

$$\gamma = \gamma(y), \tag{3.61}$$

$$K \equiv \gamma(t - \int\frac{d\gamma}{g(\gamma)}), \tag{3.62}$$

$$K' \equiv \gamma(t - t' - \int\frac{d\gamma}{g(\gamma)}), \tag{3.63}$$

$$K'' \equiv \gamma(t - t' - t'' - \int\frac{d\gamma}{g(\gamma)}). \tag{3.64}$$

In general, because of the high non-linearity of the processes involved, the numerical approach is necessary, in particular, when the inverse Compton scattering may occur in the Klein-Nishina regime. We will discuss this more in § 11.

3.7 Relativistic Beaming in Blazar Jets

Assume that there is an emission blob which radiates isotropically in the rest frame K'. In the observer's frame K, the blob is moving with relativistic speed $\beta=v/c$ ($\sim$1), and the radiation is strongly anisotropic. Three important effects are expected as follows.

3.7.1 Aberration of Light

Simple Lorentz transformation shows that the directions of the velocities of light in the two frames (K, K') are related by the formula,

$$\tan\theta = \frac{\sin\theta'}{\Gamma(\cos\theta' + v/c)}, \tag{3.65}$$

$$\cos\theta = \frac{\cos\theta' + v/c}{1 + (v/c)\cos\theta'}, \tag{3.66}$$

where Γ is the Lorentz factor of the blob and given $\Gamma \equiv [1-\beta^2]^{-1/2}$. Considering the spatial case of $\theta' = \pi/2$, we obtain

$$\tan\theta = \frac{c}{\Gamma v} \qquad \sin\theta = \frac{1}{\Gamma} \tag{3.67}$$

This means that in the frame K, half of the photons are concentrated in a narrow cone of half angle $\theta\sim1/\Gamma$.

3.7.2 Time Dilation

The emission and arrival time intervals are different. The difference of arrival time Δt_a is expressed by the difference of the emission time Δt_e as

$$\Delta t_a = \Delta t_e(1 - \beta\cos\theta), \tag{3.68}$$

while $\Delta t'_e$ is related with Δt_e

$$\Delta t_e = \Gamma \Delta t'_e. \tag{3.69}$$

leading to

$$\Delta t_a = \Gamma(1 - \beta\cos\theta)\Delta t'_e \equiv \Delta t'_e/\delta. \tag{3.70}$$

This is a convenient derivation of the *beaming factor* δ ($= [\Gamma(1-\beta\cos\theta)]^{-1}$). As we see in Figure 3.9, the beaming factor exceeds unity if viewing angles are small. Note that, when the observer is located perpendicular to the moving direction (i.e., $\theta' = \pi/2$) in the source frame, $\delta \simeq \Gamma$ because $\sin\theta \simeq 1/\Gamma$.

3.7.3 Blue Shift of Frequencies and the Luminosity Enhancement

Since frequencies are the inverse of times, we have a simple relation,

$$\nu = \delta\nu'. \tag{3.71}$$

The specific intensity $I(\nu)$ divided by the cube of the frequency is Lorentz invariant (e.g., Rybicki & Lightman 1979). Thus we have

$$I(\nu) = \delta^3 I'(\nu') = \delta^3 I'(\nu/\delta). \tag{3.72}$$

Integration of $I(\nu)$ over the frequencies yields

$$I \equiv \int I(\nu)d\nu = \delta^4 \int I'(\nu')d\nu' = \delta^4 I', \tag{3.73}$$

Assuming isotropy of the emission, the corresponding transformation for luminosity is

$$L_{\rm obs} = \delta^4 L'_{\rm src}. \tag{3.74}$$

Because of this factor δ^4, blazars, whose jet emissions are pointing closely to the observer, are strongly enhanced in brightness.

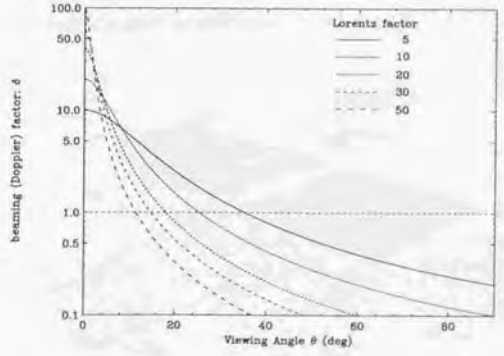

Figure 3.9: Beaming (Doppler) boosting factor δ as a function of viewing angle θ. Results for Lorentz factor, Γ = 5, 10, 20, 30 and 50 are shown respectively. Note that $\delta = 2\Gamma$ for $\theta = 0$, and $\delta = \Gamma$ for $\theta = 1/\Gamma$.

Chapter 4

Instruments on-board *ASCA*

4.1 *ASCA* Satellite

ASCA (Advanced Satellite for Cosmology and Astrophysics) satellite (Tanaka et al. 1994) is the fifteenth scientific satellite of Institute of Space and Astronautical Science (ISAS). *ASCA* is the fourth Japanese X-ray observatory succeeding *HAKUCHOU*, *TEMMA*, and *GINGA* satellites. It was launched by the M-3SII rocket on February 20, 1993 (JST) from Kagoshima Space Center (KSC) in Kagoshima, Japan. *ASCA* orbits on a nearly circular orbit with its height about 520 km at its perigee and about 620 km at its apogee. It weighs about 420 kg and the length of an extensible optical bench (EOB) is about 4.7 m. Figure 4.1 shows a schematic view of *ASCA* satellite in orbit.

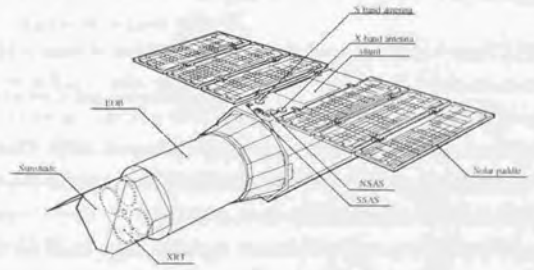

Figure 4.1: Schematic drawing of *ASCA* satellite.

ASCA features imaging and spectroscopic capabilities with a large effective area and the highest energy resolution ever achieved in a wide energy band, which ranges from

0.5 keV to 10 keV. It carries four X-ray telescope (XRT), equipped with two X-ray CCD cameras (Solid state Imaging Spectrometer; SIS) and two gas scintillation imaging proportional counters (Gas Imaging Spectrometer; GIS) at their focal plane. The arrangement of these instruments is shown in Figure 4.2. These two types of detectors have complementary properties; the SIS has finer position and better energy resolution than GIS, while the GIS has faster time resolution and wider dynamic range in source intensity. We briefly describe the XRT, SIS, and GIS in the following sections.

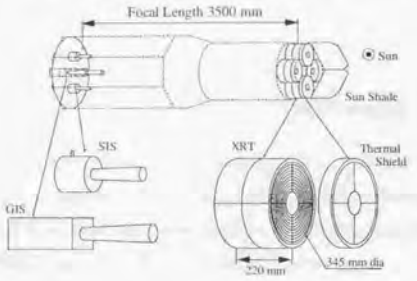

Figure 4.2: Arrangement of instruments on *ASCA* satellite.

4.2 XRT

The *ASCA* XRT(X-ray telescope) consists of a large number of conical thin-foil reflectors to fill its aperture nested with their surface seen almost edge-on (Figure 4.2). It aims to achieve a large effective area and high throughput over a broad energy band up to 10 keV. Four XRT's on-board *ASCA* satellite are placed at the top of EOB. They were produced cooperatively by Nagoya University, NASA Goddard Space Flight Center (NASA/GSFC), and Institute of Space and Astronautical Science (ISAS).

X-rays from celestial sources are reflected by XRT only when its incident angle is smaller than the critical angle of 1°. To achieve a large effective area, over a hundred nested thin foils are used for *ASCA* XRT. Since it is difficult to shape a thin foil into a paraboloid and a hyperboloid, a conical surface is used as an approximation. Although this approximation reduces the image quality, the roughness of the reflectors' surface mainly contributes to the point spread function, whose half power diameter of 3 arc-minutes. Design parameters and performance of XRT are shown in Table 4.1.

Table 4.1: Design parameters and performance of *ASCA* XRT

Mirror substrate	127μm
Mirror surface	Acrylic lacquer 10μm + Au (500 oA)
Mirror length	100mm
Number of mirrors	120 foils
Inner (outer) diameter	120 (345) mm
Focal length	3500 mm
Incident angle	$0.24^\circ \sim 0.7^\circ$
Total weight[a]	$\sim$ 40 kg
Geometrical area	558 cm^2/telescope
Field of view	24 arcmin. (FWHM @ 1 keV)
	16 arcmin. (FWHM @ 1 keV)
Energy range	$\leq$ 10 keV
Effective area[a] (4 XRTs)	$\sim$ 1300cm^2 (1 keV)
	$\sim$ 600cm^2 (7 keV)
Half power diameter	$\sim$ 3 arcmin.

4.3 SIS

The *ASCA* SIS is an X-ray sensitive CCD camera, and features high energy resolution and fine positional resolution. The details of the design and In-orbit performance is given in Burke et al. (1991) and Yamashita et al. (1997). Two SIS detectors (hereafter SIS0 and SIS1) are placed in the focal planes of two of the four XRT's. They were developed by the Massachusetts Institute of Technology (MIT), Osaka University, and Institute of Space and Astronautical Science (ISAS).

4.3.1 System Description

The SIS consists of four X-ray CCDs (Charge Coupled Device), analog electronics (SIS-AE), and digital electronics (SIS-DE). As shown in Figure 4.3, the four CCD chips are aligned in a square with narrow gaps. Each CCD chip has 422 × 420 pixels. The dimensions of the CCD chip are 11mm × 11mm which covers 11' × 11' in the sky. Design parameters and performance of SIS are summarized in Table 4.2.

The SIS is a frame transfer type CCD, whose detection part is made of an Si p-n junctions. An insulator layer made of SiO_2 is attached on the front surface of the n-type Si. The electrodes are built on both the front and the back of the device. By supplying specific patterns of voltages on the electrodes, charges in a pixel are transfered from one pixel to the next. A depletion layer is developed in the device by supplying a bias voltage

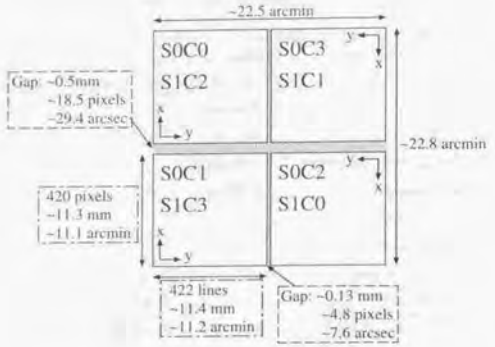

Figure 4.3: Alignment of the four CCD chips in SIS.

Table 4.2: Design parameters and performance of *ASCA* SIS

Irradiation Method	Front irradiation
Charge Transfer Method	Frame Transfer
Clock	3-phase drive
Number of pixels in Image Region	420 pixels × 422 lines per chip
Pixel Size	27 μm
Area	11×11 mm^2 per chip
Field of View	11×11 square arc minutes per chip
Thickness of Depletion Layer	$\sim 40\mu$m
Drive temperature	~ -62°C
Energy Band	0.4-12 keV
Quantum Efficiency	80% at 6 keV
Energy Resolution	2% at 5.9 keV (FWHM)

between the electrodes on the front and on the back. The CCD chips are cooled down to −62°C with a thermo-electric cooler (TEC) from the back to reduce the thermal noise.

Two SIS-AE's are on-board corresponding to SIS0 and SIS1 respectively. Electric signals from SIS are fed into SIS-AE and their pulse heights are converted into digital signals with analog-to-digital converters (ADC). SIS-AE also generates driving clocks for the CCD chips and monitors and controls the temperature of the CCD chips. SIS-DE picks up X-ray events in the digital signals from SIS-AE with two digital signal processors (DSP) and sends them to a data processor (DP).

4.3.2 On-Board Data Processing

The observation modes are designed for scientific observations and consists of *faint* mode, *bright* mode, and *fast* mode. In the observation modes, the data are processed every four seconds independent of the bit rate (High/Medium/Low). The order of reading of the CCD chips can be changed in accordance with the aim of observation (CCD mode). Three CCD modes are designed for standard observations: 1-CCD mode, 2-CCD mode, and 4-CCD mode. The number preceding "CCD" in mode name is the number of chips to be read out.

In *faint* mode and *bright* mode X-ray images and spectra are simultaneously obtained with poor time resolution of 4 sec at most. Information on detected X-rays is acquired almost in the same way in both modes, except that the information is compressed in *bright* mode. 1-, 2-, and 4-CCD modes are available in faint and *bright* modes.

In the *bright mode* DP classifies an event by assigning a "grade". The grade ranges from 0 to 7 depending on the pattern of the pixel levels of neighboring pixels whose pixel levels exceed a split threshold. Definitions of grades are shown in Figure 4.4. DP also sums pixel levels which exceed the split threshold and are not of detached corner pixels, and compresses the summed pixel level with 12 bits length into 11 bit data.

In Table 4.3 operation mode of SIS are summarized. Most of the observations in this thesis were performed in normal 1-CCD *faint* mode for bit-High and normal 1-CCD *bright* mode for bit-Medium (§ 6.1). The telemetry limit is 64 cts/s/SIS for the former, while 32 cts/s/SIS for the latter. During the observation of Mrk 421 in 1998, SIS count rate exceeds this telemetry limit thus we perform careful data reduction to eliminate the effect of telemetry saturation (see, § 7.1.1).

Table 4.3: Summary of observation modes in SIS

	Faint	Bright	Fast
Time Resolution	4/8/16 sec	4/8/16 sec	16 ms
	(1/2/4CCD mode)		(1CCD mode)
Event Trans. Rate	128/16/4	512/64/16	1024/128/32
(cts/sec/2 sensors)	(High/Medium/Low bit rate)		
Data size per event	128 bits	32 bits	16 bits
CCD ID	2 bits	—	—
Pixel level	12 bits ×9	11 bits	11 bits
Event position	9 bits ×2	9 bits ×2	1 bit
Time stamp	—		3 bits
Grade	—	3 bits	1 bits

Figure 4.4: Definitions of grades of events.

4.3.3 Reduction of the SIS data

Hot and Flickering Pixels

A pixel creating events but *no* incident particle is called a "hot pixel" or a "flickering pixel". These erroneous pixels are mainly due to a large dark current, caused by lattice defects on the insulator layer under electrodes of the CCD. Assuming the Poisson distribution, we regarded a pixel, whose number of events largely exceeds the average among surrounding pixels, as a flickering pixel. In a standard analysis the average is calculated from 5×5 pixels centering a pixel of interest. The threshold probability is set to $10^{-5.25}$, which corresponds to a probability that one out of all the pixels in a chip (422×420 pixels in total) exceeds the threshold by chance, namely, $1/(420 \times 422)$.

Echo

A pixel level suffers an artificial increase by an "echo" phenomenon, which originates from a transitional property of SIS-AE. In SIS-AE an analog signal from the CCD leaves an extra signal after the main signal as a result of a "ringing" effect. A significant pulse height remains even at a time when the signal from a next pixel is processed.

In the analysis, the *faint* mode data can be corrected to remove the echo phenomenon by subtracting pixel levels of the center pixel from that of right-hand pixels by the echo fraction for an observation period. In *bright* mode data, however, only summed pixel levels are obtained so that no correction to the data can be performed. In this case one should use a better subtraction technique of the echo phenomenon thorough calculating the response matrix.

Dark Frame Error (DFE)

A dark frame error (hereafter DFE) is a residual dark level causing pixel levels to be shifted by a constant amount, depending on the SIS condition during the observation. The DFE arises from incomplete estimation of dark levels in calculating pixel levels in SIS-DE. The dark level is calculated as an average of raw PH data which distributes asymmetrically around the true dark level.

The DFE is mainly due to light input in an optical band. The distribution of pixel levels at corner pixels are accumulated for each short time interval, each 64 sec usually, and compared with a template by cross-correlating them. This estimation is repeated throughout an observation period, and the time history of DFE values are obtained. For *faint* mode data the estimated DFE are subtracted from pixel levels of all the pixels sent to the ground. Since no DFE correction can be made for *bright* and *fast* mode data,

the effect of DFE on a spectral analysis are eliminated by using an appropriate response matrix.

Charge Transfer Inefficiency (CTI)

Charge transfer inefficiency (CTI) is defined as the probability that an electron in a charge cloud is not transfered from one pixel to the next. The CTI is caused by charge traps by lattice defects in channels of electrons in the CCD chips. Since such lattice defects are created by charged particles in orbit, CTI increases gradually.

CTI can be corrected, except for *fast* mode data. The method of the correction is straightforward reading a CTI table to obtain CTI at an observation period, calculating a reduction factor of energy scale for each event by multiplying CTI by the number of transfers of electrons of the event, and dividing the pixel level of the event by the reduction factor.

4.4 GIS

ASCA GIS is a gas scintillation imaging proportional counter. It features high time resolution and high detection efficiency for hard X-ray photons. The detail description on the detector design and pre-flight calibrations are given in Ohashi et al. (1996). Two GISs (hereafter GIS2 and GIS3) are on-board the *ASCA* satellite and placed on focal planes of another two of the four XRT's. They were produced by University of Tokyo and Institute of Space and Astronautical Science (ISAS).

4.4.1 System Description

GIS consists of a gas cell, a position sensitive photo-multiplier (Imaging Photo-Multiplier Tube; IPMT), a high voltage unit, a housing, and electronics (GIS-E).

The gas cell has a cylindrical shape with $\sim$ 60mm diameter and $\sim$ 25mm height. A schematic view of the cross section of a gas cell and a position sensitive photo-multiplier tube of GIS are shown in Figure 4.5. The field of view of GIS is circular with 50' diameter in the sky. Xe gas (96%) and He gas (4%) are filled in the gas cell. In front of the gas cell, a plasma shield is placed to protect GIS from radiation damage. The gas cell is divided into two regions: a drift region and a scintillation region. IPMT is attached below the gas cell as shown in Figure 4.5. These cells are optically connected with each other through a quartz window at the bottom of the gas cell and a bialkali photo-electrode at the top of IPMT. Design parameters and performance of GIS are summarized in Table 4.4.

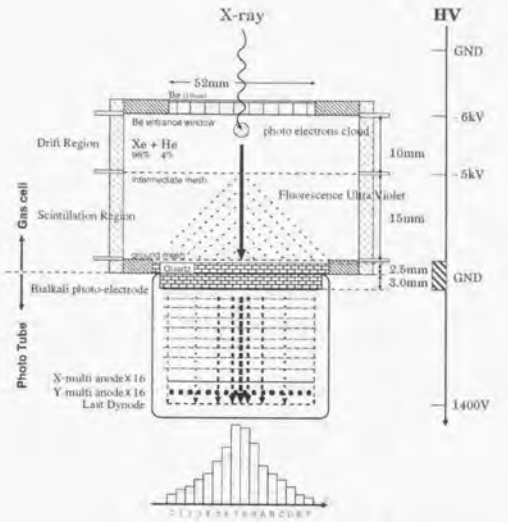

Figure 4.5: Cross sectional view of a gas cell and a position sensitive photo-multiplier tube of GIS. The voltage of each part of the detector supplied by a high voltage unit is shown at the right of the figure for reference. A schematic drawing of an X-ray detection is also shown.

Table 4.4: Design parameters and performance of GIS

Energy Band	0.7-15 keV
Energy Resolution	8% at 5.9 keV (FWHM)
Effective Area	50 mm diameter
Positional Resolution	0.5 mm (FWHM)
Time Resolution	$\sim$ 61 μsec (Minimum in PH mode)
	1.95 ms (Minimum in MPC mode)

The high voltage unit supplies appropriate voltages to the gas cell and IPMT as shown at the right in Figure 4.5. A bleeder is placed below IPMT and supplies voltages to a dynode and to the anodes of IPMT by dividing a high voltage from the high voltage unit. At the end of GIS2, a radiation belt monitor (RBM) is attached to monitor the flux of charged particles.

One GIS-E is on-board the satellite and processes signals from GIS2 and GIS3. GIS-E converts analog signals from two GIS's into digital signals with two 12 bits ADC and

four 8 bits flash ADC. The CPU in GIS-E collects and edits this information and sends it through a FIFO (First-In First-Out logic) to the DP of the satellite, which commonly edits SIS data and GIS data into a telemetry format. GIS-E also supplies power to two GIS's and RBM, controls the high voltage unit and the preamplifier to operate GIS, and handles the RBM flag to prevent the detectors from radiation damage.

4.4.2 On-Board Data Processing

The observation modes are designed for scientific observations and consists of *PH* normal mode (*PH* mode in short), *PH PCAL* mode (*PCAL* mode in short), and *MPC* mode. In the *PH* mode, X-ray images and spectra are both obtained with high time resolution up to 61μs.

Arrival times of X-rays are measured with scalers, which count the system clock of the satellite. The frequency of the system clock depends on the bit rate: it is 16384 Hz for high bit rate, 2048 Hz for medium bit rate, and 512 Hz for low bit rate. Table 4.5 shows the clock speed relating to time assignment of GIS(2+3) with maximum counting rates observable with GIS. We find that for the high bit rate, telemetry limit is 128 cts/s/GIS while 16 cts/s/GIS for the medium bit rate. For Mrk 421 observation in 1998, the source was very bright and the telemetry was strongly saturated when the data was taken at medium bit-rate (§ 7.1.1). For the data taken at bit-High rate, dead-time of the detector is about 3 % for a bright source of 30 cts/s/GIS (Makishima et al. 1996).

Table 4.5: Clock speed relating to time assignment of GISs

	Time stamp		Telemetry output		Maximum
Bit Rate	Frequency	Period	Frequency	Period	Counting Rate
High	16384 Hz	$\sim$ 61 μs	256 Hz	$\sim$ 4 ms	256 c/s
Med	2048 Hz	$\sim$ 488 μs	32 Hz	31.25 ms	32 c/s
Low	512 Hz	$\sim$ 1.95 ms	4 Hz	125 ms	8 c/s

4.4.3 Reduction of the GIS data

Gain Correction

The gain of GIS mainly depends on the temperature of the gas cell and the position at which an X-ray is detected. The temperature dependence is due to characteristics of Xe gas in the gas cell. The positional dependence is caused by the positional dependence of the sensitivity of IPMT. On the surfaces of both GIS2 and GIS3, radioactive isotopes

^{55}Fe are mounted near the rim of their apertures. ^{55}Fe emits fluorescent X-rays of energy 5.895 keV. This X-ray line is used to measure the instantaneous gain number of GIS. The imaging capability of GIS enables us to extract only events from the isotopes and events from the isotopes do not contaminate X-rays from celestial sources.

The gain correction for GIS events is divided into two steps. First, a pulse height of an event is corrected taking the gain map into account. After this correction the corrected gain number should be constant over the surface of the detector. Second, the resultant pulse height is further corrected so that the X-rays from ^{55}Fe has a constant value. This cancels the temperature dependence of the gain number and the corrected pulse height is independent of the observation conditions, called a pulse height invariant (PI). According to pre-flight and in-flight calibrations, the uncertainty in the GIS gain is known to be 1%.

Background Rejection

Over 90% of background events can be rejected by means of evaluating a pulse height, a rise time, and the spread of the event. Sources of GIS background events are divided into two types.(a) X-rays absorbed at abnormal positions in the gas cell and (b) charged particles or high energy γ-rays. Only events with rise times between 159 and 218 (rise time window) are collected in the on-board data processing and are sent to the ground station. 92% of background events are rejected by filtering events with a narrower rise time window in the data analyses. Different rise time windows are set for events with different pulse heights. A table of rise time windows for various pulse heights is called an "RT mask". The spread discrimination rejects 60% of background events not rejected by the rise time discrimination. Only events in a certain range of spread patterns are collected in the on-board data processing and are sent to the ground station.

4.5 Alignment of the Detectors

The optical axes of the four XRT's point to slightly different positions on the sky. Also, the centers of the two SIS's and two GIS's correspond to different positions on the sky. This gives different effective areas to different detectors. The relations between these positions are measured by the *ASCA* calibration team and are used to evaluate the detector's response in analyses. The alignment of each detector is shown in Figure 4.6. The positions of the optical axes and detector centers in reference to the center of SIS0 are projected on the focal plane in the figure. The figure also shows "nominal positions" for various observation modes, where an image of the target of an observation is planned to be placed. In 1-CCD mode, for example, the satellite's attitude is controlled so that an image of the

target centers on the 1-CCD nominal position on the detectors.

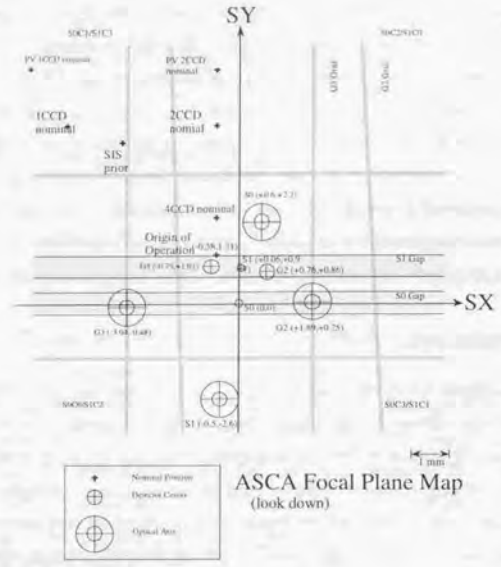

Figure 4.6: Alignment of the detectors. The optical axes and detector centers of SIS0, SIS1, GIS2, and GIS3 are shown. Nominal positions for various observation modes are also plotted in the figure.

Chapter 5

Instruments on-board *RXTE*

Since our main goal is to understand variability and spectral behaviour of all TeV blazars, we need X-ray data taken at various states of source activity. For this purpose, we conducted several *RXTE* (Rossi X-ray Timing Explorer) observations as a guest observer. We also analyzed the archival data taken from 1996 April to 1998 January, to have more complete sample. We mainly analyze PCA data in 2.5−20 keV range where the detector is well calibrated and the best noise-to-signal ratio is obtained.

5.1 *RXTE* Satellite

RXTE is a X-ray mission which was launched on December 30, 1995. The spacecraft was designed and built by the Goddard Space Flight Center (GSFC). It was launched by a Delta II rocket that put *RXTE* into a low-earth circular orbit whose apogee and perigee are 580 and 560 km, corresponding to an orbital period of about 90 minutes, at an inclination of 23 degrees.

RXTE carries two pointed instruments, the Proportional Counter Array (PCA) developed by GSFC and the High Energy X-ray Timing Experiment (HEXTE) developed by University of California at San Diego (UCSD). PCA covers the lower part of the energy range (2 − 60 keV), while the HEXTE covers a higher energy range, from 20 keV to more than 100 keV. These instruments are equipped with collimators yielding an angular resolution of 1 degree. In addition, *RXTE* carries an All-Sky monitor (ASM) from Massachusetts Institute of Technology (MIT), that scans about 80 % of the sky on every orbit. ASM allows constant monitoring of the sky at time scales of 90 minutes or longer. Figure 5.1 shows a schematic view of *RXTE* satellite in orbit.

RXTE is designed to facilitate the study of time variability in the emission of celestial X-ray sources with moderate spectral resolution. Time scales from microseconds to

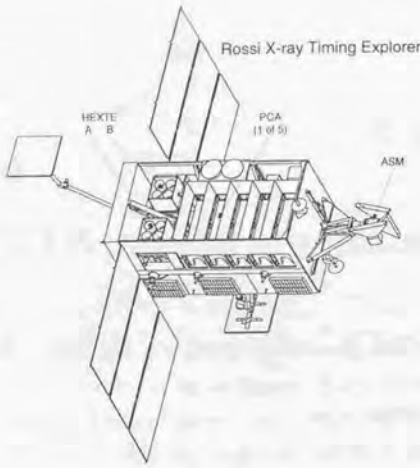

Figure 5.1: Schematic drawing of *RXTE* satellite. Three kinds of instruments, PCA, HEXTE and ASM are carried on the spacecraft.

months are covered in an instantaneous spectral range from 2 to 100 keV. It is designed for a required lifetime of two years, with a goal of five years.

5.2 PCA

5.2.1 System Description

The *RXTE* PCA (Proportional Counter Array) consists of five large proportional counters (PCUs) with anti-coincidence (hereafter "veto") features which provide a very low background. A mechanical hexagonal collimator is carried on each proportional counter, which provides an angular resolution of 1 degree (FWHM). Because of the large effective area, sources as faint as 1 mCrab can be detected only in a few seconds. The detailed description on the PCA design, as well as the orbit performances are given in Jahoda et al. (1996; 1999).

The total area of 5 PCUs is 6250 cm^2. The schematic view of an assembly of five units and each proportional counter are given in Figure 5.2. We summarize the design parameters and performance of PCA in Table 5.1. The PCA is effective over the energy

range $2 - 60$ keV with 18 % energy resolution at 6 keV. PCA units are filled with Xe gas and achieve low background through efficient veto schemes including side and rear chambers and a propane top layer.

The 1 degree FOV (FWHM) of the tubular (hexagonal) collimations yields a source confusion limit at ~ 0.1 mCrab. The Crab nebula will yield 8700 cts/s ($2 - 10$ keV) and 1200 cts/s (10 - 30 keV) in the PCA. The background in these two bands are 20 and 24 cts/s, respectively. With these backgrounds, an AGN source of intensity 1.3 mCrab and energy index 0.7 will be detected at $\geq 2\ \sigma$ in only 1 sec at $2 - 10$ keV and at $3\ \sigma$ in 10 sec at $10 - 30$ keV. Monitored veto rates will provide a measure of the background to at least 10 % of its value.

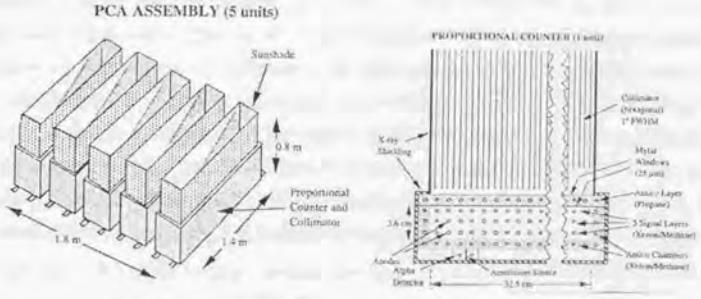

Figure 5.2: *left* : Assembly of 5 PCA counters with total area of 6250 cm^2. *right* : Schematic view of one PCA unit.

Table 5.1: Design parameters and performance of *RXTE* PCA

Energy Band	$2 - 60$ keV
Energy Resolution	$\leq 18\%$ at 6 keV (FWHM)
Time Resolution	1 μ sec
Angular Resolution	1 degree (FWHM)
Detectors	5 proportional counters
Collecting Area	6500 cm^2
Net Area	3000 cm^2 (at 3 keV) and 6000 cm^2 (at 10 keV)
Layers	1 Propane veto, 3 Xe, 1 Xe veto layer
Sensitivity	0.1 mCrab ($2 - 10$ keV in minutes)
Background	2 mCrab
Telemetry	18 kb/s

5.2.2 On-Board Data Processing

The system will process count rates from the PCA up to 5×10^5 cts/s (only 6 % deadtime for the Crab) and will be able to determine photon arrival time with an accuracy of ~ 1 μsec. The PCA data stream can be binned and telemetered in 6 different modes simultaneously by 6 independent Event Analyzers (EA) which operate in parallel, each analyzing the total PCA data stream. Two other EAs will process the ASM data and control its rotation.

Two of the 6 PCA EAs are intended to be reserved for two standard PCA modes with timing and spectral parameters that will remain unchanged throughout the mission to provide a uniform mission data bank. For the remaining 4 PCA EAs, however, processing modes are flexibly selected by guest observers to accommodate the scientific requirements. The standard modes consists of *Standard*-1 and *Standard*-2. *Standard*-1 contains 8 rates sampled at 0.125 sec: the total good event rate from each individual counter, propane event rates summed over the PCA, and the rate of oll other events. *Standard*-1 also contains calibration spectra which are stored and telemeterd separately for each detector and each layer once every 128 seconds. *Standard*-2 contains 129 channel pulse height spectra for each signal layer of each detector, 33 channel propane layer spectra for each detector, and 29 rates of various combinations of combinations of coincidences for each detector read out every 16 seconds.

5.2.3 Reduction of PCA data

Energy Response

As we have seen in Figure 5.2, each PCU detector, from the top, consists of a thermal shield, a collimator, an aluminized mylar window, a propane volumes, and a detector body. The low energy threshold of the PCA is determined by the transmission of the mylar windows (1 mm each) and the propane volume. For generating the response matrix, the important quantity is the photo-electric stopping power of each layer and all exterior layers.

The gain of the counter is monitored continuously with an ^{241}Am radioactive source for which detection of the α particle identifies the calibration X-rays. Additional information about the energy scale has been obtained from measurements of the iron line in the super nova remnant Cassiopeia A, and the Xe-L escape peak which is collected in a special mode that keeps all events with a calibration flag.

PCA response matrices map 900 energies from 0.023 to 100 keV to 256 PHA channels. Half of the energy channels are equally spaced below 10 keV, except that the three channels

which include one of the Xe-L edges are split into two channels with channel boundary matching the atomic edge. The remaining channels are also equally divided except that the channel including the Xe-K edge is again split into two channels.

Background

The detector background mainly consists of two components – the diffuse sky background which enters through the collimator as X-rays, and the internal background which arises from interactions between radiation or particles in orbital environment with the detector or spacecraft. Since PCA does *not* produce continuous measurements of the background, it relies on a model background.

Figure 5.3 shows the total background summed over all 5 PCU detectors during the observation of Mrk 501 in 1998 May (§ 8). The upper line includes photon counts from the source, for comparison. Line features are present due to Xe-L escape photons, copper fluorescence (primarily from the backplane, and concentrated in the third layer), unflagged calibration events, and a contribution which appears to come from residual activity in the collimator. The background typically varies between 18–24 cts/s/PCU. In practice, the most significant contributions to the background are dependent on the local particle environment of the satellite and the recent history of passage through SAA : the presence of background components after passage through the SAA indicates that some of the detector or spacecraft becomes activated.

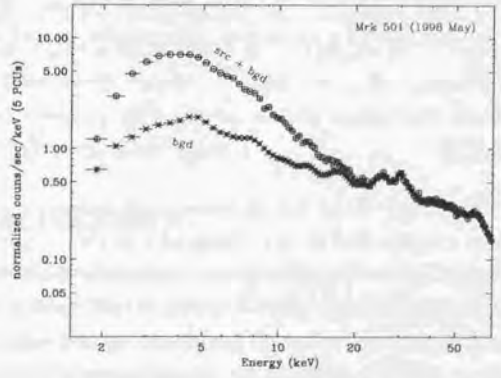

Figure 5.3: The PCA background versus source photon counts from Mrk 501 (from 1998 May observation). The count rate of 5 PCUs are summed.

To model the background, it is assumed that the internal background varies on a time scale which is long compared to the natural time-scale of the PCA *Standard*-2 data (16 sec). The design is such that the model can be evaluated once every 16 seconds, and that the equivalent of a *Standard*-2 data file can be created with separate information for each detector and each anode chain.

The modeled background spectrum can be based on parameters measured at the time of the observation, parameters describing the condition and position of the spacecraft, and parameters describing the evolution of the spacecraft. PCA background models based on these parameters have been constructed in two ways: using data from blank-sky observations and using data from periods of Earth occultation. The models based on the local particle parameters are constructed using data from only those spacecraft orbits in which the SAA-induced activation is small. Some of these data are still significantly contaminated by SAA-induced activation but this contamination can be later removed by an appropriately constructed model of the activation component of the background.

Electron Contamination

The background models are parameterized in terms of particle rate. In addition to the high energy protons and ions, low energy electrons may also lose their energy within the detector. Electrons with several 10s of keV may come through the collimator and stop in the first Xe layer. The rate of propane plus first layer coincidences measures such a population, and while these events are vetoed, the rate can be used to screen periods when there could be increased background, for instance due to the same electrons fluorescing the collimator. For the reliable data reduction, we screen the data when the electron rate is significantly high.

5.3 HEXTE

The HEXTE (High Energy X-ray Timing Experiment) features a large area and low background with a 1 degree field of view coaligned with the PCA field of view. Eight "Phoswich(NaI+CsI)" detectors are arranged in two clusters, each of which rocks on and off the source. This and automatic gain control for each of the eight detectors together yield a well determined background which permits the spectral measurements of a faint source (1 mCrab) at 100 keV in about 1 day. We summarize the design parameters and performance of HEXTE in Table 5.2.

In this thesis, however, we do not use HEXTE data for several reasons. Firstly, a lot of calibration problems still remain and make the analysis results quite uncertain. Secondly, the typical exposure for *RXTE* observation ($\sim$ 1 ksec) was too short to yield the hard X-ray spectrum at > 20 keV. Thirdly, X-ray spectra of TeV blazars evolve significantly during the observation. Hence we cannot sum over the photons obtained in different epochs. To see this more clearly, one example of the HEXTE spectrum derived from 60 ksec integration of data is given in Figure F.1.

Table 5.2: Design parameters and performance of *RXTE* HEXTE

Energy Band	20 - 200 keV
Energy Resolution	$\leq$ 18% at 60 keV (FWHM)
Time Resolution	10 μ sec
Angular Resolution	1 degree (FWHM)
Detectors	2 clusters of NaI(Tl) and CsI(Na) phoswich units (4)
Collecting Area	1600 cm^2
Net Area	1200 cm^2 (at 50 keV) and 300 cm^2 (at 200 keV)
Sensitivity	1 mCrab (90-110 keV; 3 σ for 10^5 sec pointing)
Background	100 mCrab
Telemetry	5 kb/s

5.4 ASM

The ASM (All Sky Monitor) is the watchdog that alerts XTE to flares and changes of state in X-ray sources. It consists of three rotating Scanning Shadow Cameras (SSC) that can scan about 80 % of the sky in 90 minutes. The camera is sensitive to 2 — 10 keV X-rays and have three energy channels. The cameras provide measurements of intensities of about 75 known celestial sources in a day and can measure the position of a previously unknown source with a precision of about 3'.

5.4.1 System Description

The ASM consists of three Scanning Shadow Cameras (SSC) on one rotating boom with a total net effective area of 90 cm^2 (180 cm^2 without masks). Figure 5.4 shows schematic view of the assembly of shadow cameras and their scan directions. The design parameters and performance of ASM are summarized in Table 5.3.

Each SSC is a one-dimensional "Dicke camera" consisting of a 1-dimensional mask and a 1-dimensional position-sensitive proportional counter (Figure 5.4). Because of the mask ('slit') above the proportional counter, the X-rays coming from different directions

should make different images on anodes, which is the principle of the Shadow Camera. The gross field of view of a single SSC is $6° \times 90°$ FWHM, and the angular resolution in the narrow (imaging) direction is 0.2 degree.

A motorized drive will rotate the three SSCs from field to field in 6° steps. At each resting position, a ~ 100 sec exposure of the X-ray sky will be made; a complete rotation is thus completed in 90 minutes. Since the 'crossed-field detectors' are stepped by only the 6° FWHM angle, each source is viewed twice. In this manner, each source gives rise to the entire mask pattern in the accumulated data, thus minimizing aliasing and side bands in the deconvolved results. During each rotation, ~ 80 % of the sky will be surveyed to a depth of ~ 20 mCrab (about 50 sources). Frequent spacecraft maneuvers will make it likely that 100 % of the sky is surveyed each day. In one day, the limiting sensitivity becomes ≤ 10 mCrab (~ 75 sources).

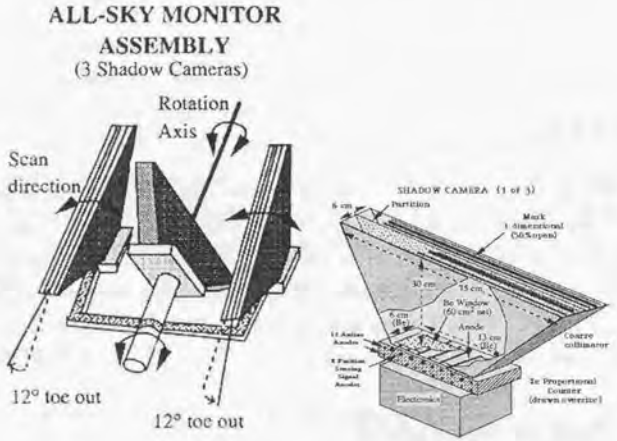

Figure 5.4: *left* : All-Sky Monitor assembly of 3 Shadow Cameras. ASM scans 80 % of the sky every 90 minutes to monitor the intensity of the brightest 75 X-ray sources and to provide an alert if a source changes state or brightness suddenly. This allows the spacecraft to be maneuvered to observe with more powerful PCA/HEXTE systems. *right* : Shadow Camera (1 of 3) of All Sky Monitor. Each SSC is a sealed proportional counter filled to 1.2 atm with Xe-CO_2, and sensitive depth of 13 mm.

Table 5.3: Design parameters and performance of *RXTE* ASM

Energy Band	2 – 10 keV
Energy Resolution	~20% in 2 – 10 keV (3 energy channels)
Scan Time	90 min: 80 % of the sky per orbit
Angular Resolution	0.2 degree
Positional Resolution	3' × 15'
Detectors	3 Scanning Shadow Cameras
Collecting Area	180 cm^2 (without masks)
Net Area	90 cm^2 (3 detectors)
Sensitivity	20 mCrab in 90min; $\leq$ 10 mCrab in a day
Telemetry	3 kb/s

5.4.2 Reduction of ASM data

The position histograms are analyzed in near-real time in the Science Operations Facility at GSFC. The data is first fit with the model responses of each SSC to the catalogued bright X-ray sources within the field of view. A linear least squares calculation yields the strengths of each of these sources. Next, the fit residuals are examined via a cross-correlation technique for evidence of previously unknown or unexpectedly bright sources. When a new source is found, its coordinates are entered into the source catalogue. For quick-look analysis, the data will be performed on a dwell-by-dwell and SSC-by-SSC basis. For the definitive analysis, the analysis will be performed simultaneously on data from neighboring dwells and from multiple cameras. The resultant ASM light curves are open to public and one can obtain the data via online service for 75 sources (http://space.mit.edu/XTE/asmlc/ASM.html).

Chapter 6

Observation

6.1 X-ray Observations with *ASCA*

We analyzed data from 37 *ASCA* observations of four TeV blazars as listed in Table 6.1. The total net exposure amounts to 540 ksec for Mrk 421, 100 ksec for Mrk 501, 210 ksec for PKS 2155−304, and 60 ksec for 1ES 2344+514. The observational log for *ASCA* observations are shown in Table 6.2−6.5. Observation epoch of four TeV blazars are schematically shown in Figure 6.1.

The data we analyzed in this thesis consists of the data taken according to our proposal, and the data taken during the Performance Verification (PV) phase. For all observations, the SIS was operated in the *faint* mode for bit-High and *bright* mode for bit-Medium (see also § 4). In all observations, except for those taken in the PV phase, source positions were placed in the nominal position of 1-CCD mode at chip 1 and chip 3 of SIS0 and SIS1, respectively (Figure 4.6). The GIS was operated in *PH* mode with standard bit assignment for all observations. For the observations in the PV phase (1993), the SIS was operated in 4-CCD mode, and the GIS was operated in *PH* mode.

Most of *ASCA* observations listed in Table 6.2−6.5 are conducted simultaneously with the EGRET detector on-board the *CGRO* satellite and/or *Whipple* ground-based Atmospheric Cherenkov Telescope. *CGRO* observations lasts typically two weeks and the observations by *Whipple* lasts several hours per night. Observations with Cherenkov Telescope were performed in clear nights without bright moon. To cover the same time duration with γ-ray detectors in the X-ray band, *ASCA* observations were usually divided into several short time intervals ($\sim$ 10 ksec) during the multi-frequency observations, except for the 'big' campaign of Mrk 421 conducted in 1998.

Table 6.1: TeV blazars observed with *ASCA* & *RXTE*

Source	Other Name	Position RA	(J2000) DEC	(Galactic l	Co-ord) b	z [a] $[d_L]$ [b]	N_H^{gal} [c]	class [d]
1101+384	Mrk 421	166.1138	38.2088	179.832	65.032	0.031 [3.853]	1.45	HBL
1652+398	Mrk 501	253.4676	39.7602	63.600	38.859	0.034 [4.229]	1.73	HBL
2155−304	PKS	329.7169	−30.2256	17.730	−52.246	0.117 [14.72]	1.77	HBL
2344+514	1ES	356.7702	51.7050	112.891	−9.908	0.044 [5.487]	16.0	HBL

[a] redshift of the source.

[b] luminosity distance in the units of 10^{26} cm. The Hubble constant is assumed to be $H_0 = 75$ km s^{-1} Mpc^{-1}.

[c] Galactic column density in the units of 10^{20} cm^{-2}. Elvis et al. (1989) for Mrk 421 and Mrk 501, Stark et al. (1992) for PKS 2155−304 and 1ES 2344+514.

[d] HBL: high-frequency-peaked BL Lac objects. For more detail, see § 2.

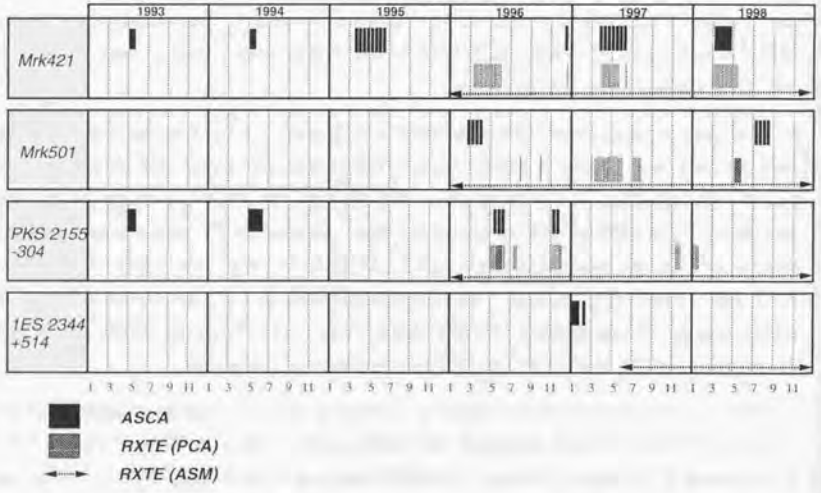

Figure 6.1: Observations of four TeV blazars with *ASCA* & *RXTE*. *black*: *ASCA* observations. *gray*: *RXTE* (PCA) observations. *Arrows* : *RXTE* (ASM) observations.

Table 6.2: *ASCA* observation log of Mrk 421

Source Name	Start (UT)	End (UT)	Exp. SIS	(ksec) GIS	SIS mode [a] bit-H/M	CCD mode [b]
Mrk 421	1993.05.10 03:22	1993.05.11 03:17	38.8	42.8	F/B	0123/2301
	1994.05.16 10:04	1994.05.17 08:06	29.5	38.9	F/B	1111/3333
	1995.04.25 19:16	1995.04.26 03:01	9.3	11.1	F/B	1111/3333
	1995.04.28 06:18	1995.04.28 13:51	8.4	9.3	F/B	1111/3333
	1995.04.29 11:23	1995.04.29 18:36	11.6	12.1	F/B	1111/3333
	1995.05.01 07:46	1995.05.01 15:32	9.9	10.3	F/B	1111/3333
	1995.05.03 11:12	1995.05.03 18:45	11.4	11.5	F/B	1111/3333
	1995.05.05 15:52	1995.05.05 23:51	11.2	11.5	F/B	1111/3333
	1995.05.06 19:05	1995.05.07 03:01	11.4	13.0	F/B	1111/3333
	1995.05.08 06:07	1995.05.08 13:27	11.5	12.4	F/B	1111/3333
	1996.12.15 18:37	1996.12.16 00:51	10.2	11.5	F/B	1111/3333
	1997.04.29 01:45	1997.04.29 08:00	10.1	12.3	F/B	1111/3333
	1997.04.30 01:35	1997.04.30 07:51	9.7	11.7	F/B	1111/3333
	1997.05.01 20:34	1997.05.02 04:06	11.6	13.3	F/B	1111/3333
	1997.05.03 03:23	1997.05.03 10:36	9.5	10.4	F/B	1111/3333
	1997.05.04 04:15	1997.05.04 11:56	10.3	10.9	F/B	1111/3333
	1997.05.06 01:37	1997.05.06 08:32	10.5	11.6	F/B	1111/3333
	1997.06.03 00:12	1997.06.03 06:51	10.2	11.1	F/B	1111/3333
	1998.04.23 23:08	1998.04.30 19:32	257.4	280.6	F/B	1111/3333

[a] F: *Faint* mode, B: *Bright* mode.

[b] CCD chip ID for SIS0/1. "1111/3333" represents nominal 1-CCD mode, while "0123/2301" is nominal 4-CCD mode.

Table 6.3: *ASCA* observation log of Mrk 501

Source Name	Start (UT)	End (UT)	Exp. SIS	(ksec) GIS	SIS mode bit-H/M	CCD mode
Mrk 501	1996.03.21 06:07	1996.03.21 12:01	10.6	11.5	F/B	1111/3333
	1996.03.26 02:57	1996.03.26 10:01	10.8	12.0	F/B	1111/3333
	1996.03.27 16:52	1996.03.27 22:41	10.6	11.5	F/B	1111/3333
	1996.04.02 16:35	1996.04.02 22:21	11.5	12.3	F/B	1111/3333
	1998.07.18 17:52	1998.07.19 04:11	16.1	17.9	F/B	1111/3333
	1998.07.20 19:14	1998.07.21 04:40	15.4	17.0	F/B	1111/3333
	1998.07.21 20:45	1998.07.22 05:21	13.4	15.6	F/B	1111/3333
	1998.07.23 21:47	1998.07.24 06:43	14.6	17.0	F/B	1111/3333

6.2 X-ray Observations with *RXTE*

We analyzed data from 287 *RXTE* observations of three TeV blazars as listed in Table 6.1 (no observation for 1ES 2344+514). The total net exposure was 185 ksec for Mrk

Table 6.4: *ASCA* observation log of PKS 2155−304

Source Name	Start (UT)	End (UT)	Exp. (ksec) SIS	GIS	SIS mode bit-H/M	CCD mode
PKS 2155−304	1993.05.03 20:56	1993.05.04 23:54	34.8	37.3	F/B	0123/2301
	1994.05.19 04:38	1994.05.21 07:56	84.8	96.1	F/B	1111/3333
	1996.05.22 03:14	1996.05.22 06:20	4.3	5.2	F/B	1111/3333
	1996.05.24 04:15	1996.05.24 09:40	9.5	11.0	F/B	1111/3333
	1996.05.26 16:31	1996.05.26 22:07	10.9	11.7	F/B	1111/3333
	1996.11.14 08:46	1996.11.14 20:20	18.2	20.6	F/B	1111/3333
	1996.11.15 09:23	1996.11.15 20:41	18.6	20.9	F/B	1111/3333

Table 6.5: *ASCA* observation log of 1ES 2344+514

Source Name	Start (UT)	End (UT)	Exp. (ksec) SIS	GIS	SIS mode bit-H/M	CCD mode
1ES 2344+514	1997.01.10 15:31	1997.01.11 15:10	36.0	39.8	F/B	1111/3333
	1997.01.23 05:09	1997.01.23 09:30	11.4	11.6	F/B	1111/3333
	1997.12.20 23:22	1997.12.21 05:41	11.3	12.8	F/B	1111/3333

421, 231 ksec for Mrk 501, and 255 ksec for PKS 2155−304. The detail log of *RXTE* observations is given in Appendix A (Table A.1−A.3; Mrk 421, A.4−A.5; Mrk 501, and A.6−A.8; PKS 2155−304). The large effective area of the PCA enables us to obtain high quality spectrum with relatively short observation time (see § 5). Typical exposure for one pointing is $\sim$ 1 ksec, and 20 ksec at the longest. Thus the pointing direction can be changed frequently even within a day.

In this thesis, we analyzed data taken according to our proposal and data sets from the *RXTE* public archive. We carried out 11 observations of Mrk 501 in 1998 May (net exposure time of 60 ksec). For the archival data, we used the data obtained from April 1996 to January 1998. We did not use the data before April 1996, because the reliable background model has not been available for this period
(for more detail, see, http://heasarc.gsfc.nasa.gov/docs/xte/pca_news.html).

In addition to the data taken with the PCA and HEXTE, the ASM data are also used. ASM scans 80 % of the sky in every 90 minutes to monitor the intensity of the brightest 75 X-ray sources. Four TeV blazars are included in the list and constantly monitored for more than 3 years (only 2 years data are available for 1ES 2344+514). Although ASM data is available with a time resolution of 90 minutes, we binned the data into one-day because of the low photon statistics.

All the PCA data analyzed in this thesis were taken by the combination of *standard*-1 mode, *standard*-2 mode, *GoodXenon*1-16*s* mode and *GoodXenon*2-16*s* mode. In this combination, the data extracted from *standard*-2 mode, which has a time resolution of 16 sec, are sufficient for the temporal and spectral analysis presented in this thesis. We also note that we do not use the HEXTE data for the analysis, as we mentioned in § 5.3.

6.3 Individual Targets

Mrk 421

Since the launch of *ASCA* in 1993, we have performed extensive observations of Mrk 421. It spanned more than five years from 1993 to 1998 (Takahashi et al. 1994; 1995; 1998), while observations spanned two years (1996−1997) for *RXTE*.

Our observations are based on two different strategies. First approach is the *continuous* observations for more than 1 day, which enables us uninterrupted monitoring of time evolution of blazars (1993, 1994 and 1998 observations; Table 6.2). In particular, we conducted intensive world-wide campaign in 1998 from radio to TeV. During this campaign, EGRET instrument could not obtain the data due to the deterioration of the detector. Unprecedented continuous coverage in the X-ray band with *ASCA* started from 1998 April 23 to April 30 UT, yielding a net exposure of 280 ksec.

Second approach is the short observations of 8−10 ksec which are spaced between 1 to 3 days apart, such that it covered the GeV/TeV γ-ray observations. Main purpose of this approach was to monitor long term stability, rather than the short term behaviour (1995, 1997 observations with *ASCA* and all *RXTE* observations; Table A.1−A.3). With this approach, we succeeded to have 11 simultaneous observations in keV X-ray and TeV γ-ray bands (see, Table 6.7).

Mrk 501

Observation in 1996 were divided into four short intervals of $\sim$ 10 ksec. One of four observations was done simultaneously with EGRET and *Whipple* (see below) and the observation in 1998 was done simultaneously with the *HEGRA* Cherenkov telescope.

To investigate the rapid time variability for this source, we conducted 2-day continuous observation in 1998 May by *RXTE*. This is probably the longest continuous observation for this source in the X-ray energy band (Table A.5). In order to increase data samples, we extracted data sets from public archive for 1996−1998 observations. This includes the *RXTE* data during the historical highest state in 1997 April to July, as well as the quies-

cent and the intermediate state before/after the flare. Most of the *RXTE* observations of Mrk 501 have exposures of $\sim$ 1 ksec. These observations were separated about one day. 19 observations were conducted *truly* simultaneously in keV X-ray and TeV γ-ray bands.

PKS 2155−304

We analyzed the X-ray data of PKS 2155−304 from 1993 to 1998 observations. We observed the source three times with *ASCA* . *ASCA* observation in 1994 was conducted as a part of multi-frequency campaign (Urry et al. 1997). The *ASCA* observation continued for 2 days (Table 6.4: Kataoka et al. 2000). The observation in 1993 was continuous for one day, but the source was extremely bright that a part of the data is not available because of the saturation of the detectors. In order to monitor the long term variability of the source, the observation in 1996 was divided into 5 short intervals ($\sim$ 10 ksec).

For *RXTE* observations, we used archival data. The *RXTE* observation conducted in 1996 May was a part of multi-frequency campaign. During the campaign, *RXTE* continuously monitored the source for two weeks (Table A.6). 1997 observations were short in time ($\sim$ 1 ksec), but recorded highest flux ever observed for this source. 1997 November observations are partly overlapped with the GeV (EGRET) and TeV (*Durham Mark* 6 Cherenkov telescope) γ-ray observations.

1ES 2344+514

We conducted three *ASCA* observations of 1ES 2344+514 in 1997. One of which was the observation lasted one day and the others are 10 ksec short observations (Table 6.5). No *RXTE* observations have been conducted for this source so far, except for daily monitoring by the All Sky Monitor.

6.4 Simultaneous Observations

6.4.1 X-ray and GeV γ-ray (EGRET) observations

The log of multi-frequency campaigns with EGRET instrument is summarized in Table 6.6. Because of the relatively weak emission of HBLs in the GeV energy band, the sources could not be detected with high significancies ($\geq$ 4 σ) in several observation periods. However, Mrk 421, Mrk 501 and PKS 2155−304 were detected at least once, during the multi-wavelength observations presented in this thesis.

Table 6.6: List of simultaneous X-ray/GeV (EGRET) observations

	EGRET				ASCA	RXTE
Source Name	Viewing Period (VP)	Start (UT) [yymmdd]	End (UT) [yymmdd]	Detection? [a]	[yymmdd]	[yymmdd]
Mrk 421	326.0	940510	940517	YES	940516	—
	418.0	950425	950509	NO	950425	—
					$\sim$ 950508	
Mrk 501	516.5	960321	960403	YES	960321	—
					$\sim$ 960402	
	617.8	970409	970415	NO	—	970409
						$\sim$ 970415
PKS 2155 −304	520.4	960521	960528	NO	960522	960521
					$\sim$ 960526	$\sim$ 960528
	702.0	971118	971125	YES	—	971120
						$\sim$ 971122
	709.1	980106	980113	NO	—	980109
						$\sim$ 980113

[a] YES: GeV γ-rays are detected at $\geq 4\,\sigma$ level. NO : GeV γ-rays are not detected during the observation.

6.4.2 X-ray and TeV γ-ray (*Whipple*) observations

The X-ray observations listed in Table 6.7 were conducted simultaneously with TeV observations with the *Whipple* Cherenkov telescope. For the big campaign, we conducted in April 1998, we obtained additional data from other two TeV Cherenkov telescopes, *HEGRA* and *CAT*. No simultaneous X-ray/TeV observation has been performed for PKS 2155−304 and 1ES 2344+514.

Table 6.7: List of simultaneous X-ray/TeV (*Whipple*) observations

	TeV(*Whipple*) observation			*ASCA*	*RXTE*
Source Name	Start Time [MJD]	End Time [MJD]	significance σ	Start (UT) yymmdd	yymmdd [OBS-ID]
Mrk 421	50567.15	50567.25	—	970429	970429 [P20341-01-04-00]
	50568.15	50568.25	—	970430	970430 [P20341-01-04-01]
	50570.15	50570.25	—	970502	970502 [P20341-01-05-00]
	50571.15	50571.25	—	970503	970503 [P20341-01-05-01]
	50574.15	50574.25	—	970506	970506 [P20341-01-05-05]
	50927.13	50927.29	—	980424	(980424)†
	50928.22	50930.24	—	980425	(980425)†
	50930.14	50930.28	—	980427	(980427)†
	50931.14	50931.28	—	980428	(980428)†
	50932.19	50932.28	—	980429	(980429)†
	50933.22	50932.27	—	980430	(980430)†
Mrk 501	50168.38	50168.48	0.94	960326	—
	50545.36	50545.46	10.32	—	970407 [P20340-04-09/10-00]
	50546.20	50545.30	11.85	—	970408 [P20340-04-11/12-00]
	50547.37	50547.47	7.88	—	970409 [P20340-04-13/14-00]
	50550.33	50550.43	16.32	—	970412 [P20340-04-19/20-00]
	50551.35	50551.45	32.06	—	970413 [P20340-04-21/22-00]
	50552.37	50551.47	22.46	—	970414 [P20340-04-23/24-00]
	50553.37	50553.47	19.83	—	970415 [P20340-04-25/26-00]
	50554.38	50554.48	27.24	—	970416 [P20340-04-27/28-00]
	50570.29	50570.39	7.01	—	970502 [P20340-01-02/03-00]
	50573.31	50573.41	17.80	—	970505 [P20340-01-07/08-00]
	50574.34	50574.44	14.52	—	970506 [P20340-01-09/10-00]
	50575.23	50575.33	12.01	—	970507 [P20340-01-11/12-00]
	50576.30	50576.40	27.50	—	970508 [P20340-01-13/14-00]
	50577.28	50577.38	40.54	—	970509 [P20340-01-15/16-00]
	50582.27	50582.37	8.62	—	970514 [P20340-01-25/26-00]
	50959.29	50959.39	2.86	—	980526 [P30249-01-01-04]
	50960.29	50960.39	3.98	—	970527 [P30249-01-01-06]
	51013.17	51013.27	3.11	980719	—

†: *RXTE* observations were conducted, but data are not in archive. These results are not shown in this thesis.

Chapter 7

Analysis and Results of *ASCA* Observations

7.1 Analysis

7.1.1 Data Reduction

We reduced the data using the analysis softwares supplied by the *ASCA* Guest Observer Facility at the NASA Goddard Space Flight Center (GSFC) and the Institute of Space and Astronautical Science (ISAS). We first selected the data by the orbital conditions of the satellite. The minimum elevation angle from the Earth's limb is 10 and 5 degrees for the SIS and the GIS, respectively. The minimum cutoff rigidity is 6 GeV/c. We excluded the data obtained during the passage through the South Atlantic Anomaly. For the SIS data, we selected the data based on the criterion that the angle between the target and the illuminated Earth's limb is larger than 20 degree, to avoid the contamination by radiation from the Earth's atmosphere.

We next reduced the data by taking the detector performance and stability of satellite attitude into account. Since the attitude of satellite is not stable just after changing the pointing direction, we excluded the data obtained when the difference between the actual Euler angle and scheduled angle is larger than ~ 1 arcmin. We reduced the background in the GIS data by using the information of rise time discrimination (see § 4.4.3). We excluded hot pixels and flickering pixels of the SIS (§ 4.3.3) and selected the normal SIS events with grades 0, 2, 3 and 4 (see, Figure 4.4). The latter selection can effectively reduce background events mainly by charged particles. These criteria for data reduction are summarized in Table 7.1.

For the SIS data, we converted *faint* data to *bright* data and combined all data as

bright data. Since the echo and dark frame errors (§ 4.3.3; 4.3.3) cannot be corrected in *bright* format, we estimated the dark frame errors using *faint* data. The correction of dark frame errors and echo were incorporated in the detector response of the SIS for the spectral analysis.

Table 7.1: Screening criteria for *ASCA* analysis

Screening Item	Screening Criteria SIS 0/1	GIS 2/3
Elevation [a]	10.0	5.0
Cutoff Rigidity [b]	6.0	6.0
SAA Cut [c]	YES	YES
Bright Earth [d]	20.0	—
Maneuver [e]	YES	YES
Grade (SIS only) [f]	0,2,3,4	—
Hot Pixel (SIS only) [g]	YES	—
Rise Time (GIS only) [h]	—	YES

[a] The minimum elevation angle above the Earth's limb
[b] The minimum cutoff rigidity
[c] 'YES' if the data in SAA are excluded
[d] The minimum angle between the target and the illuminated Earth's limb
[e] 'YES' if the data when the attitude of satellite was unstable were eliminated
[f] SIS grade selection (see, Figure 4.4) used in the analysis
[g] 'YES' if the hot pixels and flickering pixels are removed
[h] 'YES' if the rise time discriminator are used to reduce background

7.1.2 Background Subtraction

After the screening processes were done, we separated the source and background photons using the images on the SIS and the GIS. We extracted the source counts from a circular region centered on a target with a radius of 3 arcmin for the SIS (1-CCD mode). This is because the half power diameter of the XRT is 3 arcmin (see, §4.2) and more than 50 % photons are included within a radius of 3 arcmin. For the SIS (4-CCD mode) and the GIS, larger region were selected with a radius of 6 arcmin. The radius used to extract source photons is given in Table 7.2 for each observation.

Most of the TeV blazars analyzed in this thesis are bright, in the sense that the background becomes comparable with source photons only at ≥ 8 keV. In this case, the Cosmic X-ray Background and its fluctuations are negligible compared with the count rate from the source ($\leq 1\%$). However, to measure the flux and spectral form of the faint sources, it is important to subtract both the internal and external background accurately (§ 4.3.3; 4.4.3). In our observations, 1ES 2344+514 is the faintest and needs background subtraction. We also subtracted the background for an observation of Mrk 421 in 1993, because the source was relatively faint during the observation. We performed no background subtraction for other observations (§ 6), to avoid any instrumental artifacts.

Since the background of the SIS detectors is flat on the chip, we estimate the background from the entire chip after subtracting the target region. For the GIS, we estimated the background from the region at the same off-axis angle as the source position. This is because the intrinsic (detector) background is dependent on the distance from the optical axis (e.g., Makishima et al. 1996).

Table 7.2: Image region for source and background spectrum

Source Name	Start Date (UT)	Source radius (arcmin) S0/S1/G2/G3	Background radius (arcmin) S0/S1/G2/G3	Local BGD
Mrk 421	1993.05.10	6/6/6/6	6/6/6/6	L[a]
	1994.05.16	3/3/6/6	—	—[b]
	1995.04.25	3/3/6/6	—	—
	~ 1995.05.08	3/3/6/6	—	—
	1996.12.15	3/3/6/6	—	—
	~ 1997.06.02	3/3/6/6	—	—
	1998.04.23	1/2.6/6/6 [c]	—	—
Mrk 501	1996.03.21	3/3/6/6	—	—
	~ 1996.04.02	3/3/6/6	—	—
	1998.07.18	3/3/6/6	—	—
	~ 1998.07.23	3/3/6/6	—	—
PKS 2155	1993.05.03	6/6/6/6 [d]	—	—
− 304	1994.05.19	3/3/6/6	—	—
	1996.05.22	3/3/6/6	—	—
	~ 1996.05.26	3/3/6/6	—	—
	1996.11.14	3/3/6/6	—	—
	~ 1996.11.15	3/3/6/6	—	—
1ES 2344	1997.01.10	3/3/6/6	3/3/6/6	L
+514	1997.01.23	3/3/6/6	3/3/6/6	L
	1997.12.20	3/3/6/6	3/3/6/6	L

[a] L: local background is subtracted.
[b] Background was not subtracted, because the source was very bright.
[c] Image region of the SIS is small to avoid the effects from the telemetry saturation (see § 7.1.3 for more detail). The GIS light curves were approximately calculated from the count rate on the Lower Discriminator (LD).
[d] Data taken at medium bit rate were not used because the telemetry was strongly saturated.

7.1.3 Treatment of the Telemetry Saturation

In two observations of PKS 2155−304 (1993) and Mrk 421 (1998) (Table 7.2), sources were extremely bright and telemetry was partly saturated. When the telemetry is saturated, the part of of the data are lost before transmitting to the ground station.

The saturation limit is 16 cts/s for the GIS data taken at the medium bit rate (§ 4.4.2). For Mrk 421 observation in 1998, the GIS count rates exceed this limit, hence we approximately estimate the count rate from the hit rate of the Lower Discriminator (LD). We also extracted the data from the period in which effects of the saturation are negligible. For PKS 2155−304 (1993), the GIS was not saturated through the observation.

The saturation limit for the SIS *bright* mode is 32 cts/s when the data are taken at a medium bit rate (1-CCD mode; § 4.3.2). Since the nominal source position is close to the readout gate on the CCD chip, the X-ray events closer to the center of image are read out earlier. Saturated portion on the chip can be eliminated by selecting the narrower source region than usual (3 arcmin). For the Mrk 421 observation in 1998, we found that the effects of saturation is negligibly small when we choose the source radius at 1.0 arcmin for the SIS0, while 2.6 arcmin for the SIS1 (Figure 7.1).

We note that the calibration of the SIS is done assuming the source radius of 3 arcmin. We thus verify that the analysis results do not change even if we choose narrower source region (1 arcmin) than usual. For PKS 2155−304 observation in 1993, all regions on the chips are heavily affected by telemetry saturation, thus we did not use the data taken at medium bit rate (about 60 % in total) because it is very difficult to estimate the flux of the source.

7.2 Results from Temporal Studies

7.2.1 Time Variability

As described in § 2, time variability is one of the marked features of blazars. Four TeV blazars were observed repeatedly with *ASCA* since the launch in 1993 (§ 6). We investigate both the long-term (weeks to years) and the short-term (hours to weeks) variability. We used the GIS data to compare the source count rate, because the GIS has wider field of view than the SIS (§ 4.4.1) and is less affected by the attitude of the satellite and position of the source on the detector.

In the following analysis, the source counts are extracted from a circular region centered on a target with a radius of 6 arcmin for the GIS. The binning time is 1024 sec and the count rate of the GIS2 and the GIS3 are summed in the energy band 0.7−7.5 keV.

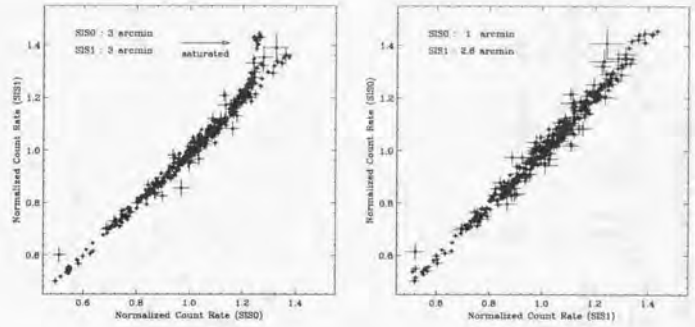

Figure 7.1: Relation of the normalized SIS0 count rate versus normalized SIS1 count rate, during Mrk 421 observation in 1998. *left*; the source radii are 3 arcmin for both the SIS0 and SIS1. Count rates are normalized to their mean values; 20.5 cts/s for the SIS0 and 16.7 cts/s for the SIS1. The SIS0 light curve is saturated when the source was in the brightest state and the data were taken at the medium bit-rate. The effect is indicated by an arrow. *right*; the source radii are 1 arcmin for the SIS0 and 2.6 min for the SIS1. Count rates are normalized to their mean values; 8.2 cts/s for the SIS0 and 15.5 cts/s for the SIS1. The effect of telemetry saturation has disappeared.

Mrk 421

As we see in Figure 7.2, the source was the faintest in 1993 (2−5 cts/s for the GIS) and the brightest in 1998 (10−40 cts/s for the GIS). In addition to this large-amplitude variability on time scales from weeks to years, rapid variability is clearly seen during the observations in 1993 and 1994. Count rate varied by a factor of 2 during a half day period. A small but rapid variability on time-scales of hours to days is also seen in the 1995 and 1997 data. The source intensity varied 40 % or less during 8 hours. In the 1998 observation, the source was extremely bright and the occurrence of day-by-day flare was clearly detected. The subsequent analysis revealed that Mrk 421 was in the historical high state during our observation in 1998 (see, § 7.3).

Mrk 501

The light curves of Mrk 501 are shown in Figure 7.3. To carry out simultaneous monitoring of the source with the γ-ray detectors, we divided our observations into short time intervals ($\sim$ 10 ksec). For the 1996 observations, the flux decreased gradually by a factor of 2 (6 − 3 cts/s for the GIS) on a time scale of two weeks. In 1998, the source was brighter (7 cts/s for the GIS) than 1996 observations. A small flux variation of 30 % was observed

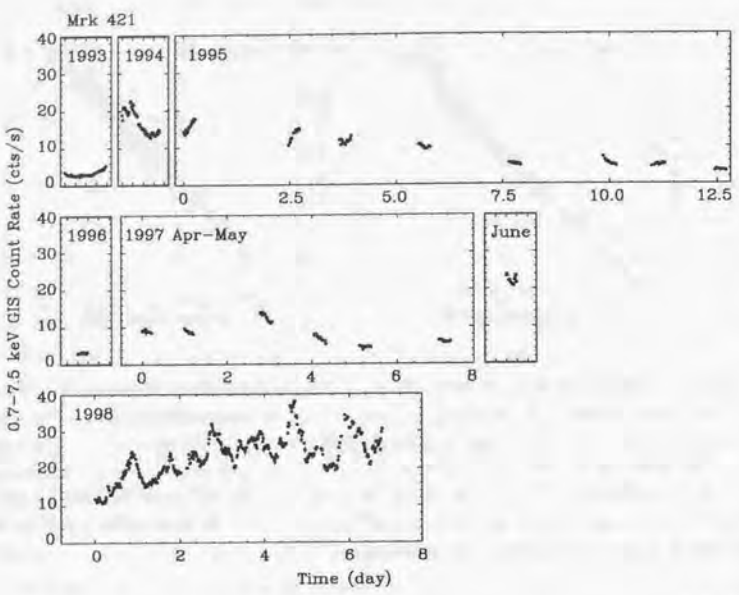

Figure 7.2: The GIS light curves of Mrk 421 from 1993 to 1998 *ASCA* observations. The source counts are extracted from a circular region centered on the target with a radius of 6 arcmin for the GIS. The binning time is 1024 sec. Energy band is 0.7–7.5 keV. The count rate of the GIS2 and the GIS3 are summed. We estimate the GIS count rate from the LD hit rate for 1998 observation, because the source was very bright and the telemetry was partly saturated.

during one-week observation. Contrary to Mrk 421, no significant variability as short as hours is seen in the light curve; a constant fit of the data for each observation (~ 10 ksec) does not indicate any rapid time variability in the sense that $P(\chi^2) < 1\%$.

PKS 2155−304

The light curves of PKS 2155−304 are shown in Figure 7.4. The source was brightest in 1993 (15–23 cts/s for the GIS) and the faintest in 1996 (3–4 cts/s for the GIS), which indicates the changes of more than factor 5 in the flux. Similar to Mrk 421, PKS 2155−304 also shows time variability on time scales as short as hours. The 1993 observation caught a brightening phase. The source varied by 60 % during one day. In 1994, PKS 2155−304 was continuously observed for two days. At the beginning of the 1994 observation, we

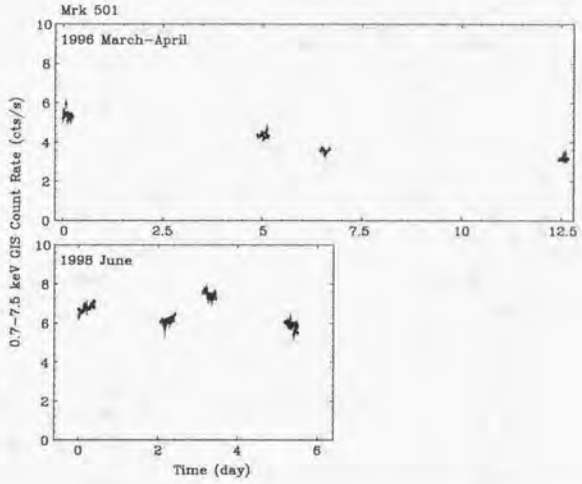

Figure 7.3: The GIS light curves of Mrk 501 from 1996 to 1998 *ASCA* observations. The source counts are extracted from a circular region centered on a target with a radius of 6 arcmin for the GIS. The binning time is 1024 sec. Energy band is 0.7–7.5 keV. The count rate of the GIS2 and the GIS3 are summed.

detected a large flare, where the source intensity varied by a factor of 2 in 8 hours. After the flare, the flux became quite stable but fluctuated with the amplitude of 20 %. In 1996 May observations, the source intensity varied by about 50 % in 4 days, but only 10 % fluctuation during each observation period (4 hours). Two observations in 1996 November showed no significant variabilities or flares.

1ES 2344+514

The light curves of 1ES 2344+514 are shown in Figure 7.5. The source was brightest in January 1997 (0.8 cts/s for the GIS) and faintest in December 1997 (0.5 cts/s for the GIS), which indicates the changes by a factor of ~ 2 in flux. No time variability as rapid as hours was detected during the observations ($P(\chi^2) > 1$ % for a constant fit).

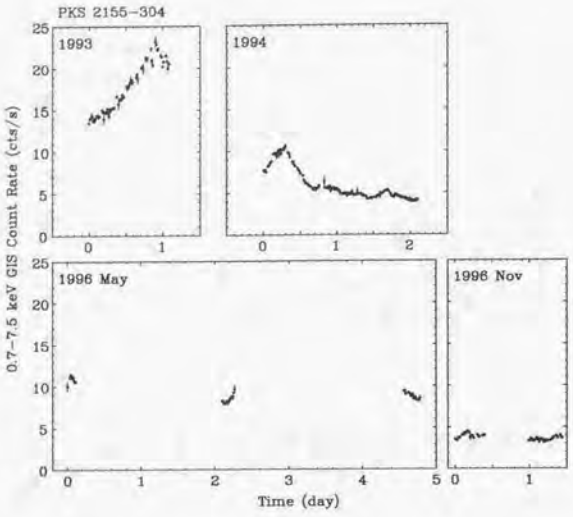

Figure 7.4: The GIS light curves of PKS 2155−304 from 1993 to 1996 *ASCA* observations. The source counts are extracted from a circular region centered on a target with a radius of 6 arcmin for the GIS. The binning time is 1024 sec. Energy band is 0.7−7.5 keV. The count rate of the GIS2 and the GIS3 are summed.

7.2.2 Energy Dependence of Variability

Variability Amplitude

In order to quantify the variability properties, we first introduce the general definition of the fractional *rms* variability parameter (e.g., Rodriguez-Pascual et al. 1997; Zhang et al. 1999). The *rms* variability characterizes the mean variability of the source during the observation. The parameter is defined as follows.

We assume there are data series (a light curve) $F_i(t)$, where i is the ID of the data number ($1 \leq i \leq N$) and t is the time. The standard deviation for this time series is

$$\sigma_F^2 = \frac{1}{N-1} \sum_{i=1}^{N} (F_i(t) - F_{\rm mean})^2, \tag{7.1}$$

where $F_{\rm mean}$ is the mean count rate. We define the *random variance*, due to random errors $\sigma_i(t)$ associated with $F_i(t)$ as

$$\Delta_F^2 = \frac{1}{N} \sum_{i=1}^{N} \sigma_i(t)^2. \tag{7.2}$$

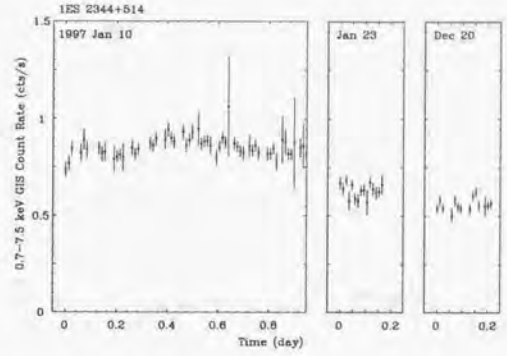

Figure 7.5: The GIS light curves of 1ES 2344+514 in 1997 *ASCA* observations. The source counts are extracted from a circular region centered on a target with a radius of 6 arcmin for the GIS. The binning time is 1024 sec. Energy band is 0.7−7.5 keV. The count rate of the GIS2 and the GIS3 are summed.

The excess variance, $\sigma_{\rm exc}$, is then defined as the difference between the standard deviation σ_F^2 and the random variance Δ_F^2.

$$\sigma_{\rm exc}^2 = \sigma_F^2 - \Delta_F^2. \tag{7.3}$$

Finally, we define the fractional *rms* variability parameter as

$$F_{\rm var} = \sigma_{\rm exc} / F_{\rm mean}. \tag{7.4}$$

Long-Term Trend of Variability

We calculate the $F_{\rm var}$ of four TeV blazars using the GIS light curves shown in Figure 7.2−7.5. To investigate the long-term trend of variability in various energy bands, we divided the GIS light curves into five energy bands: 0.7−1.0 keV, 1.0−1.5 keV, 1.5−2.0 keV, 2.0−3.0 keV and 3.0−7.5 keV.

The results are summarized in Figure 7.6. From the figure, one can find a clear trend such that the amplitude of variability becomes larger as the photon energy increases for all objects studied here. For Mrk 421 data, however, we do not include the 1998 data because we cannot estimate the light curves separated by energy only from the LD count rate. $F_{\rm var}$ was calculated using the data from 1993 to 1997. We calculate the $F_{\rm var}$ of Mrk 421 observation in 1998 using the SIS light curves in the next section.

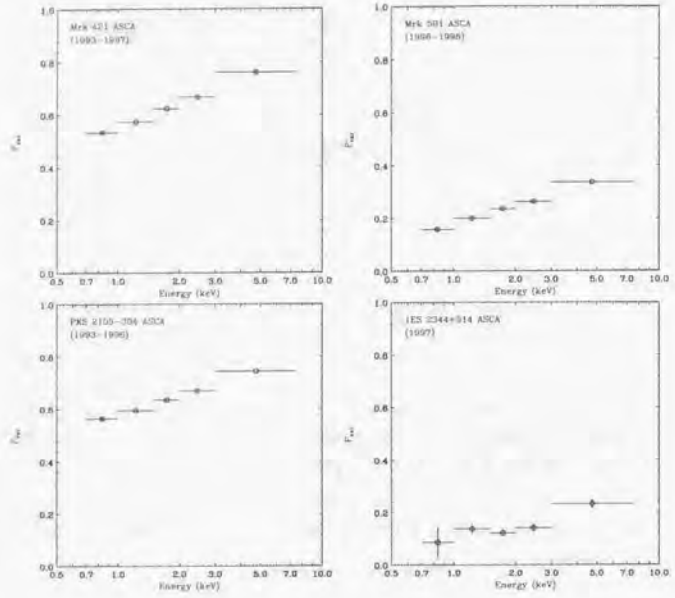

Figure 7.6: Energy dependence of variability of four TeV blazars. The variability parameter was calculated in 0.7−1.0 keV, 1.0−1.5 keV, 1.5−2.0 keV, 2.0−3.0 keV and 3.0−7.5 keV, respectively. For the light curves in total *ASCA* bandpass (0.7−7.5 keV), see Figure 7.2−7.5. *top left*: Mrk 421, *top right*: Mrk 501, *bottom left*: PKS 2155−304, and *bottom right*: 1ES 2344+514. For Mrk 421, we do not include the data in 1998.

Variability of Day-by-Day Flares (Mrk 421 1998)

In order to study the variability of Mrk 421 during the 1998 observation, we use the SIS data binned at 1024 sec. Count rates from the SIS0 and the SIS1 are summed. First, variability was calculated for the total exposure (7 days) in five energy bands, corresponding to 0.5−1.0 keV, 1.0−1.5 keV, 1.5−2.0 keV, 2.0−3.0 keV and 3.0−7.5 keV, respectively. As shown in Figure 7.7, the energy dependence of the variability for Mrk 421 in 1998 is similar to that obtained in 1993−1997 (Figure 7.6).

Since the observation in 1998 continued for 7 days and included ∼10 day-by-day flares (Figure 7.2), we also assess the variability behavior for *each* flare event. For this purpose, we divided the total exposure into 10 segments as shown in Figure 7.8. Except for the first (#1) and the last interval (#10), each segment typically involves one flare event.

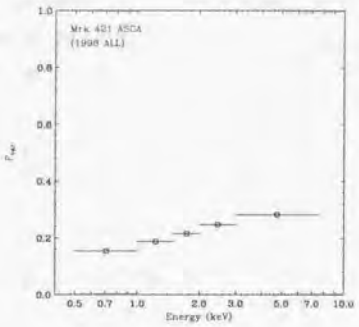

Figure 7.7: Energy dependence of variability of Mrk 421 in 1998. The variability parameter was calculated for the total exposure in five energy bands (0.5−1.0 keV, 1.0−1.5 keV, 1.5−2.0 keV,2.0−3.0 keV and 3.0−7.5 keV). We used the SIS data binned at 1024 sec, because the GIS light curves are strongly saturated.

We calculate the variability parameter $F_{\rm var}$ from time-segments #2 to 9. The energy dependence of variability of individual flares are shown in Figure 7.9, respectively.

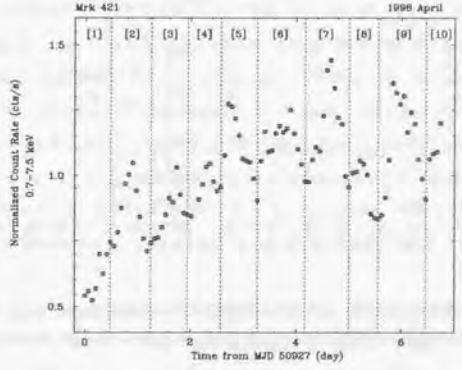

Figure 7.8: The SIS light curve of Mrk 421 obtained in 1998 observation and the division of time interval in 10 separate segments. Each point represents 6 ksec integration of the data.

Four flares exhibit a similar trend to Figure 7.7, such that the variability becomes larger as the photon energy increases (segments # 2,5,7,9), while the energy dependence of variability is flat and not as clear for the flares involved in segments # 3,4,6 and 8. These

results indicate important features for the variability of TeV blazars: on a longer time-scale, variability amplitude becomes larger as increasing photon energy, but for individual flares (or shorter time-scale), the energy dependence of variability changes *flare-by-flare*.

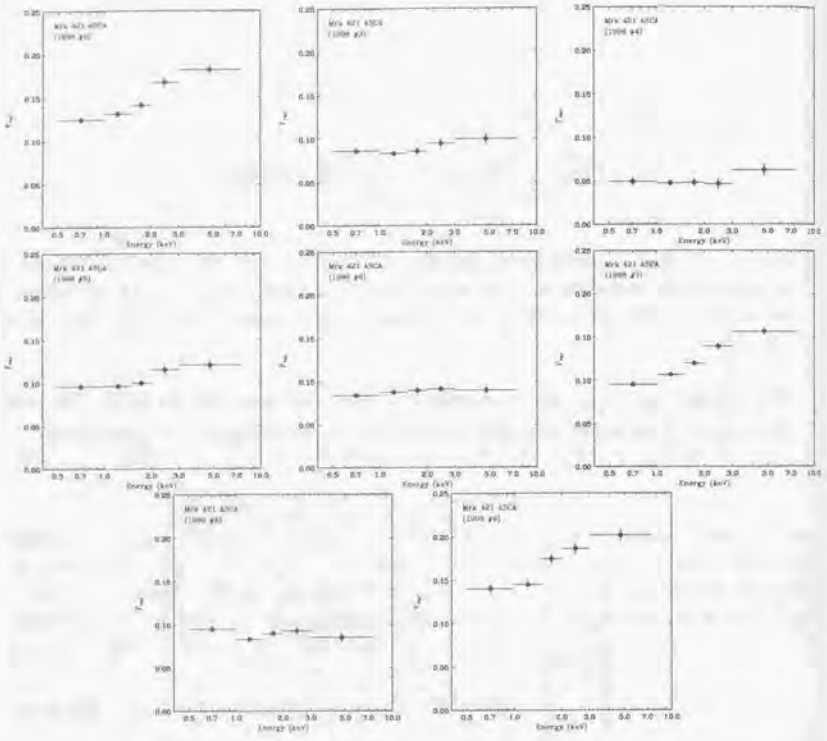

Figure 7.9: Energy dependence of variability of Mrk 421 in 1998 observations. Variability for individual flares is separately shown. Time segments are defined in Figure 7.8. The combined SIS data were used.

7.2.3 Structure Function

In 1998 observation of Mrk 421, we detected day-by-day flares as shown in Figure 7.2. This naturally leads us to an idea that there exists some *preferred* time scale for the rapid variability of blazars. Variability parameter, $F_{\rm var}$, is a measure of the *mean* variability of the source. Since it averages over all the variability during the observation, the more detailed analysis of the time-scale and the time-profile of the variability requires a more sophisticated technique than the $F_{\rm var}$ - type analysis. To quantify the characteristic time scale of the variability and investigate its physical origin, we use a numerical technique called the Structure Function (hereafter the SF).

The definition of the SF and their properties are given by Simonetti et al. (1985). It provides a measure of the mean difference in the flux densities as a function of the separation in the sampling interval. The first order SF is defined as

$$\mathrm{SF}(\tau) = \frac{1}{N}\sum[a(t) - a(t+\tau)]^2, \tag{7.5}$$

where $a(t)$ is a point of the time series $\{a\}$ and summation is made over all pairs, whose separation times are equal to τ. N is the number of such pairs.

The SF analysis gives information similar to power spectrum analysis, but the SF has advantages when examining non-periodic data. In particular, the SF is free from the DC component in the time series, whereas other methods such as Auto Correlation Function (ACF) are not. Furthermore, Hughes et al. (1992) argue that the SF technique provides a method of quantifying time variability without the problems of windowing, and aliasing, which are encountered in the traditional power spectrum analysis techniques.

The SF is closely related to the power spectrum density distribution. If the $\mathrm{SF}(\tau) \propto \tau^{\beta}$ ($\beta > 0$), then the power spectrum has the distribution $P(f) \propto f^{-(\beta+1)}$, where f is frequency (e.g., Paltani et al. 1997; Figure 7.11). Importantly, when the significant time variability does *not* exist below $\tau_{\rm min}$ and $a(t)$ is approximately linear in τ, the SF will be $\propto \tau^2$ in the range $\tau \leq \tau_{\rm min}$.

The SF for a typical measured process consists of three different parts, as schematically shown in Figure 7.10; (i) for the shortest separation times, plateau appears with an amplitude which is just the twice of the variance of the measurement noise ($2\ \sigma^2_{\rm noise}$), (ii) for τ longer than the longest variability time scale, there is a plateau (roll-over) with an amplitude equal to twice the variance of the fluctuation ($2\ \sigma^2_{\rm signal}$), (iii) these regions are linked by a curve whose slope depends on the nature of the intrinsic variation of the source (e.g., red noise, flickering noise, etc). Time scale at which plateau (roll-over; $t_{\rm var}$ in Figure 7.10) appears, is thought to be the *characteristic* time scale of the measured time variability.

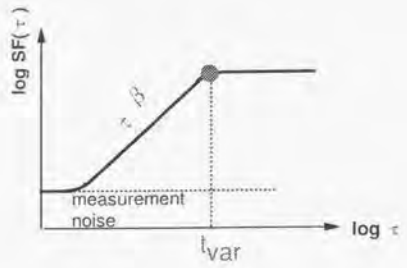

Figure 7.10: Schematic drawing of the 'typical' structure function for a measured time series.

In order to investigate possible systematic errors on the SF analysis, the 1st order SF was calculated for the simulated light curves, whose power spectrum densities are expressed as $P(f) \propto f^{-\alpha}$. We assumed $\alpha = 2.2$ in the following analysis. The length of simulated data was set to 6.7 day, which is similar to the actual observation of Mrk 421 in 1998 (Figure 7.2). To generate the time series, we simply superimposed sine functions with random phases from 0 to 2π, with the constraint that the power in each frequency bin decreases as specified by the power spectrum density. We then extracted the light curve from the simulated data with the actual window for Mrk 421 (1998) observation. The SFs were calculated from thousand sets of simulated light curves prepared with different seeds for the random number generator. Finally, we made the histograms of the SF(τ) for each τ to estimate the systematic errors on the SF.

Simulated SFs are shown in Figure 7.11 with the range of the deviation. The solid line is the ensemble averages of the simulated SFs, while the two dotted lines show the 1 σ *rms*. One finds that the uncertainty of the calculated SF(τ) becomes larger at larger values of τ. It is less than 20 % for $\tau \leq 0.1$ day, while about a factor of 10 for $\tau \geq 5$ day. An oscillation and large errors of the latter is due to insufficient sampling of the data at long time-scale. We should note that in the time region $\tau \geq 0.3 \times$ [Maximum Sampling Interval] (≥ 2 day for this particular data sets), the calculated SFs have an uncertainty of more than factor 2.

We calculate the SFs for the observations whose net exposure times were longer than 40 ksec (§ 6). The results are summarized in Figure 7.12. We mark a time scale by an arrow above which the calculated SF contains large uncertainty of more than factor 2.

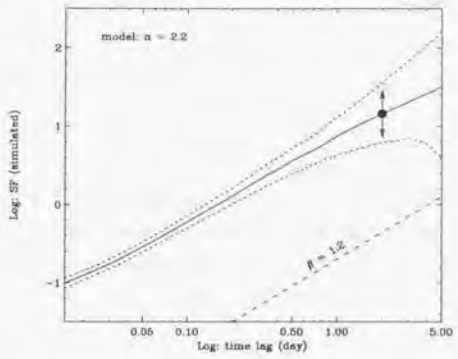

Figure 7.11: Simulated structure function for $P(f) \propto f^{-\alpha}$ ($\alpha = 2.2$). Assumed data length is 6.7 day, which coincides with the Mrk 421 observation in 1998. Solid line is the ensemble average of the SFs produced by the Monte Calro simulations described in the text. Dotted lines are 1 σ *rms* for the simulated SFs. Large dash is a line corresponding to $\beta = 1.2$ (SF $\propto \tau^{\beta}$), drawn to guide an eye. Arrow plotted at $\tau = 2$ (day) indicates that the SF contains the uncertainty of factor 2 at this point.

Mrk 421

The 1st order SFs are separately shown for the 1993 observation (*upper left*), 1994 observation (*upper right*) and the 1998 observation (*middle left*). The SIS data, binned at 1024 sec were used for the calculation. We fitted SF(τ) by a power law $\propto \tau^{\beta}$ in the time domain $0 < \tau/\mathrm{day} < 0.3$. The best fit slopes were $\beta = 1.5 \pm 0.1$ (1993), $\beta = 1.7 \pm 0.1$, and $\beta = 1.2 \pm 0.1$ (1998). For the 1998 data, we clearly detect a roll-over around the time scale $\tau \simeq 0.5$, which corresponds to the typical time scale for an individual flare event. Both 1993 and 1994 observations are too short to identify the same roll-over due to the large errors in the SF.

PKS 2155−304

The SFs of 1993 and 1994 observations are separately shown in Figure 7.12 (*middle right* and *lower left*). Power law slopes of the SFs are $\beta = 2.0 \pm 0.2$ (1993) and $\beta = 1.4 \pm 0.1$ (1994) in $0 < \tau/\mathrm{day} < 0.3$, respectively. For the 1994 data, we see a roll-over around 0.3 day, which corresponds to the rise/decay-time of the large flare event (see, Figure 7.4).

1ES 2344+514 (1997)

The SF for 1ES 2344+514 observation in 1997 are given in Figure 7.12 (*lower right*). The best fit power law index is $\beta = 2.3 \pm 1.1$ for $0 < \tau/\mathrm{day} < 0.3$.

Analysis of Time Asymmetry

It is very intriguing to characterize the shape of the flares seen in the light curves (e.g., § 7.2). Structure function is also viable to test the asymmetry of the light curves. We adopt a convenient approach suggested by Kawaguchi et al. (1998). We separate $\mathrm{SF}(\tau)$ into two parts, SF_+ and SF_-, depending on the sign of $a(t)-a(t+\tau)$;

$$\mathrm{SF}_+(\tau) = \frac{1}{N_+}\sum[a(t) - a(t+\tau)]^2 \quad (\text{for } a(t) - a(t+\tau) < 0), \tag{7.6}$$

$$\mathrm{SF}_-(\tau) = \frac{1}{N_-}\sum[a(t) - a(t+\tau)]^2 \quad (\text{for } a(t) - a(t+\tau) > 0). \tag{7.7}$$

The summation in SF_+ (or SF_-) is made only for pairs that have plus (or minus) signs of $a(t)-a(t+\tau)$, and N_+ (or N_-) are the numbers of such pairs.

The negative sign of $a(t)-a(t+\tau)$ represents the increasing luminosity with time; thus SF_+ approximately indicates the structure function of brightening phases, and similarly, SF_- represents the decaying phases. If the studied light curve is symmetric in time, $\mathrm{SF}_+(\tau)$ and $\mathrm{SF}_-(\tau)$ are expected to coincide with $\mathrm{SF}(\tau)$. On the other hand, if the light curve is characterized with rapid rise and gradual decay, a relation becomes $\mathrm{SF}_+(\tau) > \mathrm{SF}_-(\tau)$.

We calculate $\mathrm{SF}_+(\tau)$ and $\mathrm{SF}_-(\tau)$ for Mrk 421 data obtained in 1998. Since we conducted simultaneous EUV (extreme ultraviolet; 60–90 Å) observation with the *EUVE* during this campaign (§ 9), we also plot the SF for the *EUVE* light curve (see, Figure 9.2). Results are separately shown in Figure 7.13 for *EUVE*, 0.5–2.0 keV, 2.0–4.0 keV and 4.0–7.5 keV data. Upper panels show SF_+, SF_- and usual SF, respectively, while lower panels are the differences between SF_+ and SF_-, normalized by SF. We define the *symmetrical parameter* $\mathrm{Sy}(\tau)$ as

$$\mathrm{Sy}(\tau) = \frac{\mathrm{SF}_+(\tau) - \mathrm{SF}_-(\tau)}{\mathrm{SF}(\tau)}. \tag{7.8}$$

Since we are interested in the symmetry of a single flare event, $\mathrm{Sy}(\tau)$ was calculated in the time region $0 \le \tau \le 0.5$ (day), where 0.5 day is the characteristic time scale of Mrk 421 (Figure 7.12). We averaged over $\mathrm{Sy}(\tau)$ in the time domain $0 \le \tau \le 0.5$ day, and plot them against the photon energy. The results are shown in Figure 7.14. The figure indicates two important results:

(1) $\mathrm{Sy}(\tau)$ is always larger than zero, which indicates the time profile of day-by-day flares of Mrk 421 favours 'rise-time < decay-time'.

(2) Deviations of $\mathrm{Sy}(\tau)$ from zero become smaller as photon energy increases, which indicates that the light curves are more symmetric at higher energies.

Since the light curve of Mrk 421 in 1998 includes many of the flare events and they are superposed on each other, we also applied the same analysis for the light curves after subtraction of the general trend in the light curves. We first fitted the light curves with a quadratic function, then subtracted the best fit function as a 'trend'. We confirmed that the result presented in this section is not affected by the *pileup* of flares. Full details are given in Appendix C.

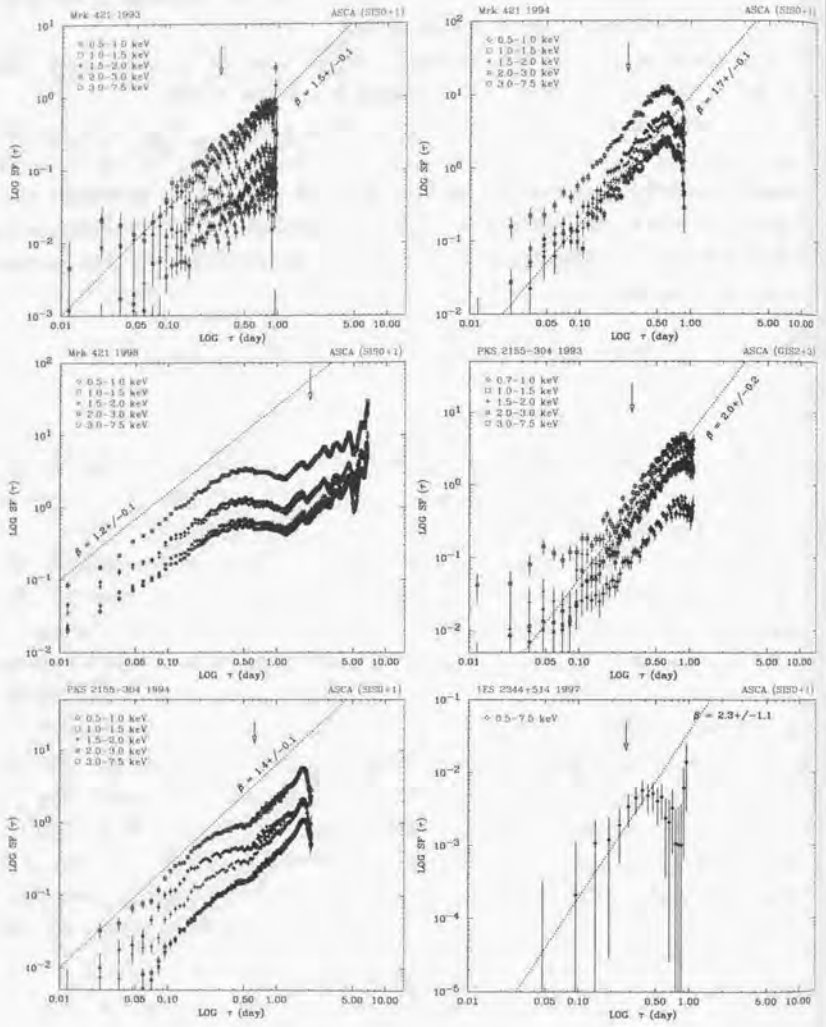

Figure 7.12: 1st order structure function of Mrk 421 (1993; 1994; 1998), PKS 2155−304 (1993; 1994) and 1ES 2344+514. The SFs of various energy bands are shown separately. SF(τ) was fitted by a power law $\propto \tau^{\beta}$ in the time domain $0 < \tau/\mathrm{day} < 0.3$. The best fit index is given in each panel. Arrows indicate the points above which SF values contain uncertainties of more than factor 2. The SIS data were used, except for the PKS 2155−304 observation in 1993.

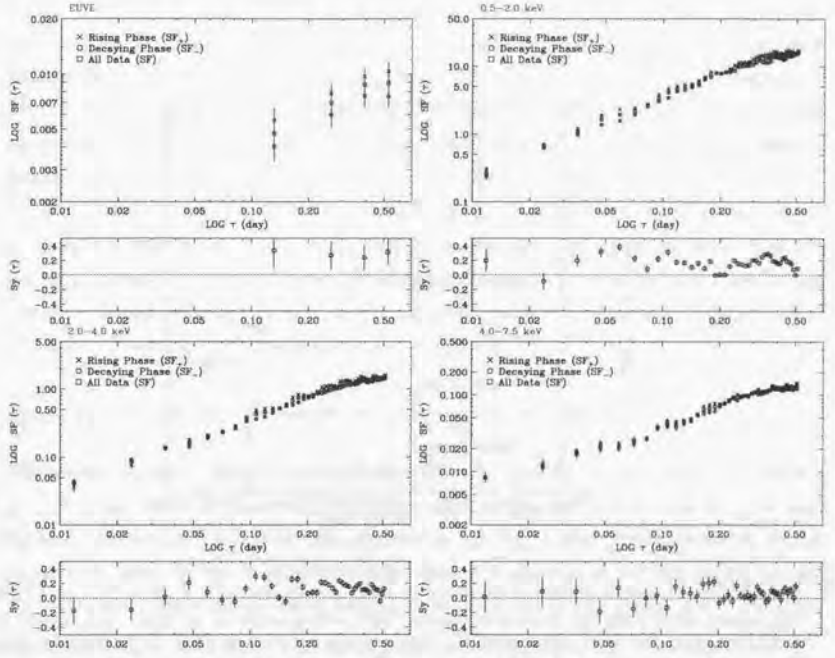

Figure 7.13: Symmetry of the light curves of Mrk 421 (1998) in various energy bands. *top*: 1st order structure function. The data from rising phase (SF_+) and decaying phase (SF_-) are separately shown (see. text). *bottom*: *symmetry* parameter which is defined as $[SF_+ - SF_-]/SF$.

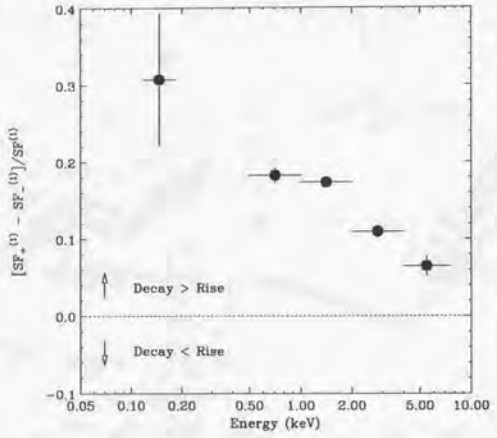

Figure 7.14: Energy dependence of the averaged symmetry parameter $Sy(\tau) = [SF_+ - SF_-]/SF$ for Mrk 421 observation in 1998. $Sy(\tau)$ was averaged over the time lags smaller than 0.5 day. Light curves are almost symmetric, i.e., $[SF_+ - SF_-]/SF \sim 0$ at higher energy band, but at lower energies, the symmetry tends to break down. Corresponding structure functions are given in Figure 7.13.

7.2.4 Spectral Evolutions

In the previous section § 7.2.2, we found that variability amplitude generally becomes larger at increasing photon energy, but on shorter time scales, variety exists as shown in Figure 7.9. Such flare-by-flare behavior may be associated with different spectral evolution of each flare event. Actually, when the variability is larger in a higher energy band, the photon spectra become harder during the flare.

To characterize the spectral evolution of TeV blazars, we investigate the correlation between the count rates (0.7−7.5 keV) and the hardness ratio. We define the hardness ratio as the photon counts in higher energy band (2−7.5 keV) to those in lower energy band (0.7−2 keV). In this expression of the intensity versus hardness, we can also investigate the presence of characteristic hysteresis associated with the 'time-lags' in various energy bands (§ 2.2.3).

We concentrate on the spectral evolution during the continuous observations whose net exposure times were longer than 40 ksec (§ 6). The GIS count rates are used except for the Mrk 421 observation in 1998. In the subsequent analysis, in order to reduce errors and present the time evolution of hardness ratios more clearly, we rebinned the light curves at 6 ksec (12 ksec for 1ES 2344+514 to reduce errors).

Mrk 421

The relations between brightness (count rate) and the hardness ratio for 1993 and 1994 observations are shown in Figure 7.15. In both cases, the general trend is that the spectrum becomes steeper (i.e., relatively less photons in the high energy band) in the declining phase and harder in the brightening phase. Mrk 421 observation in 1994 (§ 7.2) shows the 'clockwise' hysteresis as reported by Takahashi et al. (1996; Figure 2.6). However, the re-analysis of 1993 observation shows a hint of the reverse '*anti*-clockwise' hysteresis, which will be discussed later (§ 7.2.5).

For the 7-day observation in 1998, the spectral evolution in time-segments #2−9 (Figure 7.8) is shown in the separate panels of Figure 7.16. Note that the hardness ratio increased significantly during four of the flares (segments #2, 5, 7, 9) while in others, it did not (segments #3, 4, 6, 8). These results are consistent with what is expected from the energy dependence of the variability amplitude (Figure 7.9).

Strikingly, the spectral evolutions show a complex mixture of the 'clockwise' motions (segments #2, 4), '*anti*-clockwise' motions (segments #3, 6, 8), and 'no significant hysteresis' (segments #5, 7, 9). This clearly indicates that not only the variability amplitudes but also the time-lags may vary flare-by-flare.

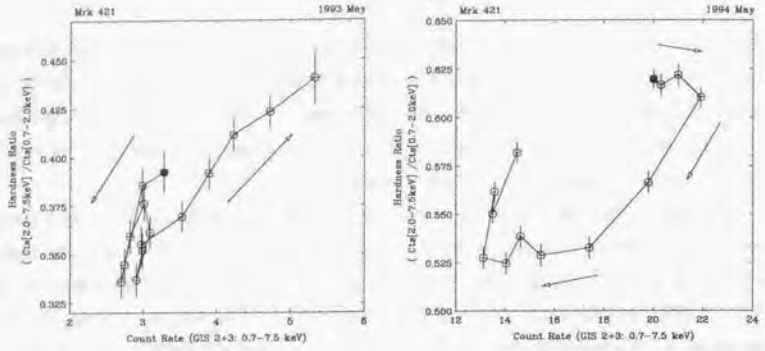

Figure 7.15: The GIS 2+3 count rate (0.7–7.5 keV) versus hardness ratio for Mrk 421 1993 (*left*) and 1994 observations (*right*). Each point represents 6 ksec integration. The large filled circle represents the start point of the observation.

PKS 2155−304

The relation of brightness (count rate) and the hardness ratio for 1993 and 1994 observations of PKS 2155−304 is shown in Figure 7.17. In both cases, the general trend is that the spectrum becomes steeper in the declining phase and harder in the brightening phase, similar to the case for Mrk 421. The figure of 1994 observation shows a clear 'clockwise' hysteresis during the first large-flare (Kataoka et al. 2000), while 1993 observation shows no significant hysteresis. For this particular source, Sembay et al. (1993) has reported both 'clockwise' and the '*anti*-clockwise' patterns using the *GINGA* data.

1ES 2344−514

The relation of brightness (count rate) and the hardness ratio for 1997 observation of 1ES 2344+514 is shown in Figure 7.18. Unfortunately, variability trend is not clear because the source was faint and less variable during the observation.

7.2.5 Search for Time Lags and Time Leads

In the previous section, we found a hint of energy dependent 'time-lags' via the analysis of variability of energy-binned light curves, which causes the diversity in the observed spectral evolution. Importantly, the clockwise hysteresis is expected when the time variations in the low energy band lag behind those in the high energy band, while *anti*-clockwise

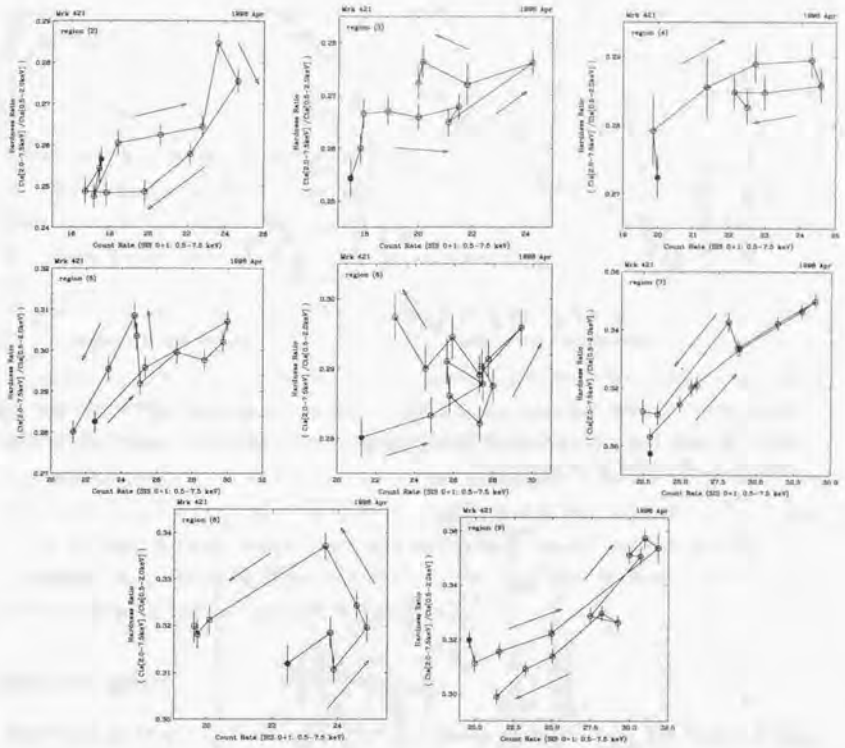

Figure 7.16: Spectral Evolutions of Mrk 421 in 1998 observation. Evolutions in 8 time-segments (#2–9), which were defined in Figure 7.8, are separately shown. Arrows indicates the direction of evolution in the count rate versus hardness ratio plane.

motion is expected in the opposite case (Kirk, Rieger & Mastichiadis 1998; see also § 2.2.3). In this section, we evaluate the time lags more quantitatively in various energy bands.

Discrete Correlation Function (DCF)

In order to study the time series in various energy bands quantitatively, we apply the discrete correlation function given by Edelson & Krolik (1988). This technique was specifically designed to analyze unevenly sampled data sets. The first step is to calculate the

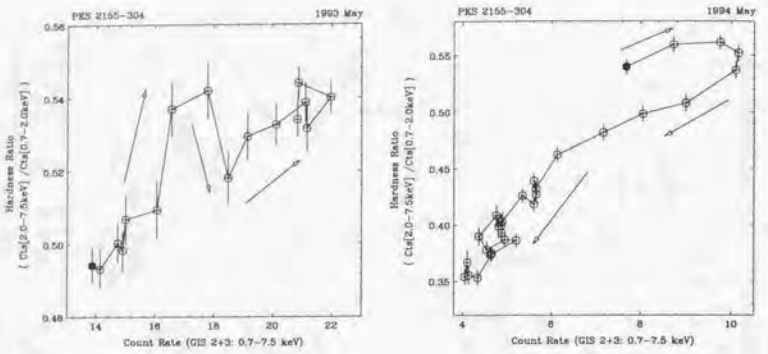

Figure 7.17: The GIS 2+3 count rate (0.7–7.5 keV) versus hardness ratio of PKS 2155–304. *left*: 1993 observation and *right*: 1994 observation. Each point represents 6 ksec integration. The large filled circle is the start point of the observation.

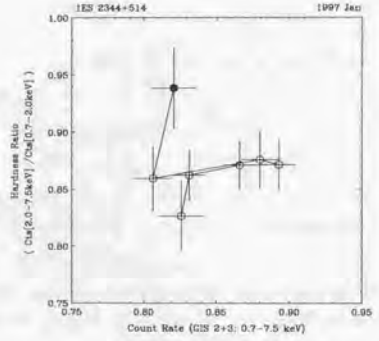

Figure 7.18: The GIS 2+3 count rate (0.7–7.5 keV) versus hardness ratio for 1ES 2344+514 observation. Each point represents 6 ksec integration. The large filled circle is the start point of the observation.

set of unbinned discrete correlation functions (UDCF) between each data point in the two data streams. This is defined in the time domain as

$$\mathrm{UDCF}_{ij} = \frac{(a_i - \bar{a})(b_j - \bar{b})}{\sqrt{\sigma_a^2 \sigma_b^2}}, \tag{7.9}$$

where a_i and b_j are points of the data set $\{a\}$ and $\{b\}$, $\bar{a}$ and $\bar{b}$ are the means of the data sets, and σ_a and σ_b are the standard deviation of each data set. The discrete correlation

function (DCF) for each time lag τ is defined as an average of the UDCF that have the separation time of $\tau - \Delta\tau/2 \leq \Delta t_{ij} \leq \tau + \Delta\tau/2$.

$$\mathrm{DCF}(\tau) = \frac{1}{M} \sum \mathrm{UDCF}_{ij}(\tau), \tag{7.10}$$

where M is the number of pairs in the bin.

The advantage of the DCF lies in the fact that it uses all the data points available, does not introduce new errors through interpolation, and calculates a meaningful error estimates. The standard error for each bin is calculated as

$$\sigma_{\mathrm{DCF}} = \frac{1}{M-1} (\sum [\mathrm{UDCF}_{ij} - \mathrm{DCF}(\tau)]^2)^{1/2}. \tag{7.11}$$

In the following, we calculated the time lags of flux variations in four energy bands (0.5–1.0 keV, 1.0–1.5 keV, 1.5–2.0 keV, and 2.0–3.0 keV) as compared to that in the 3.0–7.5 keV band, using the DCF technique. Both the SIS and the GIS light curves were used for the analysis. The error on the lag was determined from the uncertainty (1 σ error) of the peak parameter obtained by the minimum χ^2 fitting of the DCF distribution to a Gaussian. We also evaluate the errors on the lag using the Monte Calro simulation taking the uncertainties in fluxes into account. We found that both estimates of errors are exactly consistent as described in Appendix C.

Mrk 421 (1993)

The result of Mrk 421 observation in 1993 is shown in Figure 7.19. As indicated from the *anti*-clockwise motion shown in Figure 7.15, one finds that the soft X-ray variability *leads* that in hard X-rays by 5 ksec.

Mrk 421 (1994)

For the Mrk 421 observation in 1994, we see a canonical 'soft-lag' as shown in Figure 7.20. We find that the soft X-ray variation lags behind that in the harder (3.0–7.5 keV) X-ray band by 6 ksec, which is consistent with the results reported in Takahashi et al. (1996).

PKS 2155–304 (1993)

The DCF distributions for PKS 2155–304 observation in 1993 are shown in Figure 7.21. As indicated from no significant hysteresis (Figure 7.17), no significant time lags are found between the hard X-rays and the soft X-rays.

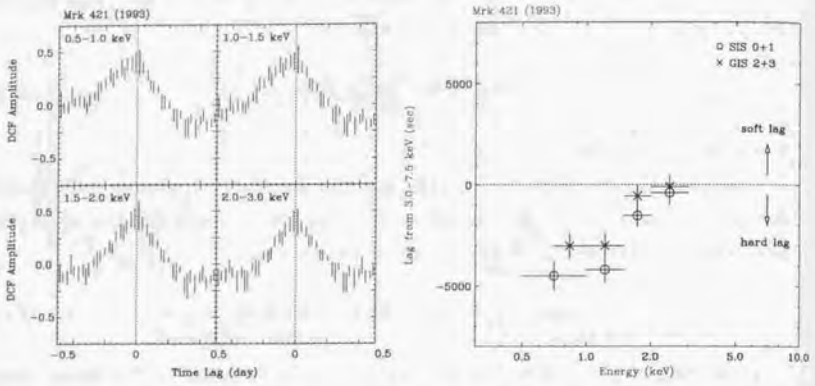

Figure 7.19: *left*: Discrete correlation function of Mrk 421 in 1993. *right*: Time lag of Mrk 421 in 1993.

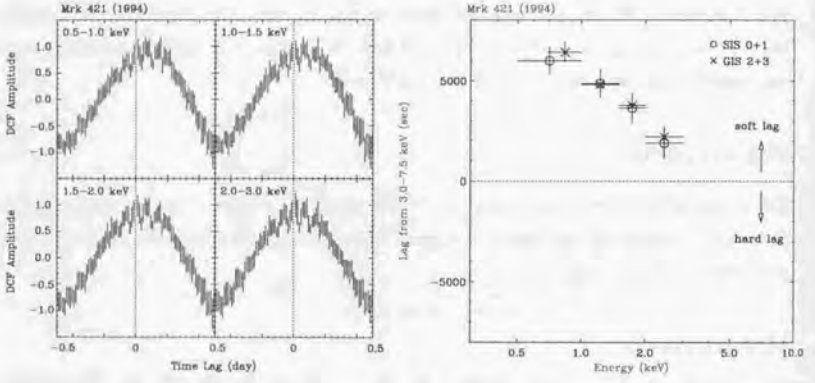

Figure 7.20: *left*: Discrete correlation function of Mrk 421 in 1994. *right*: Time lags of Mrk 421 in 1994.

PKS 2155−304 (1994)

The results for PKS 2155−304 observation in 1994 are shown in Figure 7.22. Although the rising portion of the flare has not been observed, this provides a well-defined and well-sampled light curve for an isolated large flare (see also § 10.2). We found that the

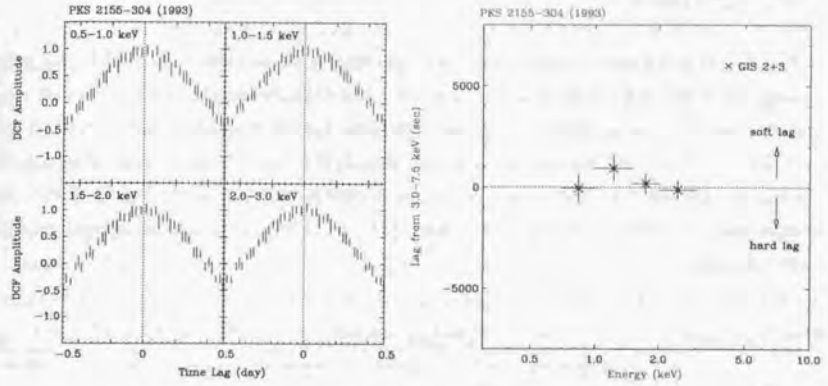

Figure 7.21: *left*: Discrete correlation function of PKS 2155−304 in 1993. *right*: Time lags of PKS 2155−304 in 1993.

soft X-ray variability lags behind that in harder X-rays by 4 ksec (Kataoka et al. 2000).

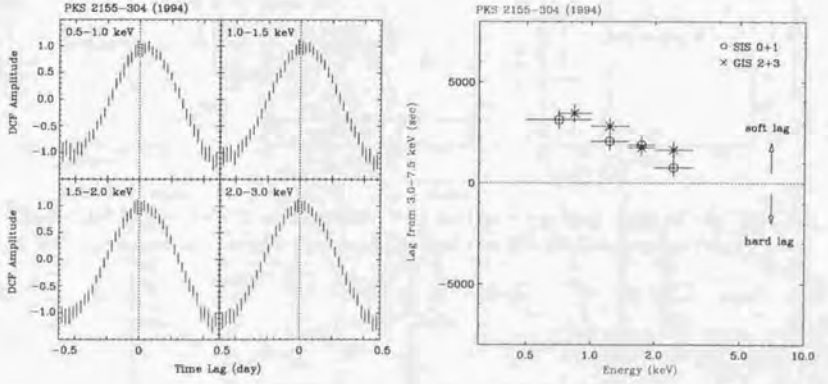

Figure 7.22: *left*: Discrete correlation function of PKS 2155−304 in 1994. *right*: Time lags of PKS 2155−304 in 1994.

Mrk 421 (1998)

For the Mrk 421 data obtained in 1998, we separately calculated the DCFs for eight time-segments (#2–9) defined in Figure 7.8. The DCF distributions for individual time segments are given in Appendix B. Calculated time-lags in four energy bands as compared to 3.0–7.5 keV band are summarized in Figure 7.23. For time segments #2 and 3, we also calculate the time lags using the GIS data, because the source was in a relatively low state and the telemetry was not saturated (§ 7.1.1). The GIS results are consistent with the SIS data.

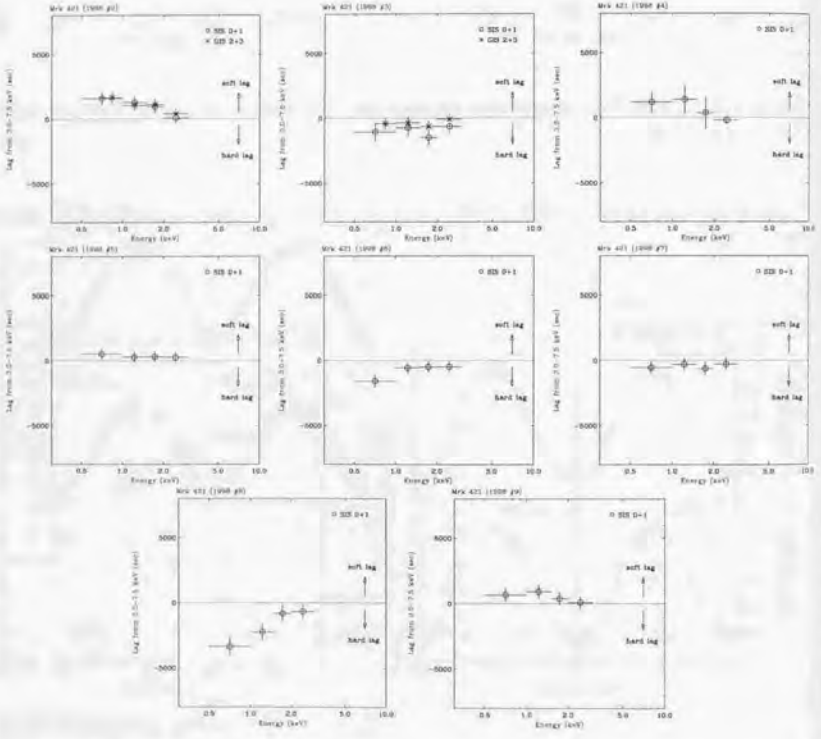

Figure 7.23: Time lags of Mrk 421 in 1998. Time lags in eight time segments (#2-9) defined in Figure 7.8 are separately shown. The DCF distributions for corresponding time segments are given in Appendix B.

We detected the complicated mixture of 'soft lag' (segments #2, 4) and 'hard lag' (segments #3, 6, 8), with several segments showing no apparent time-lag (segments #5, 7, 9). These results are in agreement with the implications from loopwise patterns (Figure 7.16).

We also applied the same analysis for the light curves after subtraction of the general trend in the light curves. We confirmed that the result presented in this section is not affected by the *pileup* of flares. Full details are given in Appendix C.

Combining the above findings with the results shown in § 7.2.2, we notice that the 'hard-lag' flares (region #3, 6, 8) may be associated with the flares whose variabilities have less dependence on energy (Figure 7.9). To see this more clearly, we plot the time-lags versus variability ratio in two energy bands, $F_{\rm var}(3.0{-}7.5\ {\rm keV})/F_{\rm var}(0.5{-}1.0\ {\rm keV})$ in Figure 7.24. Interestingly, an apparent correlation can be seen (the correlation coefficient is 0.7), but more data are necessary to deduce further conclusions.

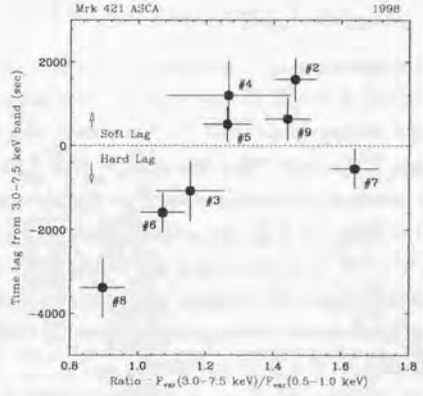

Figure 7.24: Ratio of variabilities in low energy band and high energy band, $F_{\rm var}(3.0{-}7.5\ {\rm keV})/F_{\rm var}(0.5{-}1.0\ {\rm keV})$, versus time lags calculated from the DCF. Data from Mrk 421 observation in 1998.

7.3 Results from Spectral Studies

We performed model fitting to evaluate the photon spectra of blazars. We made the source spectra for the image regions shown in Table 7.2 for observations listed in Table 6.2–6.5. The SIS and the GIS spectra after the background subtraction are shown in Appendix D. All spectra were fitted with the XSPEC version 10.00 provided by NASA/GSFC. The detector response of the SIS is generated from *sisrmg* version 4.2. We use the response version 4.0 for the GIS and 2.10 for the XRT.

7.3.1 Fit with a Power Law Function plus Absorption

We first fitted the spectrum with a power law function plus absorption arising from neutral material. The model function gives

$$\frac{dN}{dE} = N_0 \times \exp(-N_{\rm H} \times \sigma(E)) \times E^{-\Gamma}, \qquad (7.12)$$

where N_0 is the normalization in unit of photons/cm^2/s/keV, Γ is the photon spectral index, and $\sigma(E)$ is the cross section for photo-electric absorption with solar abundances taken from Morrison & McCammon (1983). The absorbing column was parameterized in terms of the equivalent Hydrogen column density $N_{\rm H}$ (Table 6.1).

As the first step, we fixed the column density at the Galactic column density. The results are listed in the Table 7.3. Formally, none of the fits are acceptable, meaning that the probability $P(\chi^2) < 1\%$. One can imagine three reasons for this: (i) photon spectra are not well expressed by a power law form; (ii) photon spectra evolve significantly during the observation; and (iii) consistency between the SIS and the GIS detectors is not good at the lowest energy band ($E < 1$ keV; see below).

In the second step, we fitted the spectrum with the column density $N_{\rm H}$ allowed to be free. We are aware that this is an unphysical model in the sense that the $N_{\rm H}$ can vary with the spectral form, which is unlikely. However, when the spectrum is gradually bending at higher energy bands from a power law form, this can be a convenient expression of the data. The results are also shown in Table 7.3. The fits are significantly improved over those obtained for a fixed $N_{\rm H}$. The best fit values of absorption much larger than the Galactic means that the spectra are convex (i.e., gradually steepening toward higher energy). In order to see the convex spectra of TeV blazar, we fit the data below 1 keV with a power law function plus Galactic absorption (Figure 7.25). large residuals in the ratio of the model to the data above 2 keV are clearly present (*top* and *middle*). The data were taken from the Mrk 421 observation in 1998. We also show the residuals to the power law function with free absorption, where the entire energy bandpass was used

Table 7.3: Fit results of *ASCA* spectra with a power law function plus absorption

Source Name	Start Date	$N_{\rm H}$ 10^{20}/cm^2	Photon Index	Flux (2-10keV) 10^{-12} erg/cm^2/s	χ^2 (d.o.f)	$N_{\rm H}$ 10^{20}/cm^2	Photon Index	χ^2 (d.o.f)
Mrk421	1993.05.10[†]	$9.38^{+0.28}_{-0.29}$	$2.97^{+0.01}_{-0.01}$	24.3±0.1	2.43(1203)	1.456fix	$2.79^{+0.00}_{-0.00}$	3.10(1204)
	1994.05.16[‡]	$9.91^{+0.15}_{-0.15}$	$2.37^{+0.00}_{-0.00}$	256±0.5	2.70(1605)	1.456fix	$2.22^{+0.00}_{-0.00}$	4.81(1606)
	1995.04.25[‡]	$13.55^{+0.30}_{-0.30}$	$2.48^{+0.01}_{-0.01}$	221±0.9	1.35(1369)	1.456fix	$2.26^{+0.00}_{-0.00}$	2.69(1370)
	1995.04.28[‡]	$11.49^{+0.36}_{-0.36}$	$2.44^{+0.01}_{-0.01}$	194±0.9	1.88(1268)	1.456fix	$2.25^{+0.00}_{-0.00}$	2.55(1269)
	1995.04.29[‡]	$12.13^{+0.32}_{-0.32}$	$2.58^{+0.01}_{-0.01}$	152±0.7	1.47(1268)	1.456fix	$2.37^{+0.00}_{-0.00}$	2.42(1269)
	1995.05.01[‡]	$12.21^{+0.37}_{-0.37}$	$2.58^{+0.01}_{-0.01}$	124±0.7	1.36(1159)	1.456fix	$2.42^{+0.00}_{-0.00}$	2.16(1160)
	1995.05.03[‡]	$11.65^{+0.46}_{-0.47}$	$2.71^{+0.01}_{-0.01}$	63.2±0.7	1.19(1001)	1.456fix	$2.49^{+0.01}_{-0.01}$	1.71(1002)
	1995.05.05[‡]	$12.63^{+0.46}_{-0.45}$	$2.77^{+0.02}_{-0.02}$	62.2±0.4	1.19(998)	1.456fix	$2.54^{+0.01}_{-0.01}$	1.99(999)
	1995.05.06[‡]	$12.25^{+0.48}_{-0.47}$	$2.83^{+0.01}_{-0.02}$	52.7±0.4	1.10(965)	1.456fix	$2.60^{+0.01}_{-0.01}$	1.68(966)
	1995.05.08[‡]	$9.89^{+0.55}_{-0.54}$	$2.67^{+0.01}_{-0.01}$	42.1±0.3	1.20(916)	1.456fix	$2.50^{+0.01}_{-0.01}$	1.48(917)
	1996.12.15[‡]	$15.10^{+0.65}_{-0.62}$	$3.06^{+0.02}_{-0.02}$	28.5±0.3	1.36(772)	1.456fix	$2.75^{+0.01}_{-0.01}$	2.05(773)
	1997.04.29[‡]	$17.15^{+0.39}_{-0.38}$	$2.72^{+0.01}_{-0.01}$	108±0.6	1.58(1169)	1.456fix	$2.41^{+0.00}_{-0.00}$	3.20(1170)
	1997.04.30[‡]	$16.83^{+0.40}_{-0.39}$	$2.77^{+0.01}_{-0.01}$	102±0.6	1.61(1125)	1.456fix	$2.46^{+0.00}_{-0.00}$	3.12(1126)
	1997.05.01[‡]	$16.77^{+0.30}_{-0.30}$	$2.72^{+0.01}_{-0.02}$	150±0.6	1.76(1283)	1.456fix	$2.42^{+0.00}_{-0.00}$	4.05(1284)
	1997.05.03[‡]	$15.71^{+0.45}_{-0.44}$	$2.81^{+0.01}_{-0.01}$	76.5±0.5	1.47(1030)	1.456fix	$2.51^{+0.00}_{-0.01}$	2.38(1031)
	1997.05.04	$14.84^{+0.54}_{-0.54}$	$3.00^{+0.01}_{-0.02}$	43.2±0.4	1.23(850)	1.456fix	$2.70^{+0.01}_{-0.01}$	2.02(851)
	1997.05.06[‡]	$15.33^{+0.46}_{-0.45}$	$2.86^{+0.01}_{-0.01}$	63.3±0.4	1.41(992)	1.456fix	$2.57^{+0.01}_{-0.00}$	2.45(993)
	1997.06.02[‡]	$18.21^{+0.25}_{-0.24}$	$2.53^{+0.00}_{-0.01}$	317±0.9	2.86(1444)	1.456fix	$2.22^{+0.01}_{-0.00}$	6.67(1445)
	1998.04.23[‡]	$17.03^{+0.64}_{-0.59}$	$2.53^{+0.00}_{-0.00}$	325±0.3	18.5(1609)	1.456fix	$2.27^{+0.00}_{-0.00}$	64.8(1610)
Mrk501	1996.03.21	$11.25^{+0.49}_{-0.49}$	$2.17^{+0.01}_{-0.01}$	98.2±1.0	1.25(1186)	1.736fix	$2.00^{+0.01}_{-0.01}$	1.60(1187)
	1996.03.26	$11.77^{+0.54}_{-0.53}$	$2.23^{+0.01}_{-0.01}$	74.9±0.5	1.16(1106)	1.736fix	$2.06^{+0.01}_{-0.01}$	1.51(1107)
	1996.03.27	$12.16^{+0.61}_{-0.61}$	$2.36^{+0.01}_{-0.01}$	55.1±0.4	1.14(958)	1.736fix	$2.17^{+0.01}_{-0.03}$	1.47(959)
	1996.04.02	$13.09^{+0.61}_{-0.60}$	$2.45^{+0.01}_{-0.01}$	46.0±0.4	1.11(948)	1.736fix	$2.23^{+0.01}_{-0.01}$	1.52(949)
	1998.07.18[‡]	$13.90^{+0.40}_{-0.40}$	$2.00^{+0.01}_{-0.01}$	129±0.7	1.33(1406)	1.736fix	$1.89^{+0.00}_{-0.00}$	2.06(1407)
	1998.07.20	$13.28^{+0.43}_{-0.43}$	$2.02^{+0.01}_{-0.01}$	114±0.6	1.21(1360)	1.736fix	$1.84^{+0.00}_{-0.00}$	1.79(1361)
	1998.07.21	$13.77^{+0.41}_{-0.41}$	$1.99^{+0.01}_{-0.01}$	144±0.8	1.21(1407)	1.736fix	$1.80^{+0.00}_{-0.00}$	2.01(1408)
	1998.07.23	$12.98^{+0.45}_{-0.45}$	$2.08^{+0.01}_{-0.01}$	110±0.7	1.24(1317)	1.736fix	$1.90^{+0.00}_{-0.00}$	1.77(1318)
PKS2155 −304	[†]1993.05.03[‡]	$7.18^{+0.23}_{-0.23}$	$2.44^{+0.00}_{-0.01}$	252±0.8	1.95(1459)	1.776fix	$2.34^{+0.00}_{-0.00}$	2.34(1460)
	1994.05.19[‡]	$9.45^{+0.16}_{-0.16}$	$2.68^{+0.00}_{-0.00}$	72.4±0.2	2.96(1560)	1.776fix	$2.53^{+0.00}_{-0.00}$	4.57(1561)
	1996.05.22[‡]	$17.56^{+0.54}_{-0.54}$	$2.47^{+0.01}_{-0.01}$	155±1.0	1.76(1063)	1.776fix	$2.18^{+0.01}_{-0.01}$	2.66(1064)
	1996.05.24[‡]	$16.90^{+0.48}_{-0.48}$	$2.72^{+0.01}_{-0.01}$	99.4±0.6	1.78(1036)	1.776fix	$2.42^{+0.01}_{-0.00}$	2.86(1037)
	1996.05.26[‡]	$14.44^{+0.38}_{-0.37}$	$2.48^{+0.01}_{-0.01}$	122±0.5	2.11(1251)	1.776fix	$2.24^{+0.01}_{-0.00}$	3.12(1252)
	1996.11.14[‡]	$12.57^{+0.44}_{-0.43}$	$2.79^{+0.01}_{-0.01}$	43.4±0.3	1.66(1023)	1.776fix	$2.56^{+0.01}_{-0.00}$	2.32(1024)
	1996.11.15[‡]	$10.05^{+0.44}_{-0.43}$	$2.67^{+0.01}_{-0.01}$	41.2±0.3	1.45(1070)	1.776fix	$2.49^{+0.00}_{-0.01}$	1.81(1071)
1ES2344 +514	1997.01.10	$27.65^{+0.88}_{-0.85}$	$2.13^{+0.02}_{-0.02}$	16.0±0.1	4.17(1038)	16.0fix	$1.95^{+0.01}_{-0.01}$	1.37(1039)
	1997.01.23	$30.43^{+1.88}_{-1.85}$	$2.42^{+0.04}_{-0.04}$	9.74±0.2	1.02(435)	16.0fix	$2.18^{+0.02}_{-0.02}$	1.17(436)
	1997.12.20	$26.00^{+2.01}_{-1.88}$	$2.21^{+0.04}_{-0.04}$	9.46±0.2	1.08(441)	16.0fix	$2.05^{+0.02}_{-0.02}$	1.14(442)

[†]: Both the SIS and the GIS data were used, but the data taken at medium bit rate were not used because of the strong telemetry saturation.

[‡]: The source was variable during the observation. Probability for constant fit of the light curve was $P(\chi^2) < 1\,\%$.

All errors are 1 σ.

(Figure 7.25 (*bottom*)).

However, we must note that most of the fit are still unacceptable. As suggested by the rapid time variability and the changes in the hardness ratio (§ 7.2.4), the X-ray spectra

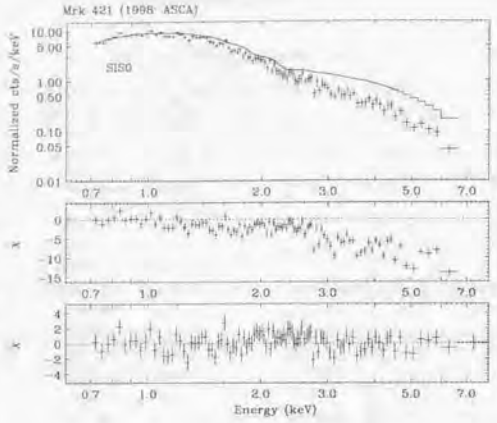

Figure 7.25: *ASCA* SIS0 spectrum fitted to a power law function. *top*; The SIS0 data for Mrk 421 obtained from 1998 04/24 00:48:20 to 04/24 01:45:00, fitted to a power law function with Galactic absorption. Only the data below 1.0 keV was used for the fit. *center*; residuals to a power law function with Galactic absorption. *bottom*; residuals to a power law function with free absorption, where the entire SIS0 bandpass was used.

of the TeV blazars evolve significantly during the observation. Thus in the third step, we divided the observation into short time intervals not to be affected by variations of photon spectra. We cut the exposure into 5 ksec segments for each and fitted the photon spectra for individual time segments. In this case, acceptable fits were obtained ($P(\chi^2) > 1\%$) except for some of the data obtained in 1997/1998 observations (Mrk 421 and Mrk 501; see § 6).

For these recent observations, we have to consider effects caused by the degradation of the on-board detectors more carefully, in particular the SIS. Lower energy region ($E < 1$ keV) is reported to be affected by the SIS degradation. According to Yamashita et al. (1999) and Dotani et al. (1999; private communication), the SIS data shows 'flatter' spectrum than the real spectrum. The discrepancy between the SIS and the GIS spectra might be explained by this effect. In this case, we also test the case where only 1.0−7.5 keV photons are used for the fit. We obtained satisfactory fits in those cases.

The results of combined fit of the SIS/GIS spectra taken from 1998 observation of Mrk 421 are listed in Table 7.4. We selected the time region from 1998 04/24 00:48:20 to 04/24 01:45:00, because these intervals are exactly overlapped with *BeppoSAX* observation, hence the cross-check of the results is possible. We also note that during this interval, the source counts are relatively low and we can use the GIS data as well (§ 7.1.3). The best fit parameters determined respectively by fitting the SIS0, SIS1, GIS2 and GIS3 data are also shown in this Table 7.4. Confidence contour plots of spectral fits are given in Figure 7.26, where contour levels of 1 σ, 90 % and 99 % are shown.

Table 7.4: Results of spectral fitting of Mrk 421 with a power law function plus absorption.

Mission	Detector	$N_{\rm H}$ 10^{20}/cm^2	Photon Index	Flux (2-10keV) 10^{-12} erg/cm^2/s	χ^2 (d.o.f)
ASCA	SIS0	$13.80^{+1.90}_{-1.87}$	$2.66^{+0.05}_{-0.05}$	145±4.4	1.18(98)
	SIS1	$19.05^{+2.25}_{-2.19}$	$2.79^{+0.06}_{-0.06}$	132±4.7	1.10(111)
	GIS2	$5.41^{+3.12}_{-3.01}$	$2.62^{+0.06}_{-0.05}$	149±4.1	0.79(189)
	GIS3	$5.61^{+2.75}_{-2.68}$	$2.65^{+0.05}_{-0.05}$	155±3.8	0.94(205)
	combine (0.7-7.5 keV)	$16.13^{+1.12}_{-1.10}$	$2.72^{+0.03}_{-0.03}$	146±2.1	1.17(611)
	combine (1.0-7.5 keV)	$16.90^{+2.40}_{-2.35}$	$2.72^{+0.03}_{-0.03}$	146±2.1	1.08(544)

Data from 1998 04/24 00:48:20 to 04/24 01:45:00 were used for the fit, when *ASCA* and *BeppoSAX* observed Mrk 421 contemporaneously. Fitting model is a power law function plus free absorption, the *ASCA* energy band. All errors are 1 σ.

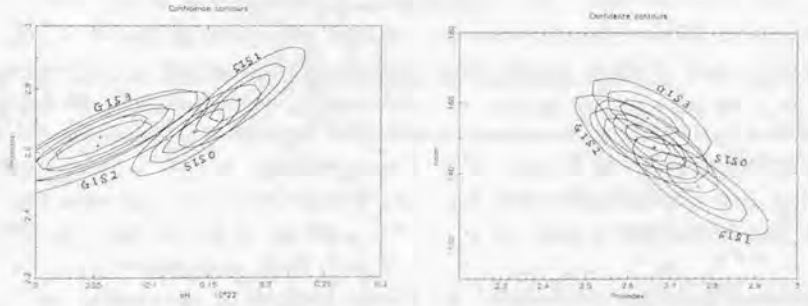

Figure 7.26: Confidence contour plots of spectral fitting for Mrk 421 observation in 1998. Data from 1998 04/24 00:48:20 to 04/24 01:45:00 were used, when *ASCA* and *BeppoSAX* observed Mrk 421 contemporaneously. Three contour levels for 1 σ, 90 % and 99 % errors are shown separately. The result are summarized in Table 7.4.

Results of fitting of all photon spectra of TeV blazars with a power law function plus free absorption, are summarized in Figure 7.27. This figure shows the distribution of luminosity and photon indices, where luminosity is simply calculated from the 2−10 keV

flux multiplied by $4\pi d_L^2$ (see, Table 6.1). One finds two clear trends from this figure; (i) the photon spectra are steeper for high luminosity sources, (ii) the spectra tend to be harder when the source becomes brighter. The latter corresponds to the general trend found in § 7.2.2 that the variability amplitude becomes larger at increasing photon energy. However, broad distribution of fluxes versus photon indices implies that a variety exists for individual flares, as was implied by the day-by-day flares observed in Mrk 421 (Figure 7.7).

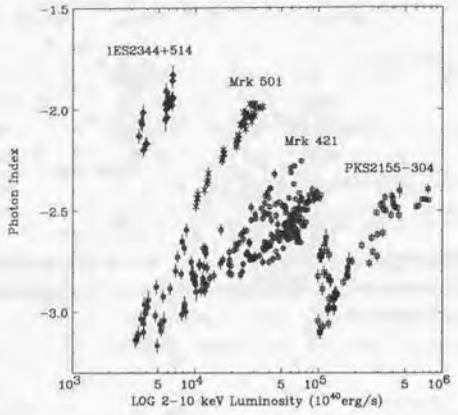

Figure 7.27: Distribution of luminosity and photon indices for all observations with *ASCA* . Mrk 421; from 1993 to 1998 data, Mrk 501; from 1996 to 1998 data, PKS 2155−304; from 1993 to 1996 data, 1ES 2344+514; from 1997 data. Fluxes are simply converted to luminosities by multiplying $4\pi d_L^2$, where d_L is the luminosity distance.

7.3.2 Fit with a Cutoff Power Law Function

Since the photon spectra of TeV blazars show convex shape, we use another model which is expected to fit the spectrum

$$\frac{dN}{dE} = N_0 \times \exp(-N_H^{Gal} \times \sigma(E)) \times E^{-\Gamma} \times \exp(-E_c/E), \tag{7.13}$$

where Γ is the photon index and E_c is the cutoff energy, respectively. This model has two advantages. First, one does not need the Hydrogen column density to vary, which is more physical. Second, the function has a simpler form. One can differentiate the function analytically.

An intrinsic photon spectrum (Galactic absorption corrected) in νF_ν space (e.g., § 2) is expressed as

$$E^2 \frac{dN}{dE} = N_0 \times E^{2-\Gamma} \times \exp(-E_c/E). \tag{7.14}$$

The peak energy E_p and an associated error on E_p are given,

$$E_p = \frac{E_c}{\Gamma - 2} \quad (\Gamma > 2), \qquad \sigma_{E_p} = \sqrt{\frac{1}{(\Gamma-2)^2}\sigma_{E_c}^2 + \frac{E_c^2}{(\Gamma-2)^4}\sigma_\Gamma^2}, \tag{7.15}$$

where σ_{E_c} and σ_Γ are errors on E_c and Γ, respectively. One cannot determine E_p for $\Gamma \leq 2$, because in such cases, the spectra are monotonously rising in the total energy band.

The results are listed in Table 7.5. As were done for the free absorption model in § 7.3.1, we divided the observations into 5 ksec exposure segments and fitted the photon spectra for individual segments. In this case, statistically acceptable fit ($P(\chi^2) > 1\%$) were obtained for all sources.

Figure 7.28 shows an example of the SIS0 spectrum fitted by the cutoff power law function and its residuals. Data are same as Figure 7.25, but the fitting model is the cutoff power law function. The result of combined fit of the SIS/GIS spectra taken from 1998 observation of Mrk 421 are listed in Table 7.6. Goodness of fit is almost equal to that for the free absorption model (Table 7.4).

Results from fitting all the photon spectra of TeV blazars with cutoff power law function are summarized in Figure 7.29. The distribution of peak luminosity L_p versus peak energy E_p is shown. The peak luminosity is simply calculated from the luminosity at $E = E_p$. Four TeV blazars observed with *ASCA* have their peaks in the X-ray energy band; 0.5−2 keV for Mrk 421, 1−4 keV for Mrk 501, 0.5−1.6 keV for PKS 2155−304 and 1.5−3 keV for 1ES 2344+514.

One finds a clear correlation between the E_p and the L_p for both Mrk 421 and Mrk 501, while the correlation is not clear for PKS 2155−304. Correlations found for Mrk 421 and Mrk 501 are quite different; a luminosity change of an order of magnitude would

Table 7.5: Fit result of *ASCA* spectra with a cutoff power law function

Source Name	Start Date	$N_{\rm H}$ 10^{20}/cm^2	E_c keV	Photon Index	Flux (2-10keV) 10^{-12} erg/cm^2/s	χ^2 (d.o.f)
Mrk 421	1993.05.10[†]	1.456x	$0.65^{+0.02}_{-0.02}$	$3.19^{+0.01}_{-0.01}$	24.0±0.2	2.36(1203)
	1994.05.16[‡]	1.456x	$0.62^{+0.01}_{-0.01}$	$2.56^{+0.01}_{-0.01}$	253±0.9	2.76(1605)
	1995.04.25[‡]	1.456x	$0.90^{+0.02}_{-0.02}$	$2.76^{+0.01}_{-0.01}$	217±1.5	1.29(1369)
	1995.04.28[‡]	1.456x	$0.74^{+0.03}_{-0.03}$	$2.67^{+0.01}_{-0.02}$	192±1.6	1.87(1268)
	1995.04.29[‡]	1.456x	$0.80^{+0.02}_{-0.02}$	$2.83^{+0.01}_{-0.01}$	150±1.1	1.46(1268)
	1995.05.01[‡]	1.456x	$0.82^{+0.03}_{-0.03}$	$2.90^{+0.02}_{-0.02}$	122±1.1	1.33(1159)
	1995.05.03[‡]	1.456x	$0.77^{+0.04}_{-0.04}$	$2.95^{+0.02}_{-0.02}$	62.4±0.7	1.20(1001)
	1995.05.05[‡]	1.456x	$0.86^{+0.03}_{-0.03}$	$3.05^{+0.02}_{-0.02}$	61.4±0.7	1.29(998)
	1995.05.06[‡]	1.456x	$0.83^{+0.04}_{-0.04}$	$3.09^{+0.02}_{-0.02}$	52.1±0.6	1.09(965)
	1995.05.08[‡]	1.456x	$0.63^{+0.04}_{-0.04}$	$2.87^{+0.03}_{-0.02}$	41.7±0.5	1.20(916)
	1996.12.15[‡]	1.456x	$1.05^{+0.05}_{-0.05}$	$3.40^{+0.03}_{-0.03}$	28.1±0.5	1.38(772)
	1997.04.29[‡]	1.456x	$1.18^{+0.03}_{-0.03}$	$3.09^{+0.02}_{-0.02}$	106±1.2	1.54(1169)
	1997.04.30[‡]	1.456x	$1.17^{+0.03}_{-0.03}$	$3.14^{+0.02}_{-0.02}$	100±1.1	1.55(1125)
	1997.05.01[‡]	1.456x	$1.16^{+0.02}_{-0.02}$	$3.09^{+0.01}_{-0.01}$	144±1.2	1.71(1283)
	1997.05.03[‡]	1.456x	$1.08^{+0.03}_{-0.03}$	$3.15^{+0.02}_{-0.02}$	75.3±0.9	1.46(1030)
	1997.05.04	1.456x	$1.02^{+0.04}_{-0.04}$	$3.32^{+0.03}_{-0.03}$	42.7±0.7	1.24(850)
	1997.05.06[‡]	1.456x	$1.06^{+0.03}_{-0.03}$	$3.20^{+0.02}_{-0.02}$	62.4±0.8	1.40(992)
	1997.06.02[‡]	1.456x	$1.24^{+0.02}_{-0.02}$	$2.91^{+0.01}_{-0.01}$	310±2.1	2.79(1444)
	1998.04.23[‡]	1.456x	$1.10^{+0.00}_{-0.00}$	$2.85^{+0.00}_{-0.00}$	320±0.6	19.5(1609)
Mrk 501	1996.03.21	1.736x	$0.67^{+0.03}_{-0.03}$	$2.37^{+0.02}_{-0.02}$	97.0±0.9	1.26(1186)
	1996.03.26	1.736x	$0.7^{+0.04}_{-0.04}$	$2.45^{+0.02}_{-0.02}$	74.0±0.8	1.17(1106)
	1996.03.27	1.736x	$0.75^{+0.04}_{-0.04}$	$2.59^{+0.03}_{-0.03}$	54.3±0.72	1.15(958)
	1996.04.02	1.736x	$0.82^{+0.04}_{-0.04}$	$2.70^{+0.03}_{-0.03}$	45.4±0.6	1.12(948)
	1998.07.18[‡]	1.736x	$0.85^{+0.03}_{-0.03}$	$2.25^{+0.01}_{-0.01}$	127±1.1	1.32(1406)
	1998.07.20	1.736x	$0.80^{+0.03}_{-0.03}$	$2.26^{+0.02}_{-0.02}$	112±1.1	1.21(1360)
	1998.07.21	1.736x	$0.82^{+0.03}_{-0.03}$	$2.22^{+0.01}_{-0.02}$	141±1.2	1.35(1407)
	1998.07.23	1.736x	$0.77^{+0.03}_{-0.03}$	$2.30^{+0.02}_{-0.02}$	108±1.1	1.26(1317)
PKS 2155 -304	[†]1993.05.03[‡]	1.776x	$0.43^{+0.02}_{-0.02}$	$2.58^{+0.01}_{-0.01}$	249±1.2	1.88(1459)
	1994.05.19[‡]	1.776x	$0.57^{+0.01}_{-0.01}$	$2.86^{+0.01}_{-0.01}$	71.8±0.3	2.99(1560)
	1996.05.22[‡]	1.776x	$1.14^{+0.04}_{-0.04}$	$2.82^{+0.02}_{-0.02}$	152±2.0	1.77(1063)
	1996.05.24[‡]	1.776x	$1.13^{+0.04}_{-0.04}$	$3.08^{+0.02}_{-0.02}$	97.7±1.3	1.78(1036)
	1996.05.26[‡]	1.776x	$0.92^{+0.03}_{-0.03}$	$2.76^{+0.02}_{-0.02}$	120±1.1	2.14(1251)
	1996.11.14[‡]	1.776x	$0.82^{+0.03}_{-0.03}$	$3.05^{+0.02}_{-0.02}$	42.9±0.5	1.66(1023)
	1996.11.15[‡]	1.776x	$0.61^{+0.03}_{-0.03}$	$2.85^{+0.02}_{-0.02}$	40.8±0.4	1.47(1070)
GIS he 1ES 2344 +514	1997.01.10	16.06x	$0.79^{+0.06}_{-0.06}$	$2.36^{+0.03}_{-0.03}$	15.7±0.3	1.17(1038)
	1997.01.23	16.06x	$1.04^{+0.13}_{-0.13}$	$2.73^{+0.07}_{-0.07}$	9.55±0.4	1.02(435)
	1997.12.20	16.06x	$0.70^{+0.14}_{-0.14}$	$2.42^{+0.08}_{-0.07}$	9.33±0.4	1.08(441)

[†] : Data from both SISs were used, but the data taken at medium bit rate were not used because of the strong telemetry saturation.

[‡] : The source was variable during the observation. Probability for constant fit of the light curve was $P(\chi^2) < 1$ %.

All errors are 1 σ.

cause only factor 2 change in the peak position for Mrk 421, while it makes more than factor 40 change for the case of Mrk 501.

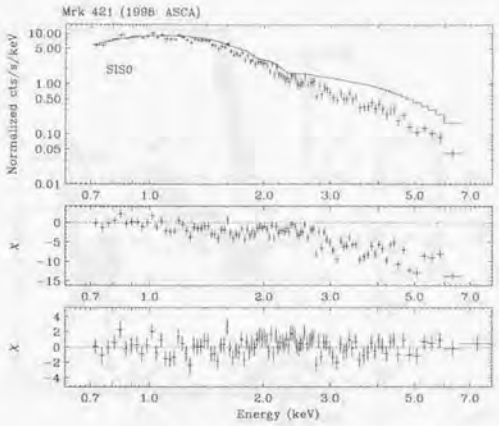

Figure 7.28: *ASCA* SIS0 spectrum fitted to a cutoff power law function. *top*: The SIS0 data for Mrk 421 obtained from 1998 04:24:00:48:20 to 04/24 01:45:00, fitted to a power law function with Galactic absorption. Only the data below 1.0 keV were used for the fit. *center*: residuals to a power law function with Galactic absorption. *bottom*: residuals to a cutoff power law function with Galactic absorption, where the entire SIS0 bandpass were used.

Table 7.6: Results of spectral fitting of Mrk 421 with a cutoff power law function.

Mission	Detector	E_c (keV)	Photon Index	Flux (2-10keV) 10^{-12} erg/cm^2/s	χ^2 (d.o.f)
ASCA	SIS0	$1.00^{+0.15}_{-0.15}$	$3.00^{+0.09}_{-0.09}$	142±7.3	1.14(98)
	SIS1	$1.40^{+0.18}_{-0.17}$	$3.25^{+0.11}_{-0.11}$	129±9.3	1.07(111)
	GIS2	$0.31^{+0.21}_{-0.21}$	$2.72^{+0.11}_{-0.11}$	148±8.5	0.79(189)
	GIS3	$0.31^{+0.19}_{-0.18}$	$2.74^{+0.10}_{-0.10}$	154±7.9	0.94(205)
combine (0.7-7.5 keV)		$1.11^{+0.08}_{-0.08}$	$3.07^{+0.05}_{-0.05}$	143±2.1	1.16(611)
combine (1.0-7.5 keV)		$0.99^{+0.14}_{-0.14}$	$3.01^{+0.07}_{-0.07}$	144±7.4	1.06(544)

Data from 1998 04:24:00:48:20 to 04/24 01:45:00 were used for the fit, when *ASCA* and *BeppoSAX* observed Mrk 421 contemporaneously. Fitting model is a power law function plus exponential cutoff. The absorption is fixed to the Galactic value. the *ASCA* energy band. All errors are 1 σ.

7.3.3 Shift of the Synchrotron Peak

As shown in Figure 7.29, the peaks of νF_ν spectra are found in the X-ray energy band for the four TeV blazars studied by us. Considering the convex curvature of the X-ray photon spectra, this is likely to be because the peak of the synchrotron (LE) component

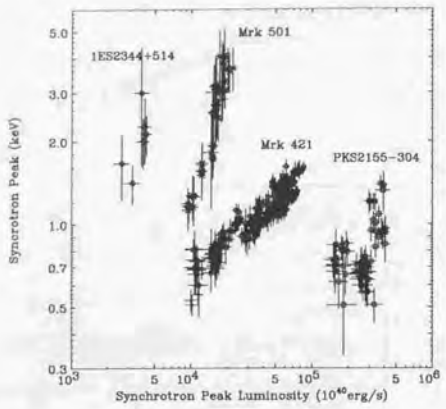

Figure 7.29: Distribution of peak luminosity L_p versus peak energy energy E_p as described in the text.

is located in the X-ray band (see § 2).

To see the time evolution of the photon spectra more clearly, we show the photon spectra in νF_ν space (Figure 7.30). The SIS spectra were convolved from the cutoff power law function. We divided the total *ASCA* bandpass (0.7−7.5 keV) into 22 logarithmic-equal energy bands to reduce errors. Figure 7.30 shows the combined results from different observations. The spectral evolutions during individual observations are summarized in Appendix E (Figure E.1−E.2).

Mrk 421

Mrk 421 shows very modest shifts in the peak position. In 1993 observation, when the source was the faintest, the peak was located below 0.7 keV. For 1994−1997 observations, we detected the peak around 1 keV. When the source was the brightest in 1998, flux increased more than a factor of 30 than that in 1993 and the peak was detected at ~ 2 keV. A correlation between peak energy E_p and peak luminosity L_p is expressed as $E_p \propto L_p^{0.36}$ (see, Figure 7.29).

Mrk 501

In 1996 April observation when Mrk 501 was in the faintest state, the synchrotron peak was detected at 1 keV. For 1998 observations, the peak was shifted to a significantly higher energy (4 keV) although an increase in flux was relatively small (factor of 2). For

this source, a clear correlation between the peak energy and the peak luminosity can be expressed as $E_p \propto L_p^{1.6}$ (see, Figure 7.29).

PKS 2155−304

PKS 2155−304 was brightest in 1993, while it was the faintest in 1996. Interestingly, however, synchrotron peak exists below 0.7 keV during 1993 observation, but around 1 keV during 1996 observation. The spectra in the lowest state of 1994 observation are very similar to that in the 1993 observation, but the flux is lower by a factor of 4. There seems no clear correlation between E_p and L_p, as was suggested from Figure 7.29.

1ES 2344+514

1ES 2344+514 was brightest in January 10 (1997), while it was the faintest in December 20 (1997). Synchrotron peak seems to be shifted from 1 keV to 4 keV corresponding to the factor 2 increase in the flux. This suggest that the spectral evolution of 1ES 2344+514 is similar to that for Mrk 501, but not conclusive because of the low photon statistics, and because there are relatively few *ASCA* observations. .

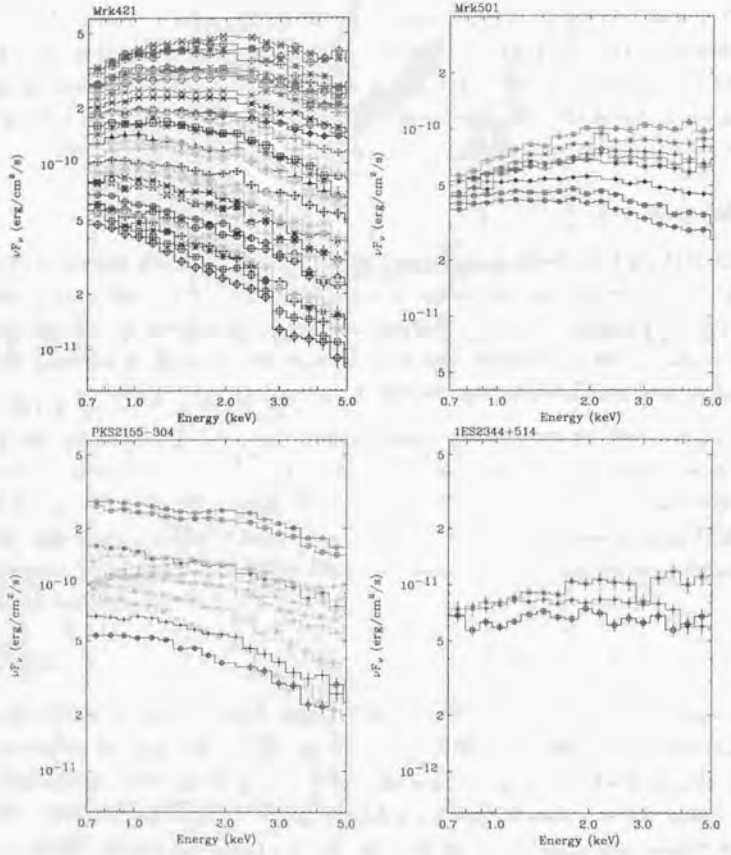

Figure 7.30: Synchrotron peak shifts of four TeV blazars. *top left*: Mrk 421, *top right*: Mrk 501, *bottom left*: PKS 2155−304 and *bottom right*: 1ES 2344+514.

Chapter 8

Analysis and Results of *RXTE* Observations

8.1 Analysis

8.1.1 Data Reduction

To reduce the PCA data, we first selected the data by orbital conditions and pointing stability. The minimum elevation angle from the Earth's limb was set to be 10 degrees. We excluded the data obtained during the passage through the South Atlantic Anomaly (SAA). Since the PCA detector is activated during the SAA and the background increases significantly just after the passage, we only use the data when the background goes back to the quiescent level and becomes quite stable, which is typically 30 minutes after the SAA passage. Since the attitude of satellite is not stable just after changing the pointing direction, we excluded the data obtained when the difference between the actual pointing direction and scheduled direction is larger than 1.2 arcmin.

Next we eliminated the data which includes significant electron contamination. Electrons creates background components by interaction with spacecraft or detector body. To analyze the faint sources, the PCA team recommends filtering out time when electron rate is larger than 0.1, which is the criterion used in this thesis. Additional data selections had been done from various operational reasons.

In March 1996, PCU3 and PCU4 began to experience occasional breakdowns. Since then, these two PCUs, individually or together, are occasionally turned off to prevent further damage. We thus used the data only from 3 PCUs (PCU0/1/2) whose exposure times are much larger and uninterrupted than those for PCU3 and PCU4. The PCUs have three xenon layers (X1, X2, X3) each consisting of two anodes chains (Left, Right). The

top layer detects roughly 90 % of the cosmic photons and 50 % of the internal instrumental background. Thus the best signal-to-noise for weak sources are achieved by selecting only events from the top layer (X1) and excluding events from the mid and bottom layers (X2 and X3). These criteria for data reduction are summarized in Table 8.1.

Table 8.1: Screening criteria for *RXTE* analysis

Screening Item	Screening Criteria
Elevation [a]	< 10.0
Att. Stability[b]	< 1.2 arcmin
Time since SAA[c]	> 30 min
Electron Rate[d]	< 0.1
PCU_ON[e]	PCU_0, 1, 2 (PCU_3, 4 were not used)
Layer[f]	X1 only (X2, X3 were not used)

[a] The minimum elevation angle above the Earth's limb
[b] The maximum fluctuation in the pointing direction
[c] The minimum time since the SAA passage
[d] The maximum rate for electron background
[e] ID of PCUs used in the analysis
[f] ID of PCU layers used in the analysis

8.1.2 Background Subtraction

After the screening processes were done, we estimated the PCA background for each observation. Since the PCA is not an imaging detector, the modeled background has to be subtracted from the source data. The PCA background consists of two components (see, § 5.2.3). One is the diffuse sky background which enters through the collimator as X-rays, and the other is the internal background which arises from interactions between radiation or particles in orbital environment with the detector or spacecraft. While the sky background is assumed to be constant at any one pointing position, the internal background may vary as the detectors move through different ambient conditions. The estimation of background is based on the detailed modeling of activation, especially during the SAA passage and instantaneous particle flux coming into the detector.

To estimate the background, we use the latest version of *pcabackest* (Version 2.1b) supplied from *RXTE* Observer Facility at the NASA GSFC. It is assumed that the internal background varies on a time scale long compared to 16 seconds, the natural time scale of the PCA *Standard*-2 data (see § 5). The background model was evaluated once

every 16 seconds, and the equivalent of a *Standard*-2 data file was created with separate information for each detector and each anode chain. We applied all of the good time intervals to the output files from *pcabackest* exactly as we did to the *Standard*-2 data.

8.2 Results from Temporal Studies

8.2.1 Time Variability

We first study the time variability for each source, by means of PCA count rates during the observations. Count rates are extracted from the sum of the PCU 0, 1 and 2 data. To obtain the best signal-to-noise ratio, only the data for the PHA channels from 6 (2.5 keV) to 53 (20 keV) were used in the following analysis.

Mrk 421

The light curves of Mrk 421 from 1996 to 1997 observations are shown in Figure 8.1. The source was the faintest in 1996 December (4–5 cts/s for PCA) and the brightest in 1996 May (20–152 cts/s for PCA), which was the change of more than factor of 30. Note that the amplitude of variation is larger than that observed with *ASCA* in lower X-ray energy bands (Figure 7.2). In addition to this large-amplitude, long term variability, the data reveal very rapid variability, on time scales as short as hours to days. In particular, flux variations in 1996 May (Figure 8.1 (b)) are remarkable, where the flux increased and decreased by a factor of 6 within a day. The occurrence of day-by-day flares is implied from the figure, as was clearly detected during the 1998 observation with *ASCA* (Figure 7.2).

Mrk 501

The light curves of Mrk 501 are summarized in Figure 8.2. The source was the faintest in 1998 May (26–34 cts/s for PCA) and the brightest in 1997 Apr–July (68–201 cts/s for PCA), which was a change of a factor ∼10. Subsequent analysis revealed that the fluxes observed in 1997 Apr/July are the historical record for this source (Figure 8.2 (d)(f)). In 1998 May, we monitored the source almost continuously for two days to search for the rapid time variability (fig 8.2 (g)). About 30 % fluctuation in the flux was detected, but the source did not show any significant variations as short as hours.

PKS 2155–304

The light curves of PKS 2155–304 from 1996 to 1998 observations are shown in Figure 8.3. The source was the faintest in 1998 January (4–13 cts/s for PCA; (e)) and the brightest

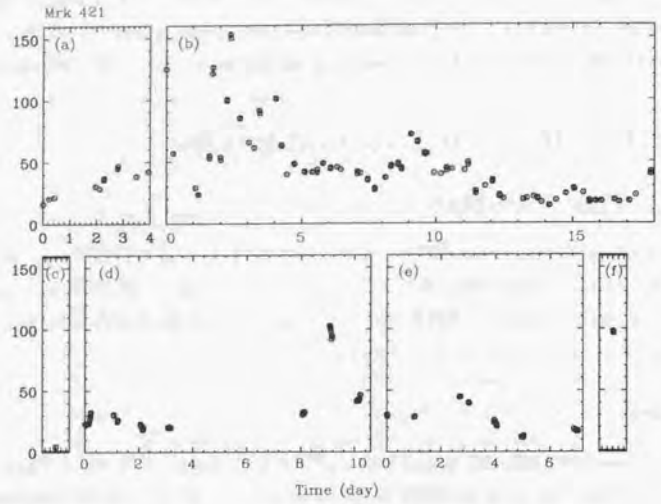

Figure 8.1: PCA light curves of Mrk 421 from 1996 to 1997 *RXTE* observations. The source counts are extracted from PCU 0, 1 and 2. The binning time is 1024 sec. Energy band is 2.5−20 keV. Each panel corresponds to the data: (a) 96/4/19 − 4/23, (b)96/5/3 − 5/21, (c) 96/12/10, (d) 97/4/2 − 4/12, (e) : 97/4/29 − 5/6, (f) : 97/6/3.

in 1997 November (41−56 cts/s for PCA; (d)), which was the change of a factor ∼10. Observations in 1996 May was conducted almost continuously (Figure 8.3 (a)), providing the longest uninterrupted X-ray data of the source for 12 days. During the May 1996 campaign, the source was highly variable and occurrence of ∼ 10 day-by-day flares is clearly seen.

All Sky Monitor

Figure 8.4 shows the variation of the ASM count rates from 1996 to 1999 for four TeV blazars. In the figure, we binned the data into 10-day to reduce the errors on fluxes.

Mrk 421 showed the flux variation of a more than factor 10, and the highest flux was observed in April 1998. This was the epoch when the *ASCA* satellite also observed Mrk 421 for 7 days and found that the source was in the historical high state (Takahashi et al. 1998; Figure 7.2). Mrk 501 also showed large amplitude variability. The highest state was observed in 1997 April to July (see, Figure 8.2). PKS 2155−304 and 1ES 2344+514 seem less variable on time scales of longer than 10 days, but the changes in flux by an

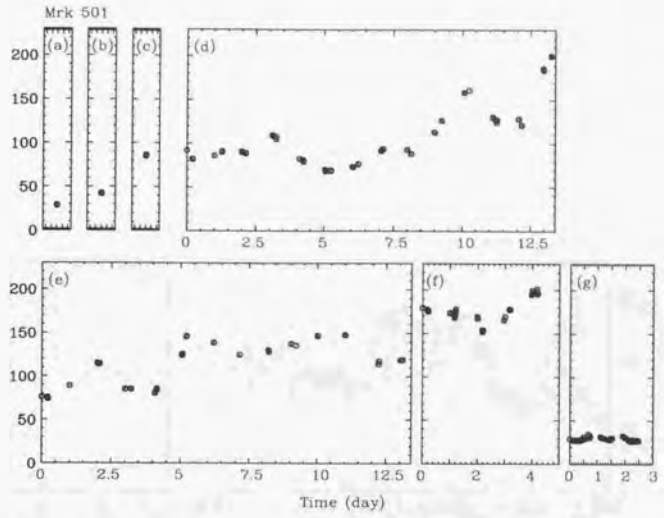

Figure 8.2: PCA light curves of Mrk 501 from 1996 to 1998 *RXTE* observations. The source counts are extracted from PCU 0, 1 and 2. The binning time is 1024 sec. Energy band is 2.5−20 keV. Each panel corresponds to the data: (a) 96/8/1, (b)96/10/22, (c) 97/3/18, (d) 97/4/3 − 4/16, (e) : 97/5/2 − 5/15, (f) : 97/7/11 − 7/16, (g) : 98/5/25 − 5/27.

order of magnitude are seen in the figure.

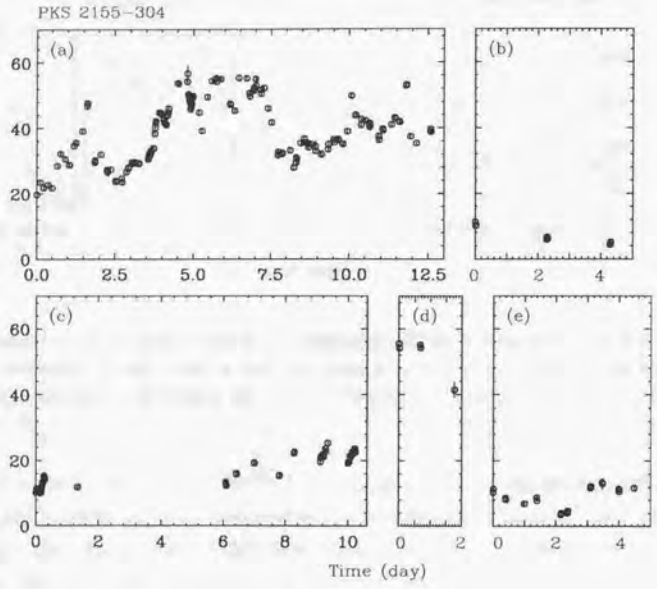

Figure 8.3: PCA light curves of PKS 2155−304 from 1996 to 1998 *RXTE* observations. The source counts are extracted from PCU 0, 1 and 2. The binning time is 1024 sec. Energy band is 2.5−20 keV. Each panel corresponds to the data: (a) 96/5/16 − 5/28, (b)96/7/23 − 7/27, (c) 96/11/14 − 11/24, (d) 97/11/20 − 11/22, (e) : 98/1/9 − 1/13.

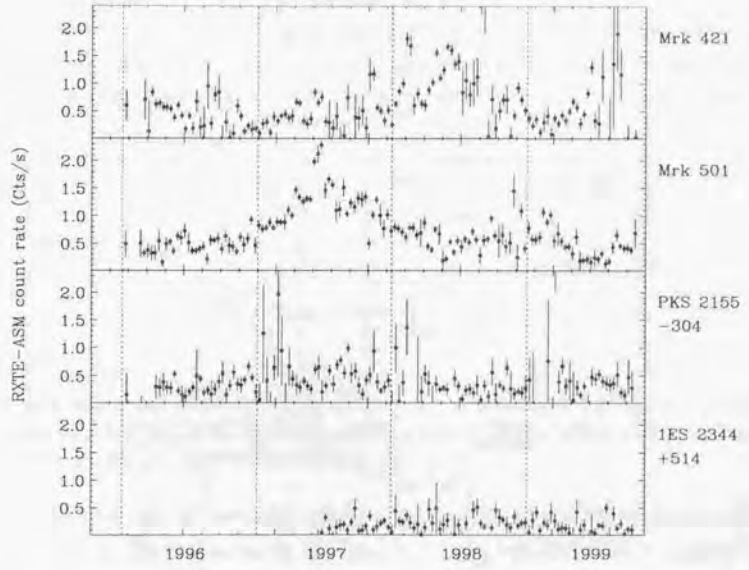

Figure 8.4: *RXTE* ASM Light Curve for TeV blazars. *top*: Mrk 421, *second*: Mrk 501, *third*: PKS 2155−304, and *bottom*: 1ES 2344+514. To reduce errors, the count rates are binned at 10 days.

8.2.2 Energy Dependence of Variability

Long-Term Trend of Variability

We calculate the fractional *rms* variability parameter $F_{\rm var}$ using the PCA light curves shown in Figure 8.1–8.3. To investigate the long-term trend of variability in various energy bands, we divided the PCA light curves into four energy bands; 2.5–5 keV, 5–7.5 keV, 7.5–10 keV and 10–20 keV. The results are summarized in Figure 7.6. From the figure, one can find a clear trend that the amplitude of variability becomes larger as photon energy increases for Mrk 421, Mrk 501 and PKS 2155–304. The energy dependence of variability is similar to that obtained from *ASCA* data for three TeV blazars (§ 7.6). This clearly indicates that the variability amplitude becomes larger for higher energy photons, in the very wide energy range from soft X-rays (0.5 keV) to hard X-rays (20 keV).

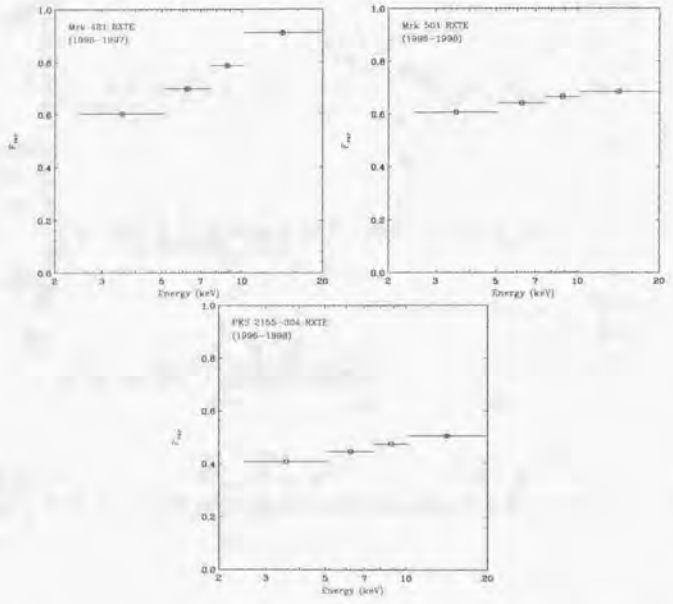

Figure 8.5: Energy dependence of variability of three TeV blazars. The variability parameter was calculated in 2.5–5 keV, 5–7.5 keV, 7.5–10 keV and 10–20 keV, respectively. For the light curves in total *RXTE* bandpass (2.5–20 keV), see Figure 8.1– 8.3. *top left*: Mrk 421, *top right*: Mrk 501, and *bottom*: PKS 2155–304.

Variability of Day-by-Day Flares (PKS 2155–304 1996 May)

In order to study the short-term variability of PKS 2155–304 during the 1996 May observation, we use the PCA data binned at 1024 sec. Variability was calculated for the total exposure (12-days) in four energy bands 2.5–5 keV, 5–7.5 keV, 7.5–10 keV and 10–20 keV, respectively. As shown in Figure 8.6, variability amplitude becomes larger as the photon energy increases (see also Figure 8.5).

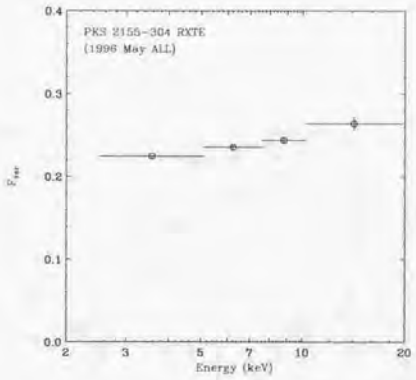

Figure 8.6: Energy dependence of variability of PKS 2155–304 in 1996 May. The variability parameter was calculated for the total 12-day observation in four energy bands (2.5–5 keV, 5–7.5 keV, 7.5–10 keV and 10–20 keV). We used the PCA data binned at 1024 sec.

In order to study the variability behavior for *each* flare event, we divided the total exposure into 9 segments as shown in Figure 8.7. Each segment typically contains one flare. We calculate the variability parameter $F_{\rm var}$ from time-segment #1 to #9. The energy dependencies of variability for individual flares are shown in Figure 8.8.

In five of the flares (# 1, 2, 6, 8, 9), the variability amplitudes becomes larger in higher energy bands, while the trend is not clear for the reminder. Such behavior is very similar to what has been observed for Mrk 421 with *ASCA* (Figure 7.9). These results support the fact that on longer time scales, the variability amplitude becomes larger at increasing photon energy, but for individual flares (or in shorter time-scale), energy dependence of variability changes *flare-by-flare*.

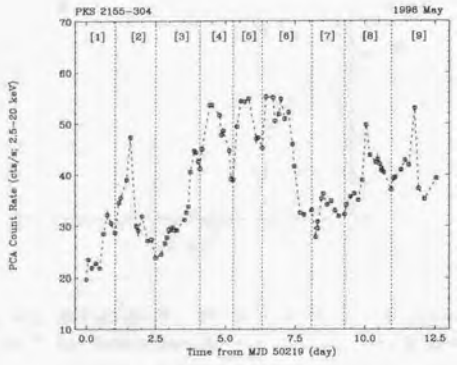

Figure 8.7: PCA light curve of PKS 2155−304 obtained in 1996 May and the division of time interval into 9 separate segments. Data points are joined to guide the eye. Each point represents 1 ksec integration of the PCA data.

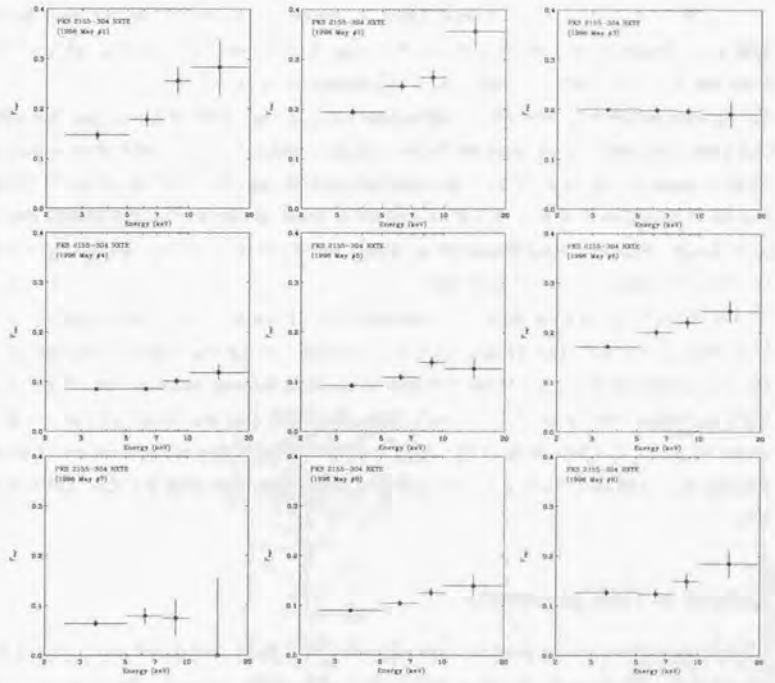

Figure 8.8: Energy dependence of variability of PKS 2155−304 in 1996 May *RXTE* observations. Variabilities for individual flare events are separately shown. Time segments are defined in Figure 8.7. The PCA data were used.

8.2.3 Structure Function

PCA and ASM Data

In this section, we calculate the Structure Function (SF) using the PCA and ASM data. The results are summarized in Figure 8.9.

For Mrk 421 (*top*), we use the PCA data obtained in 1996 May (Figure 8.1(b)). Although data were sampled rather sparsely, we see a hint of a roll-over at ~ 0.5 day, which is consistent with the *ASCA* results (§ 7.2.3). On longer time scales (of $\tau > 1$ day), both the PCA and the ASM data show a flat slope of $\beta \simeq 0.3$.

We plot the SFs of Mrk 501 (*middle*) for 1997 April and 1998 May (Figure 8.2 (d)(g)). For 1998 May data, we divided the total exposure into three parts according to the gaps in the pointing (see Figure 8.2), and calculate the average SF of the three parts. Slope of the SF is steep, such that $\beta \simeq 2.0$ for the PCA data. A roll-over is marginally detected at ~ 1 day. On time scale longer than 1 day, the ASM data shows flatter slope of $\beta \sim 0.5$ than the slope below the roll-over.

For PKS 2155−304 (*bottom*), we calculate the SF for the 12-day observation in 1996 May (Figure 8.3 (a)). The SF gradually rolls around $\tau \sim 0.3$ day, which is consistent with the *ASCA* results (§ 7.2.3). In shorter time scale than 0.3 day, slope of the SF is $\beta \simeq 1.5$, while in longer time scale ($\tau > 1$ day), both the PCA and the ASM data shows flatter slopes of $\beta \sim 0.7$. Close look at the ASM data indicates a sign of appearance of another plateau at ~ 100 day. Such a *second* roll-over cannot be seen both for Mrk 421 and Mrk 501.

Analysis of Time Asymmetry

We calculate the asymmetry of the light curve for PKS 2155−304 based on 12-day uninterrupted data. We measure the time asymmetry of the light curves by the same procedure discussed in § 7.2.3. We first calculate the SF_+ and SF_- using the light curves in the energy range 2.5−5 keV, 5−7.5 keV, 7.5−10 keV, 10−15 keV and 15−20 keV, respectively. Next, *symmetrical parameter* $Sy(\tau)$ was calculated as the difference of SF_+ and SF_- normalized by an original structure function. We calculate the ensemble average of $Sy(\tau)$ in time region $0 \leq \tau \leq 1$ (day).

Results are summarized in Figure 8.10. This result is consistent with what was found for Mrk 421 data in 1998 (Figure 7.13). We find that the light curves of PKS 2155−304 favors 'rise-time < decay-time' and that the light curves become more symmetric at higher energies. In fact, $Sy(\tau)$ is consistent with zero at the highest energy bands.

Combined *RXTE* and *ASCA* Data

When the *ASCA* and *RXTE* results are combined, we can obtain the variability information of four TeV blazars in the very wide time-domain from 10^3 to 10^7 sec. To compare the light curves from four different detectors (*ASCA* SIS/GIS, *RXTE* PCA and ASM), we normalized the light curves by their average values. The results are summarized in Figure 8.11. In these figures, we do not plot the data above the point where the SF values are affected by insufficient long sampling (see § 7.2.3).

As seen in the figure, the SFs of four TeV blazars are well represented by a broken power-law form. We find a break (roll-over) at $\tau = 0.5$ day for Mrk 421, $\simeq 1$ day for Mrk 501, 0.3 day for PKS 2155−304 and 1−10 day for 1ES 2344+514. Importantly, below the break, the SFs have very steep slopes; $\beta \simeq 1.2$ for Mrk 421, 2.0 for Mrk 501, 1.5 for PKS 2155−304 and 2.3 for 1ES 2344+514. This indicates that the rapid time variability of TeV blazars has a strong red-noise character and/or is well approximated by a simple linear trend (see, § 7.2.3). Above the break, the SF slopes flatten to $0 < \beta < 1$ and similar to flickering noise.

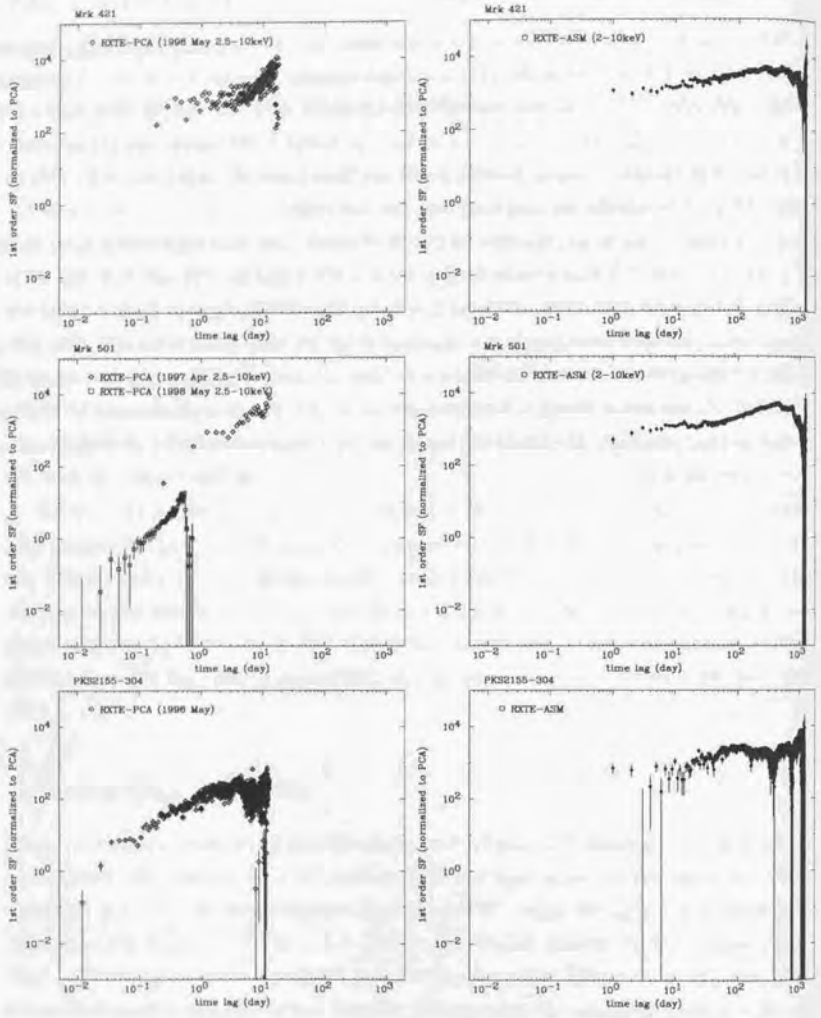

Figure 8.9: 1st order structure function (SF) of three TeV blazars observed with *RXTE* . *top left*: Mrk 421 (1996 May; Figure 8.1(b)), *top right*: Mrk 421 (ASM; Figure 8.4), *middle left*: Mrk 501 (1997 April and 1998 May ; Figure 8.2(d)(g)), *middle right*: Mrk 501 (ASM; Figure 8.4), *bottom left*: PKS 2155−304 (1996 May; Figure 8.3(a)), and *bottom right*: PKS 2155−304 (ASM; Figure 8.4). The PCA light curves from 2.5 keV to 10 keV were used and count rates are normalized to the PCA values.

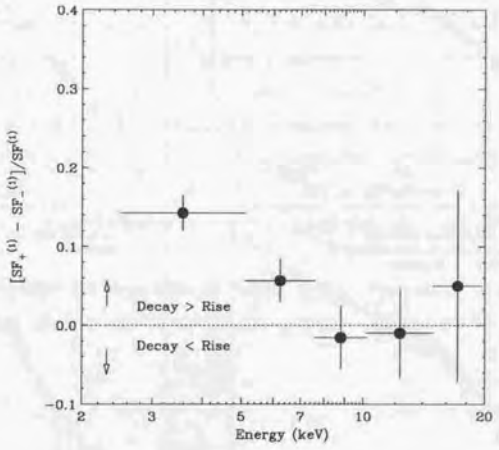

Figure 8.10: Energy dependence of the symmetry parameter $\mathrm{Sy}(\tau) = [\mathrm{SF}_+ - \mathrm{SF}_-]/\mathrm{SF}$ for PKS 2155−304 observed in 1996 May. $\mathrm{Sy}(\tau)$ was averaged over the time lags smaller than one day. Light curves are almost symmetric, i.e., $[\mathrm{SF}_+ - \mathrm{SF}_-]/\mathrm{SF} \sim 0$ at higher energy band, but at lower energies, the symmetry tends to break down.

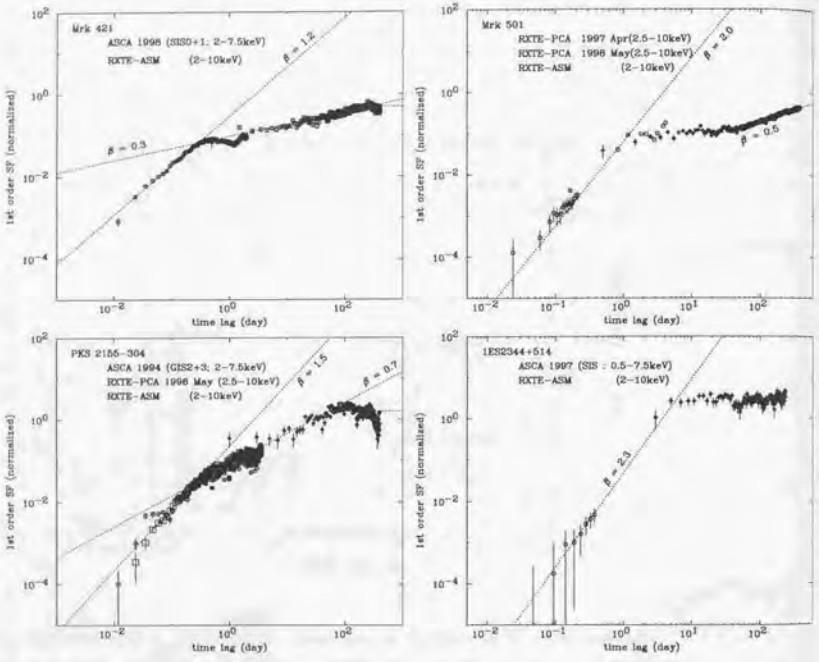

Figure 8.11: Structure functions of TeV blazars (*ASCA* and *RXTE* combined). *top left*: the combined SF of Mrk 421 using the *ASCA* (1998) and the *RXTE* ASM data. *top right*: the combined SF of Mrk 501 using the *RXTE* PCA (1997 April; 1998 May) and the ASM data. *bottom left*: the combined SF of PKS 2155−304 using the *ASCA* (1994), the *RXTE* PCA (1996 May) and the ASM data. *bottom right*: the combined SF of 1ES 2344+514 using the *ASCA* (1997) and the *RXTE* ASM data. Dotted lines are the best fit power-laws.

8.2.4 Spectral Evolutions

We investigate the correlation between the count rate (2.5−20 keV) and the hardness ratio as we did for the *ASCA* data (§ 7.2.4). For the *RXTE* data, we define the hardness ratio as the photon counts in 7.5−20 keV to those in 2.5−7.5 keV. We concentrate on the spectral evolution of PKS 2155−304 during the 12-day observation, because it is best suited to study the time evolution of the spectrum.

PKS 2155−304

We divided data into nine time segments as described in § 8.7. The spectral evolution is shown in the correlation between the intensity versus hardness (Figure 8.12). The general trend of the spectral evolution is that hardness increases when the intensity increases, as is also indicated from the changes in amplitude of variability (Figure 8.8).

In time segments #2 and 3, we can see 'clockwise' hysteresis, as seen in the data obtained with *ASCA* (§ 7.2.4). Reverse motion (*anti*-clockwise) is also detected for region #4 and 8. In other time segments (# 1, 5, 6, 7, 9), loopwise motion is not clear. This complicated 'flare-by-flare' behavior is very similar to that observed for Mrk 421 in 1998 (Figure 7.16).

We do not calculate the time-lags for the PCA data, because in most cases, observations are separated by more than 5 ksec and too sparse to calculate the time-lags.

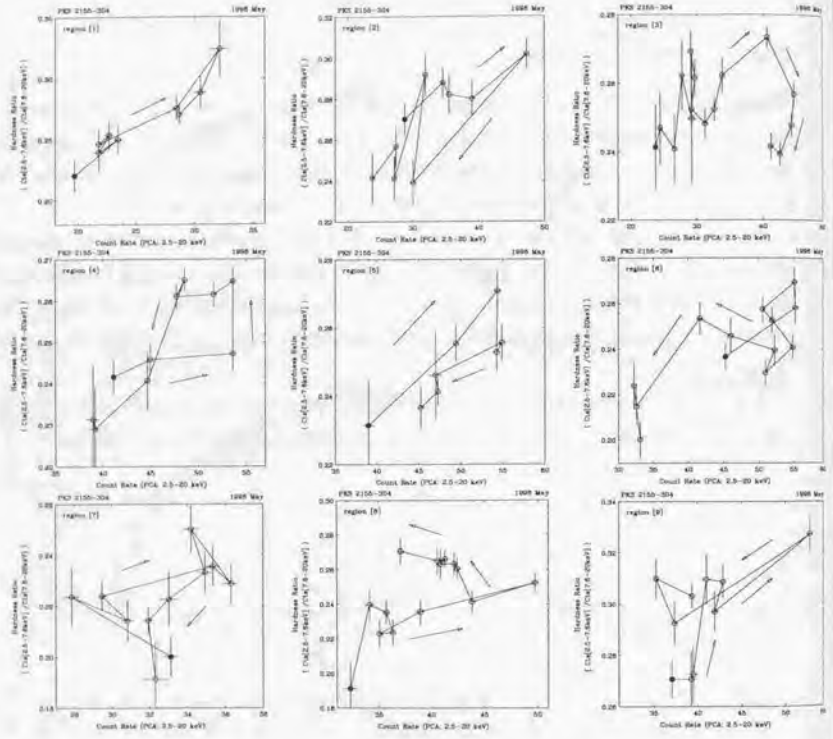

Figure 8.12: Variability patterns for 9 separated segments which are defined in Figure 8.7. Arrows indicate the direction of spectral evolution. The filled circle is the start point of each time segment.

8.3 Results from Spectral Studies

We extracted the energy spectra of PCA for all observations listed in Table A.1−A.8. We use the same analysis procedure as that for the *ASCA* data (§ 7.3). All spectra were fitted with the XSPEC version 10.00. The detector response of PCA are generated from *pcarsp* version 2.37. Although PCA has sensitivity in the 2.5−60 keV (§ 5.2), we only used data from 2.5 keV to 20 keV because each observation was too short to yield enough photon statistics above 20 keV.

8.3.1 Fit with a Power Law Function

We fitted the spectrum with a power law function plus Galactic absorption arising from neutral materials (§ 7.3.1). Since the TeV blazars are highly variable and their spectra evolve on a time scale of hours, we separated the observations into ~ 1 ksec intervals if the exposure is longer than 1 ksec. We found that the simple power law function gives a good representation for most of the PCA data. When a power law function is not adequate, we introduce an additional exponential cutoff to the power law function as described in § 7.3.2. The gradual steepening of spectra found in *ASCA* data (Figure 7.25), is also seen in the energy band covered by *RXTE*.

As an example, we show the spectrum of Mrk 501 taken in 1997 July in Figure 8.13. The best-fit parameters for the model are summarized in Table 8.2. In this case, photon spectrum is gradually steepening to higher energies, thus the fit with a power law function is statistically unacceptable. However, one can see that the fit is improved by using a cutoff power law function.

The results of spectral fitting for all *RXTE* observations of TeV blazars are summarized in Appendix G (Table G.1 – G.10). Examples of *RXTE* spectra for each TeV blazar are given in Figure H.1 (Mrk 421), Figure H.2 (Mrk 501), Figure H.3 and Figure H.4 (PKS 2155−304).

Table 8.2: An example of spectral fitting of Mrk 501

Mission	Detector	N_H (10^{20}/cm^2)	E_c (keV)	Photon Index	Flux (2-10 keV) (10^{-12} erg/cm^2/s)	χ^2 (d.o.f)
I. *RXTE*	PCA	1.73 (fix)	—	$1.95^{+0.01}_{-0.01}$	618±1.6	2.65(45)
II.		1.73 (fix)	$1.11^{+0.13}_{-0.13}$	$2.15^{+0.02}_{-0.02}$	610±19	1.10(44)

Mrk 501 data from 1997 07/12 03:36:51 to 07/12 03:58:27 were used for the fit. Fitting functions are [I] a power law function plus free absorption, [II] a cutoff power law function. The data in the energy band 2.5−20 keV were used. All errors are 1 σ.

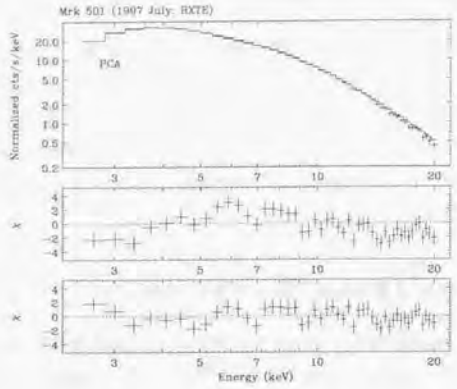

Figure 8.13: The *RXTE* PCA spectra and the best fit power law function. *top*: PCA data for Mrk 501 obtained from 1997 07/12:03:36:51 to 07/12 03:58:27, fitted to a power law function with Galactic absorption. *center*; residuals to a power law function with Galactic absorption. *bottom*; residuals to a cutoff power law function.

Correlations between the isotropic luminosities and photon indices 421, Mrk 501 and PKS 2155−304 are summarized in Figure 8.14. Corresponding figure for *ASCA* observations is Figure 7.27. Photon spectral indices distributed in a wide range from −3.2 to −2.2 for Mrk 421, −2.5 to −1.7 for Mrk 501 and −3.3 to −2.3 for PKS 2155−304. One finds that the spectra tend to be harder when the source becomes brighter, as was indicated in § 8.2.2

8.3.2 Comparison between *ASCA* and *RXTE*

Observations listed in Table 8.3 were conducted simultaneously with *RXTE* and *ASCA* . Therefore, these data enable us to test the consistency between the instruments on-board *ASCA* and *RXTE* . In order to use the energy range covered by two satellites, we selected the data from 2.5 keV to 7.5 keV. Results of the fit with a power law function plus Galactic absorption are shown in Figure 8.15. One can see that the fluxes determined by *RXTE* observations are systematically higher than those determined by *ASCA* by about 15 %. Also note that the photon indices of *RXTE* spectra are systematically stepper than that for *ASCA* results about 0.1. This trend is not improved even if we use the all energy bands, 0.7−7.5 keV for *ASCA* and 2.5−20 keV for *RXTE* .

There are several reasons which may account for these discrepancies. Most serious

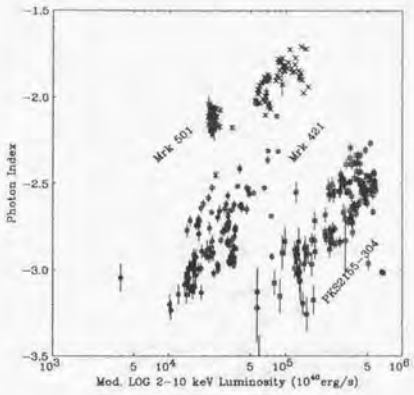

Figure 8.14: Distribution of luminosities and photon indices for all observations with *RXTE* . Mrk 421: from 1996 to 1997 data, Mrk 501: from 1996 to 1998 data, PKS 2155−304: from 1996 to 1998 data. Fluxes are simply converted to the isotropic luminosities by multiplying $4\pi d_{\rm L}^2$, where $d_{\rm L}$ is the luminosity distance.

issue would be imprecise cross-calibration between *ASCA* and *RXTE* . Response matrix of *ASCA* is made, based on both the pre-flight data and in-flight calibration against the Crab. The *standard* value of the Crab spectrum in literature is used for the in-flight calibration (2.1; e.g., Toor & Seward. 1974). On the other hand, the response matrix of *RXTE* PCA is mainly based on the pre-flight calibration. Their observational results for the Crab are slightly different than the value mentioned above. The difference in the spectrum of the Crab ($\Delta\ \Gamma \sim 0.1$) is consistent with the difference seen in Figure 8.15. Also note that the systematic differences of the background subtraction methods between imaging (*ASCA*) and collimating (*RXTE*) instruments would produce the difference in the estimated fluxes.

Table 8.3: List of simultaneous X-ray observations by *ASCA* and *RXTE*

			ASCA		*RXTE*	
Source	Start	End	Photon	Flux (2-10keV)	Photon	Flux (2-10keV)
Name	[MJD]	[MJD]	Index	10^{-12} erg/cm^2/s	Index	10^{-12} erg/cm^2/s
Mrk 421	50567.21	50567.27	2.73±0.04	102.0±1.1	2.97±0.03	129.5±1.2
	50568.21	50568.27	2.75±0.04	98.4±1.1	2.85±0.04	122.8±1.2
	50569.89	50569.94	2.73±0.05	161.4±1.9	2.85±0.04	193.7±2.1
	50571.15	50571.21	2.72±0.06	88.1±1.3	2.87±0.04	110.2±1.3
	50571.21	50571.27	2.77±0.06	85.0±1.4	2.94±0.04	96.1±1.0
	50572.21	50572.27	3.03±0.09	44.8±1.0	3.25±0.07	56.0±1.0
	50574.08	50574.14	2.91±0.05	65.5±0.9	2.93±0.06	80.8±1.3
	50574.14	50574.19	2.86±0.06	63.7±1.0	2.98±0.05	76.2±1.1
	50574.19	50574.25	2.83±0.07	61.0±1.1	3.00±0.06	76.0±1.2
	50602.24	50602.26	2.48±0.03	340.6±2.6	2.61±0.02	402.0±1.8
PKS 2155	50225.18	50225.24	2.42±0.04	156.5±1.6	2.50±0.02	186.5±1.0
−304	50227.24	50227.29	2.58±0.05	91.7±1.2	2.68±0.07	114.0±2.2
	50227.29	50227.35	2.68±0.04	97.5±1.1	2.70±0.03	119.3±0.9
	50227.35	50227.40	2.63±0.05	105.5±1.4	2.69±0.04	126.0±1.4
	50401.41	50401.47	2.85±0.07	36.1±0.7	2.90±0.07	46.1±0.8
	50401.47	50401.53	2.74±0.07	40.5±0.8	2.93±0.06	52.9±0.8
	50401.53	50401.59	2.63±0.07	44.0±0.9	2.78±0.05	56.9±1.1
	50401.59	50401.65	2.83±0.07	45.5±0.8	2.89±0.05	61.2±0.8
	50402.64	50402.69	2.64±0.07	37.1±0.7	2.73±0.08	44.8±0.9

List of simultaneous X-ray observations by *ASCA* and *RXTE*. Fitting model is Galactic absorption plus a power law function. Data from 2.5 keV to 7.5 keV were used for the fit.

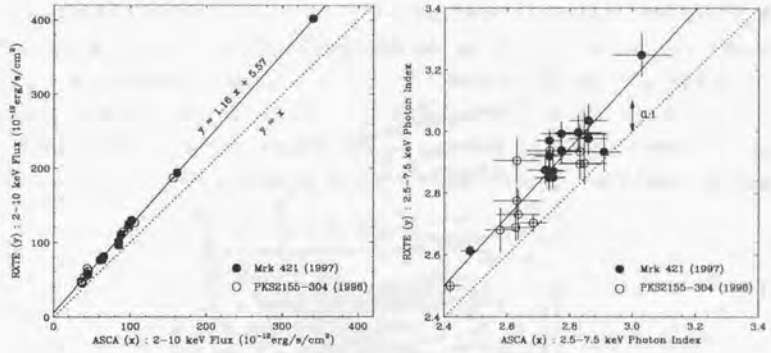

Figure 8.15: Comparison between *ASCA* and *RXTE*. Data from simultaneous observation of Mrk 421 and PKS 2155−304 are used. In order to use the energy range covered by different instruments, we selected the data from 2.5 keV to 7.5 keV. *left* : distribution of *ASCA* flux (2−10 keV) versus *RXTE* flux (2−10keV). *right* : distribution of *ASCA* photon index versus *RXTE* photon index.

8.3.3 Shift of the Synchrotron Peak

To study the time evolution of photon spectra in various states of the source activity, we describe the photon spectra for each TeV blazar in νF_ν space. The PCA spectra were convolved with the best-fit functions (either a power law function or a cutoff power law function). We binned the total PCA bandpass (2.5–20 keV) into 20 energy bands to reduce errors.

The evolution of photon spectra of four TeV blazars are shown in Figure 8.16–8.18. We can clearly see different characteristics of each source.

Mrk 421

Evolution of νF_ν spectra of Mrk 421 in different observations is summarized in Figure 8.16. Contrary to the *ASCA* result, one cannot identify the synchrotron peak in the PCA energy band (2.5–20 keV). However, when the source was in the brightest state (#1), the spectrum is very flat, which indicates that the synchrotron peak is present close to 2.5 keV. This result is consistent with what expected from the *ASCA* data, where synchrotron peak is around 2 keV, when the source was in the brightest state.

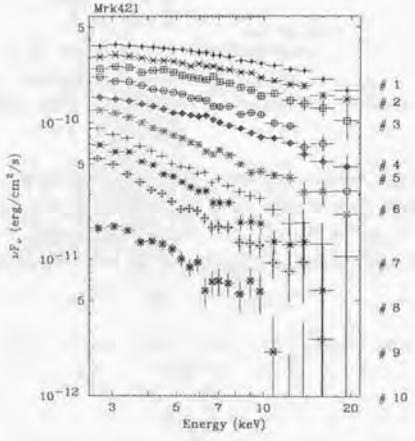

Figure 8.16: Synchrotron peak shifts of Mrk 421 observed with *RXTE* . Data are from #1: MJD 50208.56, #2: MJD 50207.90, #3: MJD 50208.43, #4: MJD 50215.25, #5: MJD 50208.17, #6: MJD 50213.64, #7: MJD 50571.23 #8: MJD 50222.25,#9: MJD 50572.23, #10: MJD 50427.89. For more detail, see Table G.1 – G.3.

Mrk 501

The changes of νF_ν spectra of Mrk 501 are shown in Figure 8.17. When the source was the faintest (#8), energy spectrum was steepest (photon index 2.5) and the synchrotron peak was well below 2.5 keV. However, during the flare, the spectrum largely flattened (photon index 1.7) and the synchrotron peak moved to above 20 keV (#1) – the largest shift ever observed in blazars (Pian et al. 1998; Kataoka et al. 1999a,b). Extrapolating the relation between the peak luminosity L_p and the peak energy E_p found in the *ASCA* results ($E_p \propto L_p^{1.6}$), we expect that the synchrotron peak reaches to ~ 100 keV in the highest state. Note that the amplitude of flux variation is much smaller than that of Mrk 421, but showed dramatical change in the synchrotron peak position.

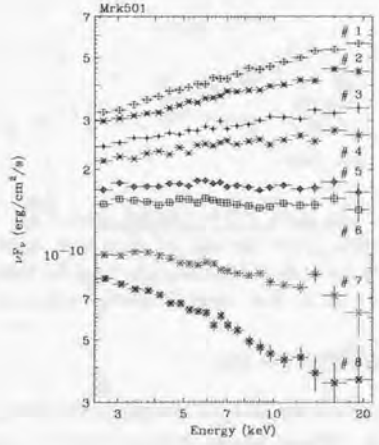

Figure 8.17: Synchrotron peak shifts of Mrk 501 observed with *RXTE* . Data are from #1: MJD 50554.17, #2: MJD 50551.46, #3: MJD 50550.45, #4: MJD 50544.31, #5: MJD 50545.44, #6: MJD 50546.25, #7: MJD 50378.51 #8: MJD 50296.57. For more detail, see Table G.4 – G.6.

PKS 2155–304

We show the changes of νF_ν spectra of PKS 2155–304 in Figure 8.18. There seems to be no clear trend between the flux and spectral shape – in fact, when the source was in the brightest state (#1), spectrum was very *steep*, indicating that synchrotron peak exists at an energy much lower than 2.5 keV. On the other hand, some observations showed very

flat spectra, although luminosity was relatively low (#3, #4). Such a lack of a clear trend has also been implied from the *ASCA* data (Figure 7.30).

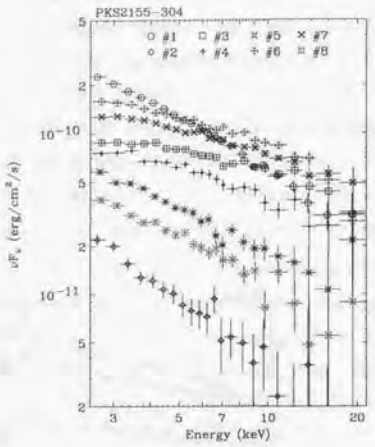

Figure 8.18: Synchrotron peak shifts of PKS 2155−304 observed with *RXTE* . Data are from #1: MJD 50772.96, #2: MJD 50824.40, #3: 50220.23, #4: MJD 50221.90, #5: MJD 50409.13, #6: MJD 50224.91, #7: MJD 50223.95 #8: MJD 50287.38. For more detail, see Table G.7 – G.10.

Combined *ASCA* and *RXTE* Results

By combining with the *ASCA* and *RXTE* results, we can study the X-ray spectral evolution of TeV blazars in different phases of source activity, using more complete data samples.

Figure 8.19 shows the distribution of peak luminosity L_p versus peak energy E_p, compiled from Figure 7.30 from the *ASCA* and Figure 8.16−8.18 from the *RXTE* results. For Mrk 421 and PKS 2155−304, we have seen that all *RXTE* spectra are located above the synchrotron peak energy, and thus we only plot the *ASCA* results. For Mrk 501, some *RXTE* observations revealed relatively flat energy spectra whose photon indices were close to $\Gamma \sim 2.0$. This means that the synchrotron peak exists in the *RXTE* energy band. When the source was in a brighter phase, the photon spectra are harder (~ 1.7) and the peak is thought to be shifted to higher energy than the PCA bandpass.

In Figure 8.19, we added the *RXTE* results of Mrk 501 as a 'box' region and a lower limit to compare the *ASCA* results. In this, we took the systematic differences between

ASCA and *RXTE* into account (§ 8.3.2); when the photon index of a cutoff power law function (§ 7.3.2) gives $\Gamma \leq 2.1$, the spectra is monotonously rising in PCA bandpass, hence E_p is located above 20 keV (equation (7.15)). When Γ is larger than 2.1 and E_p is measured to be in the PCA bandpass, the peak is likely existing in the energy range of the PCA. One can see that the *RXTE* results are exactly on a line which is expected from the *ASCA* results.

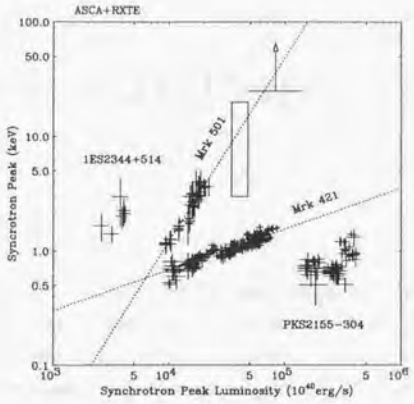

Figure 8.19: Distribution of peak luminosity L_p versus peak energy energy E_p from combined *ASCA* and *RXTE* results.